Central Washington University
ScholarWorks@CWU

All Master's Theses | Master's Theses

Spring 2018

# Assessing the Use of Tsunami Simulations as a Tool to Predict Source Magnitudes and Locations of Paleoearthquakes in Chile

Rebeca Isabel Becerra
*Central Washington University*, becerrar@outlook.com

Follow this and additional works at: https://digitalcommons.cwu.edu/etd

 Part of the Geology Commons, Geomorphology Commons, Geophysics and Seismology Commons, Sedimentology Commons, and the Stratigraphy Commons

## Recommended Citation

Becerra, Rebeca Isabel, "Assessing the Use of Tsunami Simulations as a Tool to Predict Source Magnitudes and Locations of Paleoearthquakes in Chile" (2018). *All Master's Theses*. 947.
https://digitalcommons.cwu.edu/etd/947

This Thesis is brought to you for free and open access by the Master's Theses at ScholarWorks@CWU. It has been accepted for inclusion in All Master's Theses by an authorized administrator of ScholarWorks@CWU. For more information, please contact scholarworks@cwu.edu.

# ASSESSING THE USE OF TSUNAMI SIMULATIONS AS A TOOL TO PREDICT SOURCE MAGNITUDES AND LOCATIONS OF PALEOEARTHQUAKES IN CHILE

---

A Thesis

Presented to

The Graduate Faculty

Central Washington University

---

In Partial Fulfillment

of the Requirements for the Degree

Master of Science

Geological Sciences

---

by

Rebeca Isabel Becerra

May 2018

CENTRAL WASHINGTON UNIVERSITY

Graduate Studies

We hereby approve the thesis of

Rebeca Isabel Becerra

Candidate for the degree of Master of Science

APPROVED FOR THE GRADUATE FACULTY

_____ _____
Dr. Breanyn MacInnes, Committee Chair

_____ _____
Dr. Lisa Ely

_____ _____
Dr. Walter Szeliga

_____ _____
Dean of Graduate Studies

ABSTRACT

ASSESSING THE USE OF TSUNAMI SIMULATIONS AS A TOOL TO PREDICT SOURCE MAGNITUDES AND LOCATIONS OF PALEOEARTHQUAKES IN CHILE

by

Rebeca Isabel Becerra

June 2018

A long-term goal of paleotsunami studies is the ability to predict paleoearthquake parameters based on tsunami deposits found on land. Chile provides an exemplary location for testing methods of making these predictions because the historical record includes 41 major earthquakes as far back as 1562 AD, and there are many known paleotsunami deposits throughout the region. Using these records as a comparison tool, I evaluated simulated tsunami wave heights and inundation extent with the tsunami model GeoClaw for nine hypothetical tsunamigenic large earthquakes ($M_w$ 8.6, 8.8, and 9.0) in south-central Chile with epicenters at -35.1º, -38.8º, and -42.9º. As expected, increasing earthquake magnitude produced larger tsunami wave heights, more sites with tsunami inundation, greater inundation extent, larger seafloor deformation, and generally earlier arrival times. Simulations showed tsunamis from $M_w$ 9.0 earthquakes can inundate coastal plains from nearfield sources, but not exclusively as $M_w$ 8.6 and $M_w$ 8.8 scenarios can produce wave heights over 5 m at some sites. To infer earthquake properties, I analyzed sites to determine where differences between wave heights from variable earthquake magnitudes and source locations were magnified, defined as promising sites. At these promising sites, 60% of them showed tsunami wave heights averaging ≥0.5 m

between simulations, which is a substantial number of sites in the 1,000-km stretch of coast off south-central Chile. The number of sites sensitive to magnitude and/or source location amounted to more than half of the total, proving tangibility considering the quality of bathymetry available. These nine earthquakes showed that more extensive comparisons of possible paleoearthquake parameters with on-land observations is a promising approach to defining characteristics of historical and prehistoric events.

ACKNOWLEDGMENTS

I would like to express my deep appreciation to Dr. Bre MacInnes for her valuable and constructive suggestions during the development of my thesis project. I will always remember my modeling struggles that were instantly solved once I asked her for help. Bre possesses the main qualities of a great advisor: patience, ambition, and optimism. This project was a great learning experience that was made enjoyable because of my advisor.

Assistance on the historical and paleotsunami deposit site locations provided by Dr. Lisa Ely, Dr. Marco Cisternas, Dr. Tina Dura, and Dr. Ed Garrett is also greatly appreciated. In addition, I will never forget the incredible and unique opportunity to visit these sites in Chile with Lisa and Marco – who kept the field team well fed, well versed on the appropriate coring, pit analysis, and Troels-Smith techniques, and well energized on those excellent Chilean "Frac" cookies throughout the field day.

I would also like to offer my special thanks to Dr. Walter Szeliga for his mathematical contributions to my project. Without his help, my methods would not be well supported.

Lastly, I want to express how grateful I am to the supporting roles in my life: my dear family and friends for visiting me, listening to me, and being understanding of the tremendous work that goes into a Master's degree.

TABLE OF CONTENTS

TABLE OF CONTENTS (CONTINUED)

Chapter Page

LIST OF TABLES

LIST OF FIGURES

LIST OF FIGURES (CONTINUED)

# CHAPTER I

# INTRODUCTION

The coastal communities of Chile have one of the world's highest probabilities of being struck by earthquakes and tsunamis (Cisternas et al., 2005; Okal, 2009; Arias et al., 2017). In the 21st century alone, 79 earthquakes of $M_w \geq 7.0$ have occurred in Chile (National Geophysical Data Center/World Data Service (NGDC/WDS, 2018b), including the largest ($M_w$ 9.5) earthquake in recorded history in southern Chile in 1960 (Kanamori, 1977; Barrientos and Ward, 1990; Cisternas et al., 2005; Moreno et al., 2009; Arias et al., 2017). The 1960 earthquake ruptured 1,000 km, which triggered a destructive tsunami with waves up to 15 m (Kanamori, 1977; Heaton and Hartzell, 1987; Cisternas et al., 2005). This earthquake and tsunami killed more than 2,000 people, affected about 2 million people, and caused economic losses of more than 550 million dollars (Arias et al., 2017). The 1575 earthquake closely resembles the 1960 earthquake in damaging effects and size; implying earthquakes of this magnitude have happened before in the past and are likely to occur again in the future. An earthquake of this size in the future could be even more destructive as Chile's population grows.

Since earthquakes and/or tsunamis frequently affect the coasts of Chile (Lay and Kanamori, 1981; Moreno et al., 2010; Ely et al., 2014; NGDC/WDS, 2018b), they are excellent case studies for simulating tsunamis. Tsunami simulations are useful for making modern day assessments of hazards on the coast (Titov and Gonzalez, 1997; Synolakis et al., 2008; Imamura, 2009; Liu, 2009), and one way to improve today's earthquake and

tsunami hazard assessments along Chile's coast is to include information from paleotsunami deposit datasets.

The basis of paleotsunami research is primarily the identification, mapping, and dating of tsunami deposits found in coastal areas (Pinegina and Bourgeois, 2001; Rhodes et al., 2006; Ely et al., 2014). However, compared to modern post-tsunami surveys, where water inundation (or latitudinal extent of water inland; Satake, 2005), runup (the vertical measurement of water height above sea level at maximum inundation; Satake, 2005), and flow depth are easily made (Satake, 2005), similar detailed measurements do not exist for tsunamis occurring prior to the historical record (Cisternas et al., 2005; Bertrand et al., 2008; Bilek, 2009). However, because paleotsunami deposits provide long-term chronologies and recurrence of earthquakes (Pinegina and Bourgeois, 2001; MacInnes et al., 2010; Peterson et al., 2011), information on the extent and size of an earthquake (Nanayama et al., 2003), reconstructions on prehistoric inundation distance (Fujiwara et al., 1999; Bondevik et al., 2005; Scheffers et al., 2008), and runup heights (Peterson et al., 2011), they are essential in improving hazard assessments.

Since earthquakes contribute to the formation of tsunamis, the two are directly linked (Okal, 2009), thus, tsunami deposits are a good proxy for large earthquake activity (Pinegina and Bourgeois, 2001; Jankaew et al., 2008; Monecke et al., 2008; Goff et al., 2010). Paleotsunami deposits retain details of the earthquake's size and extent, and their distribution from inundation and runup estimates can inform us about rupture characteristics of an earthquake such as magnitude and slip (Imamura, 2009; Liu, 2009).

By understanding where large earthquakes are more likely to occur from paleotsunami studies, communities along a particular stretch of coast can begin to plan accordingly in case a big tsunami event does occur.

Because GPS and seismologic instrumentation did not exist prior to the industrial revolution, the prehistoric earthquake record lacks details of rupture source parameters. For this reason, the specifics of past giant megathrust earthquakes have remained unknown for south-central Chile. However, recent studies show that geologic evidence of a tsunami can help constrain the latitudinal extent of the "near field" (the coastal zone parallel to the zone of rupture; MacInnes et al., 2010) in north-south trending coastlines, and potentially source rupture parameters (Geist, 2002; Martin et al., 2008; McCloskey et al., 2008; Goda et al., 2014; Mori et al., 2017).

In particular, studies show that tsunami-deposit distribution can help determine earthquake magnitude distribution (Martin et al., 2008; Satake et al., 2008; MacInnes et al., 2010), and tsunami runup in the near field is sensitive to earthquake slip distribution (Geist, 2002; Hirata et al., 2003; Okal and Synolakis, 2004; Satake et al., 2008; Borrero et al., 2009). Correlating paleotsunami deposits and their distribution at sites along a coast can give estimates on the size of the tsunami, indicated by the location and elevation of interpreted tsunami deposits (Pinegina and Bourgeois, 2001), and therefore help resolve the earthquake magnitude and possibly slip distribution. Thus, by studying tsunami records, we can learn more about the rupture specifics of historical and prehistoric earthquakes (Martin et al., 2008; Satake et al., 2008). These tsunami records

include tsunami height, survey maps of tsunami inundation, and the distribution of tsunami deposits (MacInnes et al., 2010) that act as a catalog of information that I need to complete this project.

## Objectives

The overall purpose of this project is to determine if unknown rupture parameters (i.e., magnitude and source location) from past megathrust earthquakes along the coast of Chile can be predicted with tsunami simulations guided by on-land observations (i.e., paleotsunami deposits or historic written records). Previous extensive field studies in Chile by many other paleoseismologists over several field seasons has allowed me to collect a dataset of the paleotsunami deposits associated with tsunamigenic earthquakes (Lomnitz, 2004; Cisternas et al., 2005; Nelson et al., 2009; Fujii and Satake, 2013; Ely et al., 2014; Moernaut et al., 2014; Dura et al., 2015; Garrett et al., 2015; Nentwig et al., 2015; Hong et al., 2016; L. Ely, pers. comm., 2017). To determine whether tsunami simulations are capable of matching these observations, I investigated the sensitivities of tsunami effects (e.g., wave heights and inundation) generated from nine hypothetical tsunamigenic large earthquakes in south-central Chile (35-43°S) that cover the diversity of characteristics from actual past events. The nine earthquake scenarios represent three different magnitude megathrust earthquakes at a northern, central, and southern location.

The goals of this research are twofold: evaluate the methodology of comparing paleotsunami and historical databases to tsunami simulations and develop a proposed list

of promising sites for future study of paleotsunamis. By evaluating the methodology, I aim to determine the practicality of predicting earthquake rupture specifics just from on-land evidence, especially if information from written records such as co-seismic displacement or the size of the tsunami, supplements paleotsunami deposits. The idea of matching on-land historical observations and geologic evidence of tsunamis to tsunami simulations to investigate the details of paleoearthquake rupture processes is an actively developing area of paleoseismology research (c.f. Martin et al., 2008; MacInnes et al., 2010; Fujii and Satake, 2013; Mori et al., 2017).

In addition to evaluating the practicality of this method, by analyzing my simulations, I identify locations on the coast that filter and/or amplify earthquakes from variable rupture sizes and source locations by magnifying differences in tsunami inundation and runup values. The purpose of this part of my evaluation is to recognize unstudied sites with a high potential for distinguishing past tsunamis within the modeling region. Future research of paleotsunamis at these hypothetically "promising" locations would therefore have the potential to contribute greater amounts of information to the paleoseismology of Chile than studies elsewhere.

# CHAPTER II

# BACKGROUND

## Regional Geologic Setting

As part of a 5,000-km subduction system, Chile is located where the Nazca plate subducts to the northeast at an oblique <10° angle beneath the South American plate with a convergence rate that varies from 0.08 m/yr in the north to 0.065 m/yr in the south (Demetz et al., 2010; Dura et al., 2015; Omira et al., 2016;). Tsunamis have occurred frequently following great ($M_w$ >8) magnitude earthquakes along the Chilean coast (Figure 1; Lomnitz, 2004; Bilek, 2009; Omira et al., 2016). The Chilean triple junction (46.5°S, 75.5°W) lies on the southern portion of the subduction zone, where the Nazca and South American plates converge at 0.07 m per year (Angermann et al., 1999).

Significant strain accumulation along the offshore subduction zone results in megathrust earthquakes with a recurrence interval of one earthquake per 100-200 years or shorter on any given segment of the Chilean margin (Lay and Kanamori, 1981; Moreno et al., 2010; Ely et al., 2014). The average historic recurrence interval based on written records falls within this range at ~one per 128 years (Garrett et al., 2015), with stratigraphic evidence showing longer average intervals interpreted for some segments (Cisternas et al., 2005; Garrett et al., 2015).

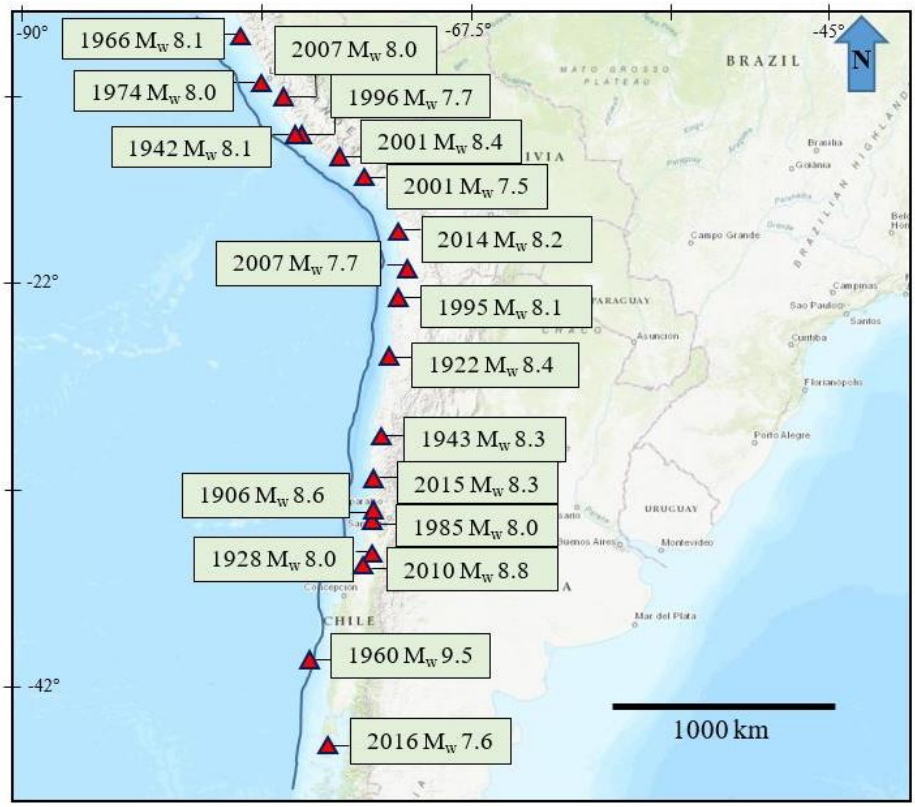


Figure 1: Overview map of most of the South American subduction zone (dark line) with epicenters of significant earthquakes (triangles) from the 20th and 21st centuries and their magnitudes. Locations from Bilek (2009). Background image from an ArcGIS Online Basemap.

The south-central region of Chile (35-43°S) is divided into two sections: the 2010 Maule segment (33.5-37.5°S) and the 1960 Valdivia segment (37.5-46°S; Figure 2; Moreno et al., 2010; Moreno et al., 2011) that often rupture separately. The mechanical behavior of the south-central Chile subduction zone reveals that the updip zone near thetrench is the characteristic location of megathrust rupture (Lay et al., 2010; Ide et al., 2011; Vigny et al., 2011).


Figure 2: Map showing locations of paleotsunami deposit field sites and towns noted in historic documents within south-central Chile. The 2010 Maule rupture and 1960 Valdivia rupture areas, defined by aftershocks, are outlined within the modeling area (Plafker and Savage, 1970); note the overlapping rupture areas between the 2010 and 1960 earthquakes between Mocha Island and Santa Maria Island.

## Past Earthquakes

Historical records of great Chilean earthquakes extend to the 1500s (Lomnitz, 1970, 2004; Cisternas et al., 2005, 2012; Carvajal et al., 2017). Notable tsunamigenic earthquakes in the 20$^{th}$ and 21$^{st}$ centuries that ruptured between Lima, Peru and Chiloe Island, Chile (12-43°S) include 1906, 1922, 1928, 1942, 1943, 1960, 1966, 1974, 1985, 1995, 1996, 2001, 2007, 2010, 2014, and 2015 (Figure 1; Cisternas et al., 2005; Bilek, 2009; Ely et al., 2014). The earthquakes or tsunamis in south-central Chile's history that were either instrumentally recorded or noted in historical accounts include those from the 1575, 1737, 1835, 1837, 1960, and 2010 earthquakes. All except the 1737 earthquake left sand deposits in coastal stratigraphy. Each of these earthquakes and tsunamis will be discussed in further detail below.

Most data prior to the 1960 earthquake is limited to eyewitness written accounts from Chileans and Spanish conquistadors, or estimations from modern studies (i.e., fault rupture locations). Written records for the 1575 (~$M_w$ 8.0-8.5), 1737 (~$M_w$ 7.5), and 1837 ($M_w$ 8.0) earthquakes are available publically (Lockridge, 1985), and include descriptions of earthquake shaking, infrastructure damage, tsunamis, and coastal land-level changes (Lomnitz, 2004; Cisternas et al., 2005). Pre-instrumental magnitude estimates rely heavily on comparisons of written descriptions with known events (Lomnitz, 2004).

The 27 February 2010 Chile earthquake ($M_w$ 8.8) occurred offshore the Maule region, some 360 km southwest of Santiago (Delouis et al., 2010; Lorito et al., 2011; Fujii and Satake, 2013; Moernaut et al., 2014; Figure 2). The ensuing tsunami caused

severe damage along adjacent coasts, with reported maximum wave heights of more than 10 m at many sites between Constitucion and the Arauco Peninsula (Lorito et al., 2011). The earthquake and tsunami claimed more than 500 lives (Lorito et al., 2011), the earthquake ruptured ~500 km of the subduction zone (Vigny et al., 2011), and estimates of maximum slip go as high as 22 m (Fujii and Satake, 2013). Subsidence occurred mainly in the central valley, although scientists measured up to 0.06 m of subsidence at the coast 15 km south of Constitucion (Vigny et al., 2011).

The 22 May 1960 mainshock earthquake ($M_w$ 9.5) occurred off the coast of southern Chile in the Valdivia segment (between 37.5°S and 46°S; Figure 2) and was the largest earthquake instrumentally recorded (Kanamori, 1977). The 1960 mainshock was third in a sequence of major earthquakes ($M_w$ 7.5 on May 21, and $M_w$ 7.8 on May 22) within a 33-hour period (Barrientos and Ward, 1990). The mainshock ruptured nearly 1000 km beginning near Lumaco (38°S, 74°W) in the north and ended near the Taitao Peninsula (46°S) at the Chilean triple junction (Plafker and Savage, 1970). The earthquake caused coastal uplift as large as 5 m and 2 m subsidence (Plafker and Savage, 1970, 1972), and near field tsunami run-up heights of 10–20 m (Siever et al., 1963; Wright and Mella, 1963; Plafker and Savage, 1970). The slip, which averaged 20-30 m over the length of the rupture (Plafker and Savage, 1970; Cifuentes, 1989) and up to 40 m locally (Barrientos and Ward, 1990; Moreno et al., 2009), expended about 350 years' worth of plate motion (Cisternas et al., 2005). From historical accounts of damage, the

1960 slip area had ruptured at least partially only 123 years before, in 1837, and also at earlier intervals of 100 and 158 years, in 1737 and 1575 (Lomnitz, 1970).

The 20 February 1835 earthquake ($M_s \approx 8$-8.5) was one of the more widely documented Chilean historical earthquakes, described by Charles Darwin in his *Voyage of the Beagle* (Darwin, 1851; Lomnitz, 2004). Darwin felt the earthquake on land near Valdivia (Darwin, 1851), and he described Concepcion as the source area of the mainshock (Campos et al., 2002). With an estimated rupture length of 350 km (Vigny et al., 2011), there was no reported damage in Valdivia, but locals reported total destruction at both Concepcion and Quiriquina Island, which uplifted 2 m.

The 7 November 1837 earthquake ($M_s \approx 8$) damaged towns along the central third of the Valdivia segment and caused coastal uplift and inland subsidence, seaward and landward respectively, of the hinge line (the down-dip limit of rupture and the neutral line of vertical deformation of the upper plate; Bodin and Klinger, 1986; Vigny et al., 2011) along the southern half of Valdivia (Cisternas et al., 2005, 2017). The epicenter of the earthquake was located between Valdivia and Castro (Lomnitz, 2004). Note that pre-instrumental earthquake archives are incomplete, especially for the 1837 earthquake, and earthquake parameters were likely created from uncertain intensity and epicenter estimations (Moernaut et al., 2007). The associated tsunami amplitude waves, cresting 6-m high in Hawaii (Lander and Lockridge, 1989), suggests that the 1837 earthquake released almost 70% of the magnitude of the 1960 mainshock (Abe, 1979). The

earthquake caused up to 2-m uplift on Lemus Island and the initiation of many landslides in the entire coastal region (Lomnitz, 2004).

The 24 December 1737 earthquake ($M_s \approx 7.5$) in Valdivia, known only from secondary sources, damaged the few remaining Spanish settlements south of Concepcion, spanning the length of Valdivia to Chiloe (Cisternas et al., 2005). The earthquake lacked a reported tsunami, even though tsunamis from central Chile in 1730 and 1751 were noted locally (Lockridge, 1985) and in Japan (Ninomiya, 1960; Watanabe, 1998).

The reported effects from the 16 December 1575 earthquake ($M_s \approx 8$-8.5) most nearly resembled those from 1960 (Cisternas et al., 2005). Conquistadors, at forts limited to the northern half of the 1960 rupture area, wrote of persistent marine inundation near Imperial, Valdivia and Castro that implies widespread tectonic subsidence. They also described a devastating tsunami near Valdivia (Cisternas et al., 2005), and observed in the north as far as Concepcion (Lomnitz, 2004).

## Site-Specific Records of Tsunamis in South-Central Chile

The paleotsunami deposits studied over many years in Chile provide additional information about each of the past subduction-zone events in the region. Unraveling the details of earthquakes and tsunamis requires a dense array of data. Within the region of south-central Chile, there are a total of 12 historical sites and 25 paleotsunami locations that I have compiled into a database (Table 1). The six earthquakes in the dataset include those that took place in 1575, 1737, 1835, 1837, 1960, and 2010, respectively.

Table 1: Site coordinates of locations that either preserve past tsunami deposits or have a historical written record of an earthquake/tsunami (Note: the 1960 and 2010 tsunami deposits are modern events and not considered paleotsunami deposits).

| **Latitude** | **longitude** | **data type** | **earthquake year (*if known*)** | **nearest town** | **reference** |
|---|---|---|---|---|---|
| -35.108160 | -72.200040 | Tsunami deposit | 1960 | La Trinchera | Ruiz, 2016; Morton et al., 2011 |
| -35.304260 | -72.400280 | Tsunami deposit | 1960 | Constitucion | Ruiz, 2016; Morton et al., 2011 |
| -36.54677 | -72.935408 | Tsunami deposit | 2010 | Dichato | L. Ely, pers. comm., 2017; Yasuda et al., 2010 |
| -36.558750 | -72.957020 | Tsunami deposits | 1835, 2010 | Coliumo | Ruiz, 2016 |
| -36.738746 | -72.993555 | Historical account | 1960, 2010 | Concepcion/ Talcahuano | Cisternas et al., 2005; Dura et al., 2015; Udias et al., 2012; Ely et al., 2014; Dura, et al., 2017; Carvajal et al., 2017 |
| -36.745843 | -73.020407 | Tsunami deposit | 2010 | Andalien | L. Ely, pers. comm., 2017; Garrett et al., 2013 |
| -36.790226 | -73.038492 | Historical accounts | 1575, 1835, 1960, 2010 | Penco | Dura et al., 2017; Garrett et al., 2013 |
| -37.023677 | -73.547261 | Historical account | 1835 | Santa Maria | Wesson et al., 2015; Melnick et al., 2006 |
| -37.195912 | -73.564125 | Tsunami deposit | 2010 | Llico | L. Ely, pers. comm., 2017; Lario et al., 2016 |
| -37.226992 | -73.440106 | Tsunami deposit | 2010 | Tubul | Ruiz, 2016; Lario et al., 2016 |
| -37.806580 | -72.704227 | Historical account | 1575, 1960 | Angol | Cisternas et al., 2005 |
| -38.250503 | -73.485413 | Both | 1835, 1960, 2010 | Quidico | Hong et al 2016; Dura et al., 2017 |
| -38.341936 | -73.495381 | Both | 1575, 1960, 2010 | Tirua | Cisternas et al., 2017; Ely et al., 2014; Nentwig et al., 2015; Garrett et al., 2013; Dura, et al., 2017 |
| -38.414942 | -73.888563 | Tsunami deposit | 2010 | Mocha Island | Bahlburg and Spiske, 2015 |
| -38.783204 | -73.400013 | Both | 1575, 1960 | Puerto Saavedra | Atwater et al., 2013; Dura et al., 2017; Wright and Mella, 1963 |
| -39.214094 | -73.203979 | Tsunami deposit | 1960, 2010 | Nueva Tolten | T. Dura, pers. comm., 2017; E. Garrett, pers. comm., 2017 |
| -39.299618 | -73.220975 | Tsunami deposit | 1960, 2010 | Tolten Viejo North & South | T. Dura, pers. comm., 2017; E. Garrett, pers. comm., 2017 |

Table 1 (Continued): Site coordinates of locations that either preserve past tsunami deposits or have a historical written record of an earthquake/tsunami (Note: the 1960 and 2010 tsunami deposits are modern events and not considered paleotsunami deposits).

| **Latitude** | **longitude** | **data type** | **earthquake year (*if known*)** | **nearest town** | **reference** |
|---|---|---|---|---|---|
| -39.357892 | -73.190059 | Tsunami deposit | 1960 | Rio Queule, S of Maitenco | T. Dura, pers. comm., 2017; E. Garrett, pers. comm., 2017 |
| -39.437605 | -73.200573 | Tsunami deposit | 1960 | Missisipi, Rio Lingue | A. Nelson, pers. comm., 2017; J. Bourgeois, pers. comm. |
| -39.860929 | -73.322706 | Both | 1575, 1837, 1960 | Valdivia | Cisternas et al., 2005; Garrett et al., 2015; Dura et al., 2017; Nelson et al., 2009 |
| -39.950000 | -73.570000 | Tsunami deposit | 1960 | Chaihuin | M. Cisternas, pers. comm., 2017 |
| -40.532894 | -73.699730 | Tsunami deposit | 1960 | Pucatrihue | M. Cisternas, pers. comm., 2017 |
| -41.620103 | -73.580401 | Both | 1575, 1837, 1960 | Maullin | Cisternas et al., 2005; Atwater et al., 2013 |
| -41.642147 | -73.635156 | Tsunami deposit | | Caulle | Cisternas et al., 2017; Atwater et al., 2013 |
| -41.851796 | -73.998253 | Tsunami deposits | 1575, 1960, 2010 | Chucalen | Garrett et al., 2015 & 2013; Dura et al., 2017 |
| -41.862544 | -73.828445 | Historical accounts | 1837, 1960 | Ancud | Cisternas et al., 2005 |
| -41.899533 | -73.993450 | Both | 1575 | Chiloe Island | Garrett 2015; Kempf et al., 2017; Dura et al., 2017; Lomnitz, 2004 |
| -41.925507 | -74.005138 | Tsunami deposits | 1575, 1837, 1960 | Cocotue on Isla Chiloe | Cisternas et al., 2017; Dura et al., 2017 |
| -42.042103 | -74.023712 | Tsunami deposit | | Chepu | T. Dura, pers. comm., 2017; E. Garrett, pers. comm., 2017 |
| -42.479688 | -73.762401 | Historical accounts | 1575, 1837, 1960 | Castro | Cisternas et al., 2005; Dura et al., 2017 |
| -42.596550 | -74.120778 | Tsunami deposits | 1575, 1837, 1960 | Lake Huelde | Kempf, 2017 |

## Historical Accounts

The data types recorded from historical accounts of earthquakes and tsunamis include a rich catalog of earthquake shaking, infrastructure damage, tsunamis, and coastal

land-level changes (Cisternas et al., 2005; Figure 3; Table 1). Historic accounts that include rupture magnitude, latitudinal rupture extent, vertical and horizontal deformation on the coast, and areal extent inundated by tsunamis are not well constrained because they are estimated from aftershock sequences and written observations (Carvajal et al., 2017). The twelve locations on the south-central Chile coast with records of past events include Maullin, Tirua, Concepcion, Angol, Puerto Saavedra, Quidico, Penco, Valdivia, Castro, Chiloe Island, Ancud, and Santa Maria (Table 1; Figure 2).

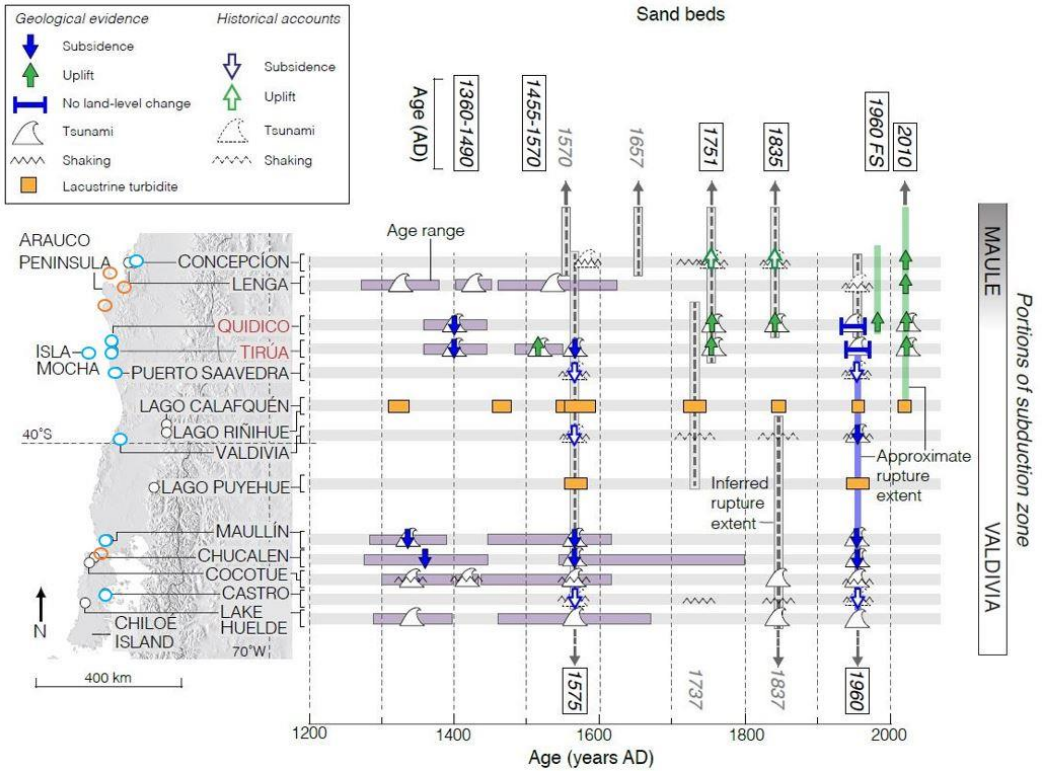


Figure 3: Historical accounts of past earthquakes modified from Dura et al. (2017) summarizing the written historical records and paleoseismic evidence of great ruptures along the Valdivia and Maule portions of the subduction zone. Eight of my twelve historical sites circled in blue, and the four unmapped sites are Santa Maria, Penco, Angol, and Ancud (from north to south) and circled in orange.

## Paleotsunami Deposits

Paleotsunami deposits studied over decades in Chile provide supplemental information to historical accounts. The three-dimensional distribution of tsunami sand sheets provides information on a deposit's height above sea level, landward extent and taper, and regional continuity (Cisternas et al., 2005; Rhodes et al., 2006; Table 1). Mapping the extent of paleotsunami layers throughout a site is possible due to correlating buried soils among different cores or trenches (Kelsey et al., 2002). In low-lying marshes, paleotsunami deposits are preserved as abrupt changes between buried soil and sand in the stratigraphy (Kelsey et al., 2002). Paleotsunami deposits are dated radiometrically either using standard radiocarbon analysis of bulk peat from below the tsunami sand contacts or accelerator mass spectrometry (AMS) analysis of small leaf, twig, or organic rip-up fragments from within the tsunami sand layer (Peterson et al., 2011).

Paleotsunami sites are useful markers of the size of the associated earthquake (Jaffe and Gelfenbaum, 2002) and many of these sites in Chile record abrupt coseismic or interseismic changes in the land-level (Dura et al., 2017). Buried soils correspond to sudden upward or downward movement in the stratigraphic record (Kelsey et al., 2002). Coupled with contact abruptness at the top of the buried soil, this is a qualitative indicator of the suddenness of submergence of a soil (Nelson et al., 1996). Paleotsunami deposits have been shown to reveal the extent of tsunami inundation inland (Jaffe and Gelfenbaum, 2002; Smith et al., 2007), the water velocity (Jaffe and Gelfenbaum, 2007),

the source location of an associated earthquake (Szczucinski, 2012), and earthquake recurrence intervals (Goto et al., 2011).

Twelve locations in my tsunami deposit catalog record pre-1960 paleotsunamis, including Maullin, Tirua, Puerto Saavedra, Quidico, Valdivia, Chucalen, Chepu, Cocotue, Chiloe Island, Caulle, Lake Huelde, and Coliumo (some of the sites with pre-1960 tsunami deposits also have 1960 or 2010 deposits; Table 1; Figure 2). Thirteen additional sites record only recent deposits from the 1960 and/or 2010 tsunami: Tolten Viejo North and South, Mocha Island, Nueva Tolten, Queule, Missisipi, La Trinchera, Constitucion, Tubul, Andalien, Llico, Dichato, Chaihuin, and Pucatrihue (Table 1; Figure 2).

# CHAPTER III

# TSUNAMI MODELING METHODS

## Introduction to GeoClaw

The tsunami modeling software I used is GeoClaw, a finite-difference model based on nonlinear shallow-water equations, which calculates tsunami inundation onto coastal areas (Mandli et al., 2016; Clawpack Development Team, 2017). GeoClaw is an open-source software (http://www.clawpack.org/geoclaw) approved by the US National Tsunami Hazard Mitigation Program for predicting tsunami arrival times and runup heights (Gonzalez et al., 2011). GeoClaw is unique in using adaptive mesh refinement, which increases the modeling resolution near the tsunami wave as it travels across bathymetry and inundates topography (Berger and LeVeque, 1998; LeVeque et al., 2011). Nonlinear shallow water equations are one of the commonly accepted approximations for calculating tsunami propagation and inundation (George and LeVeque, 2006).

GeoClaw uses Cartesian grid cells, and the code approximates and updates cell averages of the water depth and radial momentum in each time step (LeVeque, 2002). This method exactly conserves mass and momentum in regions where the bathymetry is horizontal and uninterrupted. In regions with a slope, mass and momentum are conserved using piecewise functions (LeVeque et al., 2011). GeoClaw handles inundation by setting the water depth in each grid cell to zero for dry land and positive for wet cells, and allows the state to change in each time step (LeVeque et al., 2011). GeoClaw requires two types

of input data; the bathymetry of the ocean and coastal regions combined with onshore topography, and seafloor motion (either static or kinematic seafloor deformation) initiating the tsunami (LeVeque et al., 2011).

## Model Input Data: Bathymetry and Topography

Combined bathymetry and topography for coastal Chile is currently publically available in three datasets. These include:

1. The General Bathymetric Chart of the Oceans (GEBCO) 2014 30-second resolution raster seamless topography and bathymetry dataset (Intergovernmental Oceanographic Commission et al., 2014).
2. The Scripps Institution of Oceanography Shuttle Radar Topography Mission (SRTM+) 2009 30-second resolution global topography and bathymetry distributed by the National Geospatial-Intelligence Agency (NGA; Becker et al., 2009). One of the ways Scripps gathers their bathymetric grids is from the Marine Geophysical Trackline data (NGDC/WDS, 2017), which provides unique depth constraints for many near shore areas including Asia, Africa, and South America (Becker et al., 2009).
3. The Estimated Seafloor Topography (ETOPO1) 30-second global relief model of Earth's surface that integrates land topography and the ocean bathymetry built from global and regional datasets distributed by the National Oceanic and Atmospheric Administration (NOAA) National Centers for Environmental

Information (formerly the National Geophysical Data Center; Amante and Eakins, 2009).

I decided to use the GEBCO bathymetry dataset in this study because the continental shelf appeared more credible than in the other two datasets. I inspected each dataset by plotting them at their native 30-second resolution. Plots of the three datasets (Figure 4) showed a homogeneous continental shelf for the GEBCO dataset, whereas the Scripps dataset included mounds and depressions, and the ETOPO dataset contained many small depressions. The GEBCO dataset best represented the continental shelf when compared to real bathymetric maps of the Chilean shelf (Figure 5).

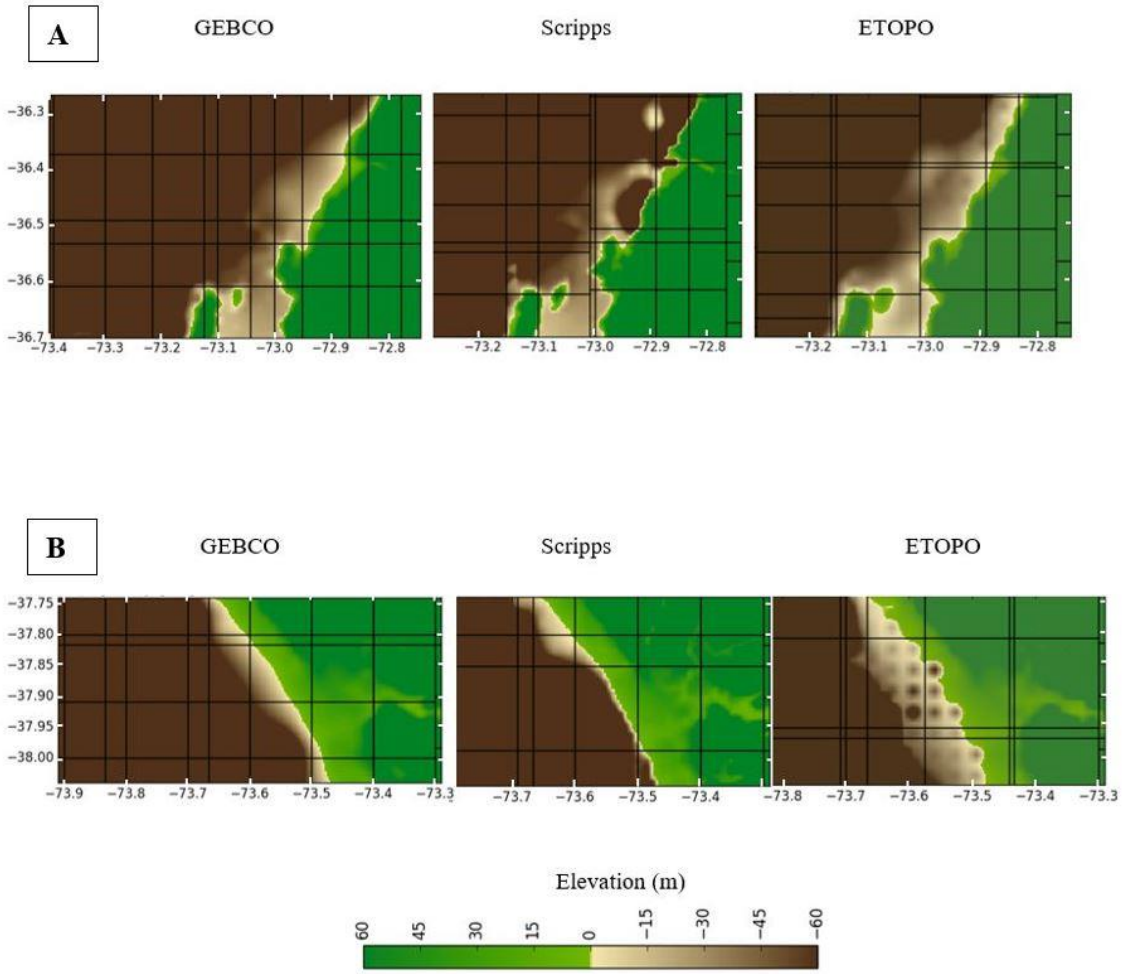


Figure 4: Three different sources of bathymetric data (GEBCO, Scripps, and ETOPO) with 30-second resolution at two different locations along the central Chilean coast. GEBCO appears more credible than Scripps or ETOPO (see text, section Model input data, and Figure 5). Bathymetry from Amante and Eakins (2009), Becker et al. (2009), and Intergovernmental Oceanographic Commission et al. (2014) respectively.

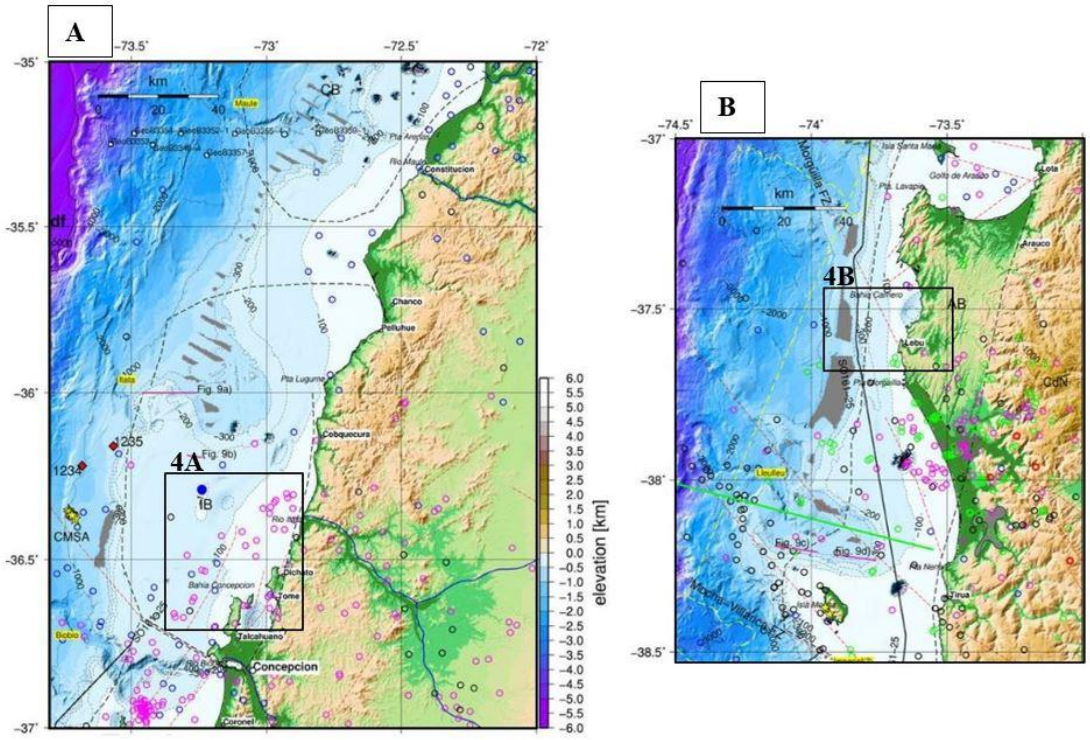


Figure 5: Real-world continental shelf morphology off the coast of south-central Chile modified from Volker et al. (2012) to compare to Figure 4. 5A (Concepcion area) is north of 5B (Lebu area). Locations for comparison are within the black boxes labeled 4A and 4B. The data used to create these maps is currently unavailable for model input.

The GEBCO bathymetry likely best represents the Chile continental shelf because the Chilean Navy Oceanographic and Hydrographic service provided updated grids from Electronic Navigation Charts (ENCs) off the coast of Chile (Weatherall et al., 2015; "Improving GEBCO's bathymetric grids in shallower water areas," https://www.gebco.net/data_and_products/gridded_bathymetry_data/shallow_water_bathymetry/). This data set included over 81,000 soundings and the seafloor surface was created in Generic Mapping Tools (GMT) in combination with other Chilean trackline survey data (18°S to 55°S; 77°W to 67°W; Weatherall et al., 2015).

## Model Input Data: Fault Source Scenarios

GeoClaw requires input data to calculate the seafloor deformation initiating the tsunami. GeoClaw uses the standard Okada (1985) equations of deformation of a homogenous half-space to calculate the seafloor deformation from rectangular subfaults. GeoClaw assumes an instantaneous deformation of the seafloor translated directly to the water surface (Borrero et al., 2015). I created nine earthquake scenarios: $M_w$ 8.6, 8.8, and 9.0 at a northern, central, and southern location, using uniform slip along a single subfault. The $M_w$ 8.6, 8.8, and 9.0 earthquakes represent megathrust events similar to recent past events in rupture area. The strike, dip, and depth of the subduction zone interface is defined by the Slab 1.0 model (Hayes et al., 2012). Rake was considered a standard 90º for a megathrust event (Gusman et al., 2014; Hayes et al., 2014). Subfault location is defined by the longitude, latitude, and depth of the center of the up-dip edge of the subfault. Slip and along-strike segment length and width is dependent on the earthquake magnitude. See Table 2 for the compiled inputs for all nine scenarios.

Table 2: Rupture input for nine earthquake scenarios along the Chile coast.

| Scenario name | strike (deg) | length (km) | width (km) | depth (m) | slip (m) | rake (deg) | dip (deg) | longitude (subfault top center) | latitude (subfault top center) |
|---|---|---|---|---|---|---|---|---|---|
| **$M_w$ 8.6N** | 9.5 | 400 | 110 | 7.7 | 5 | 90 | 18 | -73.69335 | -35.10032 |
| **$M_w$ 8.6C** | 3.1 | 400 | 110 | 7.6 | 5 | 90 | 18 | -74.88442 | -38.83812 |
| **$M_w$ 8.6S** | 5.3 | 400 | 110 | 6.8 | 5 | 90 | 18 | -75.47577 | -42.90477 |
| **$M_w$ 8.8N** | 9.5 | 500 | 120 | 7.7 | 8 | 90 | 18 | -73.69335 | -35.10032 |
| **$M_w$ 8.8C** | 3.1 | 500 | 120 | 7.6 | 8 | 90 | 18 | -74.88442 | -38.83812 |
| **$M_w$ 8.8S** | 5.3 | 500 | 120 | 6.8 | 8 | 90 | 18 | -75.47577 | -42.90477 |
| **$M_w$ 9.0N** | 9.5 | 600 | 130 | 7.7 | 12 | 90 | 20 | -73.69335 | -35.10032 |
| **$M_w$ 9.0C** | 3.1 | 600 | 130 | 7.6 | 12 | 90 | 20 | -74.88442 | -38.83812 |
| **$M_w$ 9.0S** | 5.3 | 600 | 130 | 6.8 | 12 | 90 | 20 | -75.47577 | -42.90477 |

I used previous work and historical records to define the boundaries between the northern, central, and southern modeling sites. The boundary of south-central Chile is noted as 38-41°S from published documents (Veblen et al., 1981; Martin et al., 1999; Munoz et al., 2000; Ely et al., 2014); defined by the general location of the onland central valley. However, I extended the computational domain for my models to lie between 35-43°S (from La Trinchera to southern Chiloe Island). I also extended the subfaults north of the Arauco Peninsula because that region was a site of earthquake rupture overlap from the 1960 $M_w$ 9.5 and the 2010 $M_w$ 8.8 earthquakes (Bilek, 2009; Melnick et al., 2012). I also extended my subfaults farther to the south because I wanted my modeling domain to reach the paleotsunami deposit sites at Maullin, Caulle, Chucalen, Cocotue, Chepu, and Lake Huelde, and the historical sites at Ancud and Castro. I subdivided the south-central

region into three equally spaced parts: the northern (35-37.2°S), central (37.3-40.1°S), and southern (40.2-43°S) sections (Figure 6).


Figure 6: Modeling domain from La Trinchera to Chiloe Island, divided into 3 sections: the northern, central, and southern portions. Towns are marked as a point of reference.

Previously published work in Chile on recent earthquakes, such as 1960, 2010, and 2015, provides examples of realistic fault length, width, and average slip scenarios (c.f. Delouis, et al., 2010; Vigny et al., 2011; Fujii and Satake, 2013; Moernaut et al., 2014; Li et al., 2016; Omira et al., 2016), which I used to define the length/width/slip of my earthquake scenarios. Using tsunami waveform data from the $M_w$ 9.5 1960 earthquake, Fujii and Satake (2013) and Moernaut et al. (2014) calculated a rupture length of at least 900 km, 13-25 m estimated slip near the trench, and 140-150 km width. Studies of the smaller $M_w$ 8.8 2010 Maule earthquake indicate length estimates of 400-500 km along strike (Fujii and Satake, 2013; Moernaut et al., 2014; Omira et al., 2016), rupture width around 120 km-180 km (Delouis, et al., 2010; Vigny et al., 2011; Fujii and Satake, 2013; Omira et al., 2016), and the slip within the hypocentral area of 4-10 m (Delouis, et al., 2010; Vigny et al., 2011; Fujii and Satake, 2013). The $M_w$ 8.3 2015 Illapel earthquake had a rupture length greater than 200 km (An et al., 2014; Li et al., 2016; Omira et al., 2016), a rupture width of 160 km (An et al., 2014; Omira et al., 2016), and a slip of ~3 m (An et al., 2014; Li et al., 2016; Omira et al., 2016). Geophysicists studying these great earthquakes in Chile incorporated tsunami observations (Delouis, et al., 2010; Vigny et al., 2011; Fujii and Satake, 2013; An et al., 2014; Omira et al., 2016), into their finite-fault inversion determinations to improve accuracy of their slip model.

Using the known length, width, and slip of real events on the Chilean subduction zone as a foundation, I selected length, width, and slip values to best represent the $M_w$ 8.6, 8.8, and 9.0 hypothetical earthquakes. For the $M_w$ 8.8 rupture scenarios, I chose a

length of 500 km, width of 120 km, and a slip of 8 m (Table 2) to closely agree with the $M_w$ 8.8 2010 Maule rupture dimensions. Because neither of my $M_w$ 8.6 and 9.0 earthquake scenarios matched recent events, I used the published rupture dimensions for the $M_w$ 9.5 1960 earthquake to help guide my dimensions for a hypothetical $M_w$ 9.0 earthquake, and the $M_w$ 8.3 2015 earthquake to help guide my dimensions for a hypothetical $M_w$ 8.6 earthquake.

I scaled down the length and width of the $M_w$ 9.5 earthquake dimensions using a similar length to width scaling ratio (roughly 5:1 in this case) and chose a smaller slip based on the moment magnitude and scalar seismic moment equations (Fowler, 1990; Kanamori, 1978):

- $M_w = \frac{2}{3}\ log_{10}(M_0) - 10.7$
- $M_0 =\ Area\ of\ rupture\ \times Average\ slip \times shear\ modulus\ (4 \times 10^{10}\ N\ m^{-2})$[1].

The $M_w$ 9.0 rupture dimensions I calculated were a length of 600 km, width of 130 km, and a slip of 12 m (Table 2). The equation for these inputs gave an earthquake of the size $M_w$ = 9.01. Ultimately, the scaling ratio is 4:1 for my $M_w$ 9.0 rupture, thus the $M_w$ 9.5 rupture should be longer than my $M_w$ 9.0 rupture, but roughly having similar widths.

Earthquake width is confined by the maximum width of the seismogenic zone, calculated as 150 km for northern Chile (Comte et al., 1994; Haberland et al., 2009). I

[1]Shear modulus taken from Gusman et al. (2014).

calculated the maximum possible width of any earthquake rupture for south-central Chile as 145 km using the following equation (Zakharova et al., 2013):

Width = seismogenic depth average / sin (average dip angle).

The seismogenic depth average is 45 km (Tichelaar and Ruff, 1991) and the average dip, extracted from the Slab 1.0 model for my modeling space, is 18°.

Because the published data on the rupture dimensions for the $M_w$ 8.3 2015 earthquake should be smaller than those of my hypothetical $M_w$ 8.6 dimensions, I chose a slightly wider and longer rupture using a length to width scaling ratio similar to the $M_w$ 8.3 (roughly 2:1 in this case) and larger slip. The inputs I ultimately chose for the $M_w$ 8.6 rupture dimensions had a length of 400 km, width of 110 km, and a slip of 5 m (Table 2).

Because I have known rupture parameters for all 3 of my $M_w$ 8.6, 8.8, and 9.0 earthquakes constructed from past events, I am able to constrain rupture lengths and widths for hypothetical $M_w$ 8.5, 8.7, 8.9, and 9.1, etc. earthquakes. Each increase in $M_w$ by 0.1 was an increase in 50 km in length, and 5 km in width when I assembled all parameters consecutively (Table 3).

Table 3: My defined earthquake parameters based on actual past events. Bold values are the rupture scenarios I used in this study.

| $M_w$ | length (km) | width (km) |
|---|---|---|
| **8.5** | 350 | 105 |
| **8.6** | **400** | **110** |
| **8.7** | 450 | 115 |
| **8.8** | **500** | **120** |
| **8.9** | 550 | 125 |
| **9.0** | **600** | **130** |
| **9.1** | 650 | 135 |

# CHAPTER IV

# SITE ASSESSMENT METHODS

## Tide Gauge Analysis

To compare simulations with onshore data or with each other, I used synthetic tide gauges to record waveform data from each model run. I created 99 tide gauges near the shoreline and evenly distributed them throughout the northern, central, and southern modeling boundaries, including paleotsunami and historical site locations (Figure 7; Table 4). Analysis of the synthetic tide gauge waveforms enables calculation of arrival times of the tsunami at the tide gauge and wave height highs and lows, and the maximum wave heights allows for projection of tsunami inundation onshore. Although GeoClaw calculates inundation, the resolution of the bathymetry used is not detailed enough for reliable results (e.g., Tang et al. (2009) says 1/3 arc-second, or 10-m, resolution is best for modeling wave runup and inundation). Comparing maximum wave heights at the shoreline to higher resolution (15 m) topography in Google Earth was deemed a more comparable projection of whether a coast would flood for the 99 tide gauge sites. In particular, I took a profile of the beach from Google Earth perpendicular to the gauge and compared the maximum wave height to the shoreline elevation. Low-lying beaches versus cliffs make a huge difference on inundation. Note this method does not consider how far the tsunami inundates onshore. See my Results section for situations where I used higher resolution topography in inundation simulations.

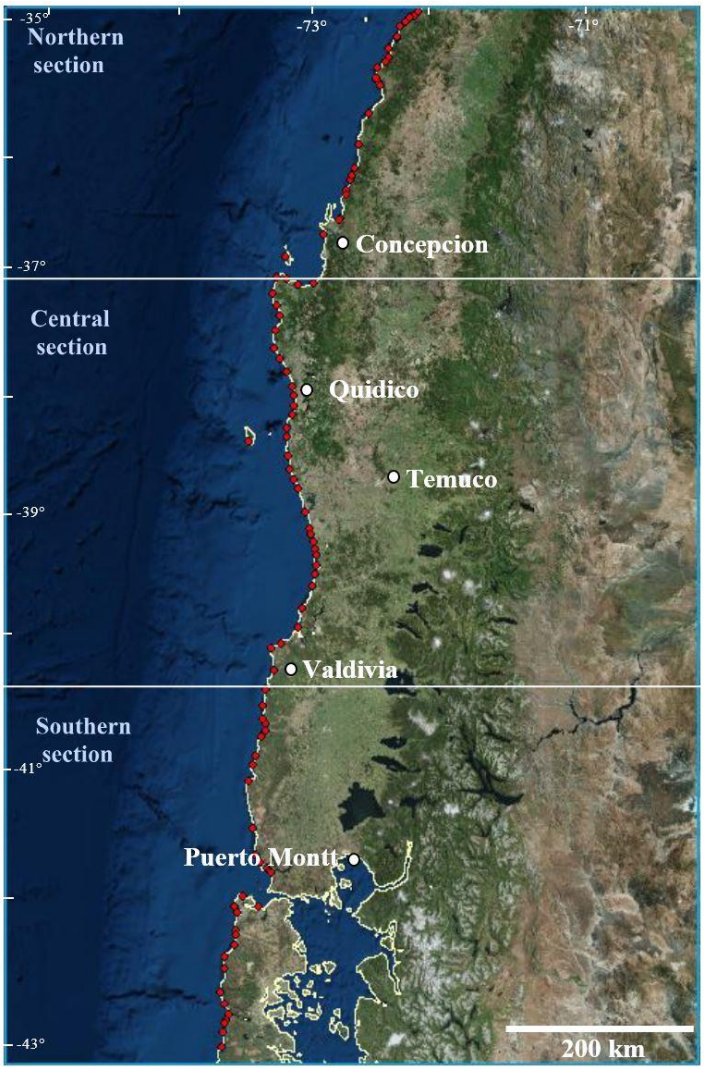


Figure 7: Distribution of 99 tide gauges by region; 33 tide gauges in each. Tide gauges are located <1 km offshore at <10-m water depth.

Table 4: Locations of my 99 tide gauges placed offshore of Chile's coast. The dataset consists of locations that have tsunami deposits and/or written historical accounts of past earthquakes/tsunamis. A blank dataset indicates no record of tsunami deposits or historical accounts at that site.

| Tide gauge # | lon | lat | dataset | notes |
|---|---|---|---|---|
| **1** | -72.205074 | -35.102322 | Tsunami deposit | La Trinchera |
| **2** | -72.221655 | -35.119193 | | Matancilla Shores I |
| **3** | -72.250258 | -35.137590 | | Matancilla Shores II |
| **4** | -72.344311 | -35.187172 | | La Lechuza |
| **5** | -72.393178 | -35.223807 | | Matancilla shores |
| **6** | -72.424995 | -35.315883 | Tsunami deposit | Constitucion I |
| **7** | -72.505974 | -35.397130 | | San Antonio |
| **8** | -72.508367 | -35.469572 | | Los Pellines |
| **9** | -72.542174 | -35.500718 | | Los Pellines |
| **10** | -72.617293 | -35.549960 | | Loanco |
| **11** | -72.634567 | -35.634621 | | Laguna Reloca (Empedrado) |
| **12** | -72.611066 | -35.658897 | | Laguna Reloca (Empedrado) |
| **13** | -72.597427 | -35.689170 | | Laguna Reloca (Empedrado) |
| **14** | -72.705478 | -35.910505 | | Chevelle |
| **15** | -72.812781 | -36.144073 | | Colmuya |
| **16** | -72.849311 | -36.327536 | | Rio Itata |
| **17** | -72.878722 | -36.402668 | | Rio Itata |
| **18** | -72.888802 | -36.422054 | | Rio Itata |
| **19** | -72.936529 | -36.503590 | Tsunami deposit | Coliumo |
| **20** | -72.995646 | -36.727037 | Historical account | Penco |
| **21** | -73.163499 | -36.846262 | Historical account | Concepcion |
| **22** | -73.270702 | -37.220920 | | El Paraiso |
| **23** | -73.640175 | -37.178959 | | Yani Dunes at Locobe |
| **24** | -73.637956 | -37.391833 | | Yani Dunes at Locobe |
| **25** | -73.604598 | -37.468789 | | North of Quidico |
| **26** | -73.608663 | -37.798000 | Historical account | Angol |
| **27** | -73.540263 | -37.898538 | | Playa Llancao |
| **28** | -73.480821 | -38.011591 | | West of Guape |
| **29** | -73.477270 | -38.229607 | Both | Quidico I |
| **30** | -73.918785 | -38.433394 | Historical account | Mocha Island |
| **31** | -73.426751 | -38.785320 | Both | Puerto Saavedra |

Table 4 (Continued): Locations of my 99 tide gauges placed offshore of Chile's coast. The dataset consists of locations that have tsunami deposits and/or written historical accounts of past earthquakes/tsunamis. A blank dataset indicates no record of tsunami deposits or historical accounts at that site.

| Tide gauge # | lon | Lat | dataset | notes |
|---|---|---|---|---|
| **32** | -73.252472 | -39.235947 | Tsunami deposit | Tolten abandoned meander |
| **33** | -73.236882 | -39.282046 | Tsunami deposit | Nique Norter |
| **34** | -73.275059 | -39.515168 | | South of Maiquiahue |
| **35** | -73.420704 | -39.826019 | Both | Valdivia |
| **36** | -73.668284 | -40.136939 | | North of Hueicolla |
| **37** | -73.755605 | -40.281145 | | El Farellon |
| **38** | -73.848107 | -41.483584 | | Los Muermos |
| **39** | -73.806839 | -41.544346 | | top of archipelago and north shores |
| **40** | -73.734149 | -41.580752 | | top of archipelago and north shores |
| **41** | -73.698227 | -41.617690 | Both | Maullin inland tsunami sand |
| **42** | -73.709798 | -41.607454 | Tsunami deposit | Caulle |
| **43** | -73.976269 | -41.789558 | | North of Guabun (top of archipelago) |
| **44** | -73.819166 | -41.857379 | Historical account | Ancud |
| **45** | -74.059594 | -41.862508 | Tsunami deposit | Chucalen |
| **46** | -74.029881 | -41.905463 | Tsunami deposit | Cocotue on Isla Chiloe |
| **47** | -74.046731 | -42.025874 | | North of Chepu |
| **48** | -74.048317 | -42.060020 | Tsunami deposit | Chepu |
| **49** | -74.160056 | -42.219651 | | Penguins |
| **50** | -74.159853 | -42.555899 | | South of Huentemo |
| **51** | -74.143862 | -42.677466 | | North of Rahue I |
| **52** | -74.146359 | -42.677000 | | Rahue II |
| **53** | -74.162424 | -42.695099 | | Playa Rio Catiao |
| **54** | -74.196800 | -42.862732 | | Paso Huencho |
| **55** | -72.211204 | -35.109678 | | Los Rabanos |
| **56** | -72.291025 | -35.152635 | | Matancilla/Cuchi |
| **57** | -72.641472 | -35.626250 | | South of Loanco |
| **58** | -72.877568 | -36.390076 | | South of Mocha Island |
| **59** | -73.009698 | -36.735227 | Tsunami deposit | Andalien |
| **60** | -73.536995 | -38.328062 | | Tirua |
| **61** | -73.240193 | -39.281829 | | West of Puraloco |
| **62** | -73.695780 | -41.618597 | | West of Maullin |

Table 4 (Continued): Locations of my 99 tide gauges placed offshore of Chile's coast. The dataset consists of locations that have tsunami deposits and/or written historical accounts of past earthquakes/tsunamis. A blank dataset indicates no record of tsunami deposits or historical accounts at that site.

| Tide gauge # | lon | Lat | dataset | notes |
|---|---|---|---|---|
| **63** | -72.940842 | -36.537509 | Tsunami deposit | Dichato |
| **64** | -73.231968 | -39.358523 | Tsunami deposit | Queule |
| **65** | -73.246352 | -39.427001 | Tsunami deposit | Missisipi |
| **66** | -74.126936 | -42.634988 | Tsunami deposit | Lake Huelde/Cucao |
| **67** | -72.425000 | -35.304347 | Tsunami deposit | Constitucion II |
| **68** | -73.427520 | -37.234248 | Tsunami deposit | Tubul |
| **69** | -73.536340 | -37.194142 | Tsunami deposit | Llico |
| **70** | -73.550815 | -37.016655 | Historical account | Santa Maria |
| **71** | -73.595580 | -39.943859 | Tsunami deposit | Chaihuin |
| **72** | -73.743268 | -40.535364 | Tsunami deposit | Pucatrihue |
| **73** | -73.678826 | -37.301608 | | Cerro La Gloria |
| **74** | -73.656497 | -37.583719 | | Lebu |
| **75** | -73.664810 | -37.715658 | | West of Santa Rosa + Pelahuenco |
| **76** | -73.461696 | -38.084088 | | West of Lago Lleulleu |
| **77** | -73.461237 | -38.164123 | Tsunami deposit | Quidico II |
| **78** | -73.539431 | -38.395718 | | Bio |
| **79** | -73.517210 | -38.537099 | | La Peuca |
| **80** | -73.50226 | -38.639643 | | West of Champulli |
| **81** | -73.470454 | -38.717915 | | Northern Puerto Saavedra |
| **82** | -73.349301 | -38.957609 | | Huente |
| **83** | -73.303089 | -39.081303 | | Chelle |
| **84** | -73.286596 | -39.127511 | | Reduccion Porma |
| **85** | -73.270188 | -39.18095 | Tsunami deposit | Nueva Tolten |
| **86** | -73.381214 | -39.68138 | | Cerro Oncol |
| **87** | -73.688072 | -39.97955 | | Huiro |
| **88** | -73.77335 | -40.404205 | | North of Playa Diaz |
| **89** | -73.784423 | -40.496665 | | Playa El Manzano |
| **90** | -73.756409 | -40.587047 | | Bahia Mansa |
| **91** | -73.795497 | -40.627618 | | Tril tril |
| **92** | -73.854036 | -40.763667 | | Caleta condor |
| **93** | -73.883587 | -40.830565 | | North of Manquemapu |

Table 4 (Continued): Locations of my 99 tide gauges placed offshore of Chile's coast. The dataset consists of locations that have tsunami deposits and/or written historical accounts of past earthquakes/tsunamis. A blank dataset indicates no record of tsunami deposits or historical accounts at that site.

| Tide gauge # | lon | Lat | dataset | notes |
|---|---|---|---|---|
| **94** | -73.921037 | -40.946712 | | South of Guayusca |
| **95** | -73.872441 | -41.290668 | | Rio Llico |
| **96** | -74.061677 | -42.131677 | | Parque Ahuenco |
| **97** | -74.159417 | -42.310498 | | Abtao |
| **98** | -74.200971 | -42.471316 | | Playa Rio Anay |
| **99** | -74.181006 | -42.758174 | | Campihuapi |

## Promising Sites

One of the ultimate goals in this project is to identify the most promising sites on Chile's coast useful for future studies on paleotsunami modeling in this area. The definition of a promising site is a location onshore that magnifies differences between wave heights of tsunamis and therefore filters the earthquake magnitude and/or source location. I started with numerical analysis to narrow down possible promising sites, and then qualitatively assessed the individual sites to choose the best sites.

My numerical analysis used the maximum wave heights for all nine simulated tsunamis at each of my 99 synthetic tide gauges. At each tide gauge location, I calculated the minimum difference between all nine simulations with the following equation, and repeated for all 99 tide gauge sites:

$$\varepsilon = \min[(|h_i - h_1|), (|h_i - h_2|), \dots, (|h_i - h_9|)] \text{ for } h_i \neq h_1, h_i \neq h_2, \text{ etc.,}$$

where $\varepsilon$ is the minimum spacing of tsunami wave heights between all nine simulations, min[(a),(b),…,(z)] is the minimum value out of the following list of variables, $h_i$ is the

maximum wave height for earthquake $i$, and $h_{1-9}$ is the maximum wave height for simulations 1-9. The variables $h_i$ and $h_{1-9}$ come from wave heights of the following nine simulations: $M_w$ 8.6N, 8.6C, 8.6S, 8.8N, 8.8C, 8.8S, 9.0N, 9.0C, or 9.0S (Table 2), and the equation does not allow duplicates to cancel out each other.

I then averaged all nine tsunami values for minimum spacing between wave heights ($\varepsilon$) to get a numerical value representing the average minimum difference perceivable between each tsunami wave, and extended these averages for all 99-tide gauge sites. I used the assumption that an average of 0.50 m or greater is necessary for wave height variability in the historical and paleotsunami record to be perceived onland. As such, tide gauges where the average minimum difference was <0.50 m were considered not promising. To verify 0.50 m with paleotsunami records, maximum tsunami wave heights are recorded to the nearest 0.1 m, so a difference in 0.50 m between wave heights would be observed onland and recorded as such.

I also applied this method to arrival times, or the time at the beginning of a tsunami wave, and assumed 5 minutes as the minimum difference for tsunami wave arrivals. I could not verify 5 minutes in the paleotsunami record, but I could with modern examples knowing that arrival times are comparable to the distance of the earthquake source location (Fujii et al., 2011). To verify 5 minutes, I used the following fluid dynamics equation for wave dispersion:

$$c = \sqrt{g \times h},$$

where c is the phase velocity of the traveling tsunami wave, g is the acceleration due to gravity, and h is the average water depth from the earthquake source to my tide gauge location. A travel time of 5 minutes coincided with the distance of my source locations.

Averaging the minimum difference in wave heights is the best method for evaluating differences in tsunami effects because the difference allows expression of the highest and lowest wave heights. Just averaging the wave heights as a start would not best illustrate the sites that magnify wave height differences. I did not take the minimum values for both steps because if the lowest wave height was 0 m from the nine simulations, wave heights greater than zero would not be expressed. Finally, I chose not to use the following standard deviation equation:

$$\text{Standard deviation} = \sqrt{\left[\frac{(\sum_{i=1}^{n}(x_i-\bar{x})^2)}{n-1}\right]},$$

where $n$ is the number of data points, $\bar{x}$ is the mean of $x_i$, and $x_i$ is each of the values in the data set. Although standard deviation calculates the "spread" of a dataset, the first step takes the mean of the tsunami wave heights, then subtracts the mean from all nine data points as a second step, which is not the best way to represent magnification of wave height differences at each site. However, the standard deviation equation shows the same group of possible promising sites as my equation (but in a different order).

After I established a list of statistically promising sites, I qualitatively analyzed these locations to determine whether the site was likely to contain preserved tsunami deposits. I used the following factors to aid in my evaluation of a promising site in decreasing order of importance: the site is already in my list of known paleotsunami or

historical site database, the topography was low-lying, flat and open, or the site has a town or neighboring city. If the site did not have known paleotsunami deposits there or historical documentation of past earthquakes or tsunamis, I used Google Earth to assess whether the coastal topography was capable of being inundated by a tsunami, such as being a coastal marsh, coastal inlet or embayment, or a river outlet.

Once I established my final list of promising sites, I evaluated whether the topography allowed tsunami inundation at river banks (if the site had nearby river outlets), at the beach, and/or past the berm. This is an important analysis because even if the site filtered tsunamis by size or location, and had flat lying topography, water still must flood the coastal plain for a deposit to be left in the geological record. If the maximum wave height from the tide gauges surpassed the elevation of the berm, I assumed inundation would take place past the berm and termed this "heavy inundation" that goes beyond just shoreline inundation. This method does not account for the location of the inundation limit. If an area has no berm or is mostly flat, heavy inundation will take place if the maximum wave height exceeds the highest elevation in the area.

### High-Resolution Data

The 30-arcsecond resolution of bathymetry and topography used in GeoClaw is not detailed enough to model the dynamics of inundation. 1/3-arcsecond (~10 m) resolution is ideal for simulating wave runup and inundation (Tang et al., 2009), so I aimed to make additional high-resolution simulations. I acquired 5-m and 12-m

resolution digital surface models at 6 total sites (independent from my analysis of promising sites): Andalien, Lenga, Puerto Saavedra, Queule, Quidico, and Tirua (Figure 8). Within ArcGIS, I merged these high-resolution topography files with the existing GEBCO dataset, thereby improving the resolution of the GEBCO file. With these new bathymetry/topography, I created grids for high-resolution inundation simulations at all 6 coverage areas and two additional subgrids, because Puerto Saavedra and Queule are too large to calculate inundation at the highest resolution over the whole site. At both of these locations, I divided into 2 sites. The resulting raster resolution for these sites was 0.40" (~12 m per grid cell) for both Lenga and Andalien, 0.28" (~9 m) for a small part of Queule, 0.61" (~19 m) for the entire Queule site, 0.23" (~7 m) for Quidico, 0.31" (~10 m) for Tirua, 0.40" (~12 m) for a small part of Puerto Saavedra, and 3.05" (~94 m) for the entire Puerto Saavedra site.


Figure 8: The location of six sites with high-resolution topography (orange lettering). Puerto Saavedra and Queule were subdivided into two boxes, 1 at high-resolution over a small area, and 2 at lower resolution but covering the extent of the available topography.

GeoClaw used these rasters to create maximum inundation maps at these locations, marking the extent of the highest waves, and mapping the maximum wave heights. Once GeoClaw created these high-resolution topography/bathymetry inundation maps, I used them in accordance with maximum wave heights from my tide gauges on

the lower 30” resolution topography/bathymetry to further assess tsunami inundation. For sites where only 30” topography/bathymetry was available, I relied solely on my assessments in Google Earth.

# CHAPTER V

# RESULTS

## Seafloor Deformation from Earthquake Scenarios

My earthquake input parameters resulted in wider seafloor deformation for larger width earthquakes. For example, the $M_w$ 8.6 earthquakes, 110-km wide, had a deformation width of 190 km, the $M_w$ 8.8 earthquakes, 120-km wide, had a deformation width of 210-240 km, and the $M_w$ 9.0 earthquakes, 130-km wide, had a deformation width of 270-280 km (Table 5). The width of deformation defines the wavelength of the tsunami and larger rupture width, with the same amount of slip, creates larger moment release.

Table 5: Deformation of the seafloor from each rupture scenario including the width, location of the hinge line, and maximum and minimum seafloor change. Average distance was calculated with the measuring tool in ArcGIS.

| Rupture scenario | width of deformation (km) | hinge line location | average distance from hingeline to shoreline (km) | highest uplift (m) | lowest subsidence (m) |
|---|---|---|---|---|---|
| **86N** | 190 | half onshore/offshore | 41 | 1.5 | -0.8 |
| **86C** | 190 | offshore, except for the Arauco Penin. | 37 | 1.5 | -0.8 |
| **86S** | 190 | offshore | 10 | 1.5 | -0.8 |
| **88N** | 210 | half onshore/offshore | 22 | 2.4 | -1.2 |
| **88C** | 220 | mostly offshore, except for the Arauco Penin. | 28 | 2.4 | -1.2 |
| **88S** | 240 | mostly onshore, except for above and below Chiloe | 12 | 2.4 | -1.2 |
| **90N** | 270 | half onshore/offshore | 26 | 3.9 | -1.7 |
| **90C** | 280 | half onshore/offshore | 19 | 3.8 | -1.7 |
| **90S** | 280 | mostly onshore, except for above and below Chiloe | 11 | 3.8 | -1.7 |

The Okada (1985) solution for seafloor deformation from my nine earthquake scenarios resulted in both coseismic uplift and subsidence (Figure 9). Between all three northern, central, and southern source locations, larger earthquakes produced larger values of uplift and subsidence (Tables 6-8). However, coastal sites had uplift and subsidence values that varied due to location. Of the three $M_w$ 8.6 ruptures, coastal deformation was 0.7-m average subsidence, except 0.3-m uplift at Concepcion (Figure 9). The $M_w$ 8.8 ruptures produced 1.2-m uplift on average at Dichato, Concepcion, and the Arauco Peninsula (Figure 9), with the central and southern rupture's hinge lines (the boundary between subsidence and uplift) close to the coast for this earthquake, resulting in little land-level change south of Valdivia (Figure 9). The central and southern $M_w$ 9.0 ruptures produced 0.6-m uplift on average at Tirua, Cocotue, and Lake Huelde, but the northern rupture produced 3.2-m uplift on the Arauco Peninsula and the central rupture produced 1.7-m subsidence north of Valdivia (Figure 9). Overall, the $M_w$ 9.0 rupture resulted in greater values of subsidence than the $M_w$ 8.8 or 8.6 ruptures, and produced higher uplift between Dichato and Quidico than the smaller ruptures (Figure 9).

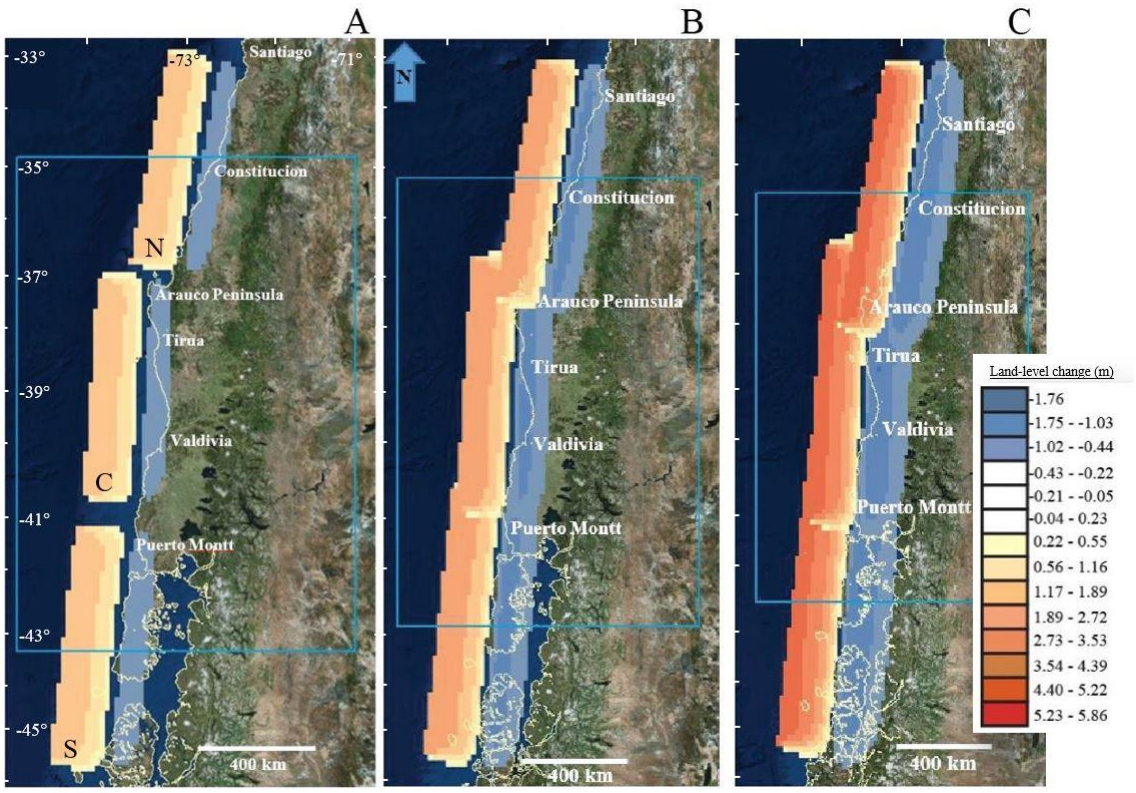


Figure 9: Seafloor deformation for the $M_w$ 8.6 (A), $M_w$ 8.8 (B), and $M_w$ 9.0 (C) earthquakes calculated in GeoClaw with place names mentioned in text. Blue box is the section of coast I analyzed. Image from ArcGIS.

Table 6: Uplift and subsidence for the northern scenarios.

| Tide gauge | land-level change (m) | | |
|---|---|---|---|
| | Mw 8.6N | Mw 8.8N | Mw 9.0N |
| 1 | -0.6 | -1.3 | -1.7 |
| 55 | -0.6 | -1.3 | -1.7 |
| 2 | -0.6 | -1.3 | -1.7 |
| 3 | -0.7 | -1.2 | -1.2 |
| 56 | -0.7 | -1.2 | -1.2 |
| 4 | -0.7 | -1.3 | -1.3 |
| 5 | -0.8 | -1.0 | -0.7 |
| 67 | -0.8 | -1.1 | -0.8 |
| 6 | -0.7 | -1.1 | -0.2 |
| 7 | -0.7 | -0.7 | -0.4 |
| 8 | -0.8 | -0.8 | -0.4 |
| 9 | -0.8 | -0.8 | -0.4 |
| 10 | -0.5 | -0.3 | 0.4 |
| 57 | -0.6 | -0.4 | 0.2 |
| 11 | -0.6 | -0.4 | 0.2 |
| 12 | -0.6 | -0.5 | 0 |
| 13 | -0.6 | -0.5 | 0 |
| 14 | -0.6 | -0.1 | 0.5 |
| 15 | -0.2 | 0.2 | 1 |
| 16 | -0.3 | 0 | 0.7 |
| 58 | 0 | 0.4 | 1.3 |
| 17 | 0 | 0.4 | 1.3 |
| 18 | 0 | 0.4 | 1.3 |
| 19 | -0.1 | 0.3 | 1.1 |
| 63 | -0.1 | 0.3 | 1.1 |
| 20 | 0.1 | 0.7 | 1.5 |
| 59 | 0.1 | 0.7 | 1.5 |
| 21 | 0.6 | 1.4 | 2.5 |
| 70 | 0.1 | 2.0 | 3.3 |
| 23 | -0.1 | 1.7 | 3.4 |
| 69 | -0.1 | 1.6 | 3.5 |
| 22 | -0.1 | 1.2 | 2.6 |
| 68 | -0.1 | 1.4 | 3.0 |

Table 7: Uplift and subsidence for the central scenarios.

| Tide gauge | land-level change (m) | | |
|---|---|---|---|
| | **Mw 8.6C** | **Mw 8.8C** | **Mw 9.0C** |
| **73** | -0.2 | 0.8 | 1.7 |
| **24** | -0.2 | 0.1 | 0.9 |
| **25** | -0.3 | 0 | 0.9 |
| **74** | -0.3 | 0 | 0.8 |
| **75** | -0.4 | 0.6 | 0.7 |
| **26** | -0.4 | 0 | 0.7 |
| **27** | -0.7 | -0.7 | -0.2 |
| **28** | -0.7 | -0.8 | -0.3 |
| **76** | -0.8 | -1.2 | -1.0 |
| **77** | -0.8 | -1.2 | -1.1 |
| **29** | -0.8 | -0.8 | -0.4 |
| **60** | -0.8 | -0.9 | -0.4 |
| **78** | -0.8 | -0.9 | -0.5 |
| **30** | 0.6 | 1.2 | 2.2 |
| **79** | -0.8 | -1.0 | -0.6 |
| **80** | -0.8 | -1.0 | -0.7 |
| **81** | -0.8 | -1.0 | -0.7 |
| **31** | -0.8 | -1.3 | -1.3 |
| **82** | -0.6 | -1.2 | -1.7 |
| **83** | -0.6 | -1.2 | -1.7 |
| **84** | -0.5 | -1.2 | -1.7 |
| **85** | -0.5 | -1.2 | -1.7 |
| **32** | -0.5 | -1.0 | -1.7 |
| **61** | -0.5 | -1.0 | -1.7 |
| **33** | -0.5 | -1.0 | -1.7 |
| **64** | -0.5 | -1.0 | -1.7 |
| **65** | -0.5 | -1.0 | -1.7 |
| **34** | -0.4 | -1.1 | -1.7 |
| **86** | -0.5 | -1.3 | -1.6 |
| **35** | -0.6 | -1.2 | -1.6 |
| **71** | -0.7 | -0.9 | -0.5 |
| **87** | -0.7 | -0.4 | 0.2 |
| **36** | -0.7 | -0.5 | 0.1 |

Table 8: Uplift and subsidence for the southern scenarios.

| Tide gauge | land-level change (m) | | |
|---|---|---|---|
| | **Mw 8.6S** | **Mw 8.8S** | **Mw 9.0S** |
| **37** | -0.1 | -0.1 | 0 |
| **88** | -0.1 | -0.2 | 0 |
| **89** | -0.1 | -0.3 | 0 |
| **72** | -0.1 | -0.3 | -0.6 |
| **90** | -0.1 | -0.3 | 0 |
| **91** | -0.1 | -0.3 | 0 |
| **92** | -0.1 | -0.2 | 0.5 |
| **93** | -0.1 | -0.2 | 0.5 |
| **94** | -0.2 | -0.3 | 0.3 |
| **95** | -0.5 | -0.6 | 0 |
| **38** | -0.7 | -1.1 | -0.9 |
| **39** | -0.7 | -1.1 | -0.1 |
| **40** | -0.7 | -1.2 | -1.5 |
| **42** | -0.6 | -1.2 | -1.5 |
| **41** | -0.6 | -1.2 | -1.5 |
| **62** | -0.6 | -1.2 | -1.5 |
| **43** | -0.6 | -0.5 | 0.2 |
| **44** | -0.7 | -1.2 | -1.2 |
| **45** | -0.3 | 0.1 | 0.8 |
| **46** | -0.6 | -0.5 | 0.1 |
| **47** | -0.7 | -0.6 | 0 |
| **48** | -0.7 | -0.6 | -0.1 |
| **96** | -0.4 | -0.1 | 0.6 |
| **49** | -0.1 | 0.3 | 1.2 |
| **97** | -0.1 | 0.3 | 1.1 |
| **98** | -0.3 | 0.2 | 1 |
| **50** | -0.3 | 0.1 | 0.9 |
| **66** | -0.6 | -0.5 | 0.1 |
| **52** | -0.6 | -0.6 | 0 |
| **51** | -0.6 | -0.6 | 0 |
| **53** | -0.3 | 0 | 0.8 |
| **99** | -0.4 | 0 | 0.8 |
| **54** | -0.4 | 0 | 0.6 |

At maximum, the western-most location of the hinge line separating uplifted areas from subsided regions was 80 km from the shoreline in the $M_w$ 8.6 rupture scenario (Table 5). Earthquakes with wider ruptures produced a hinge line more eastward (Figure 9). The $M_w$ 8.6 earthquake produced a hinge line between Colmuya and Concepcion for the northern earthquake, between the Arauco Peninsula and Angol for the central earthquake, and south of Campihuapi for the southern earthquake (Figure 9). The $M_w$ 8.8 earthquake produced a hinge line farther northeast for both the northern (between Loanco and Concepcion) and southern (between Cocotue and Lake Huelde) earthquakes compared to the $M_w$ 8.6 earthquake, with no change for the central earthquake (Figure 9). The $M_w$ 9.0 earthquake produced a hinge line farther southeast for the southern earthquake (Figure 9) compared to the $M_w$ 8.8 earthquake, but the northern and central earthquakes produced no change in hinge line location.

Coseismic subsidence and uplift values from all nine scenarios can be compared to field data for all locations where we have paleoseismic or historical records (Tables 6-8). The northern $M_w$ 8.8 earthquake rupture extent and seismic moment are equivalent to the 2010 Maule earthquake (Delouis et al., 2010; Fujii and Satake, 2013; Moernaut et al., 2014; Omira et al., 2016). Observations for land-level change during the 2010 Maule earthquake reported up to 2.5-m uplift in the Arauco Peninsula (37.1º S-37.7º S; Farias et al., 2010) and 2.4-3 m of uplift on Isla Santa Maria (Wesson et al., 2015). For the comparable $M_w$ 8.8 northern rupture scenario, the Arauco Peninsula uplifted at slightly smaller values: 1.4-m at Tubul, 2.0-m at the uppermost tip of Punta Lavapie (Tubul and

Punta Lavapie are on the Arauco Peninsula), and 2.0-m on Isla Santa Maria (Figure 10). Therefore, uplift is ~20% less, but relatively similar. As such, I conclude that the 2010 tsunami observations can be compared to my simulated $M_w$ 8.8 northern wave heights.

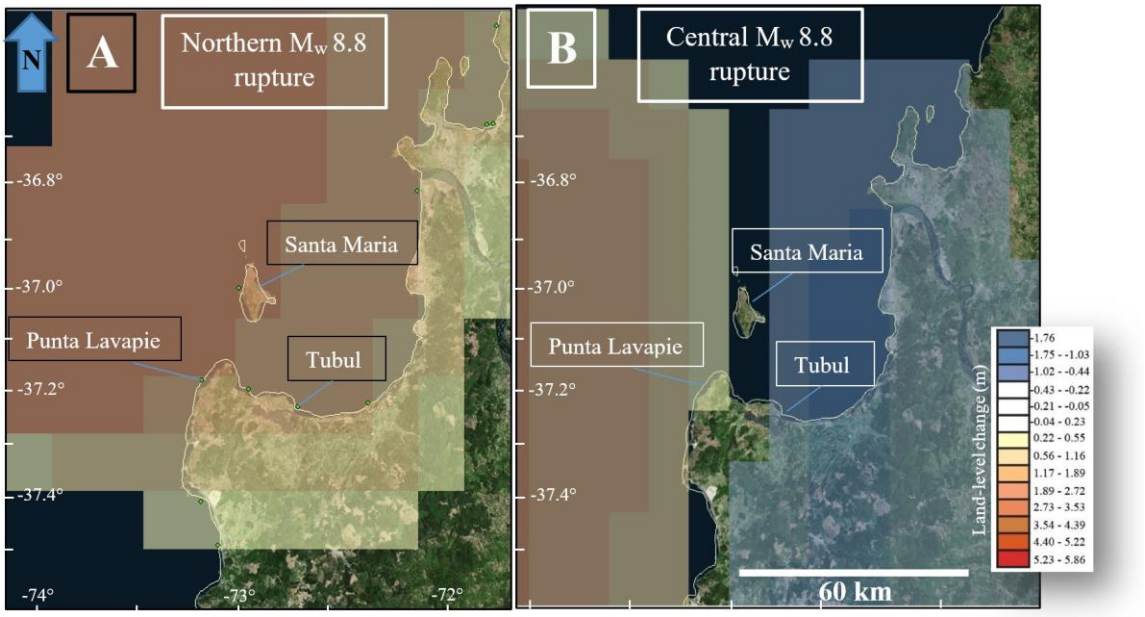


Figure 10: Box A- Coseismic land-level change for a northern $M_w$ 8.8 rupture showing uplift at Santa Maria, Punta Lavapie, and Tubul. Box B- Coseismic land-level change for a central $M_w$ 8.8 rupture showing uplift at Punta Lavapie, subsidence at Tubul, and neither uplift nor subsidence at Santa Maria. Color scale (right inset) is in meters.

Fault parameter differences, especially slip and rupture width, explain the small disagreement between simulated and observed land-level change values. Rupture for the 2010 earthquake had a width of 150 km and slip concentrations of 13-25 m (Delouis et al., 2010; Fujii and Satake, 2013; Moernaut et al., 2014), while the northern $M_w$ 8.8 scenario's width and slip were smaller at 120 km for width and 12-m uniform slip (Table 2). The magnitude of the slip is an important factor because it reflects strain release and

increases coseismic surface displacement (Wang, 2007; Leonard et al., 2010). The width of the coseismic rupture zone is also an important factor, especially the downdip extent, because it affects the coseismic vertical displacement in two ways (Wang et al., 2003; Leonard et al., 2010). First, the downdip limit of full rupture is shifted landward (Leonard et al., 2010). Second, the rupture width increases the maximum magnitude of vertical deformation (Leonard et al., 2010).

The combined central and south $M_w$ 9.0 earthquake scenarios are equivalent in rupture area and seismic moment to the $M_w$ 9.5 1960 Valdivia earthquake (Fujii and Satake, 2013; Moernaut et al., 2014). The rupture length for the $M_w$ 9.5 1960 earthquake was at least 900 km (Fujii and Satake, 2013; Moernaut et al., 2014) spanning from the uppermost point of my $M_w$ 9.0 central rupture scenario and lowermost point of my $M_w$ 9.0 southern rupture scenario (Figure 9; Figure 3). The 1960 Valdivia earthquake caused 1-2 m of subsidence in Angol (Cisternas et al., 2005), and my $M_w$ 9.0 central scenario at Angol created a similar subsidence of 1.6-m (Figure 9). The 1960 earthquake cause 2.7-m subsidence at Valdivia (Barrientos and Ward, 1990), where my $M_w$ 9.0 southern scenario caused 1.6-m subsidence. The reason the 2010 earthquake caused uplift and the 1960 earthquake caused subsidence may be due to slip extending farther landward and to greater depths for the 2010 rupture than the 1960 rupture (Ely et al., 2014). Therefore, I conclude that the 1960 tsunami observations can be compared to my simulated $M_w$ 9.0 central and southern wave heights.

### Comparison of All Earthquake Scenarios at Simulated Tide Gauges

Wave heights and arrival times at latitudinally distributed tide gauges provide a regional summary of simulated tsunami variations between scenarios (Figure 11-12). Wave heights showed a roughly similar trend between all nine simulations, with wave heights from southern earthquakes being lowest in the northern section and wave heights from northern earthquakes being lowest in the southern section (Figure 11), as expected. Arrival times also showed a predictable trend, with shorter arrival times from northern earthquakes, and longer arrival times from southern earthquakes in the north, for example (Figure 12). Nearfield earthquakes and the $M_w$ 9.0 earthquakes all produced higher wave heights at any given tide gauge as a general trend (Figure 11). As noted above, the $M_w$ 9.0 earthquakes produced generally higher wave heights (Figure 11) and earlier arrival times (Figure 12). The $M_w$ 9.0 earthquakes had hinge lines closer to the shore and more inland, which also was observed during the 1960 earthquake (Metois et al., 2014), and might explain the $M_w$ 9.0 scenario wave heights and early arrival times in the nearshore.

Locations that exemplify expected variation in maximum wave heights, those with distributions with the largest nearfield earthquake producing the highest wave heights to the smallest distant earthquake scenarios producing the smallest, along the coast include Constitucion, Chevelle, Rio Itata, West of Champulli, Puerto Saavedra, North of Hueicolla, and Parque Ahuenco (Figure 11). These sites are all at nearfield locations without complex coastal geomorphology, helping explain their expected wave height differences.

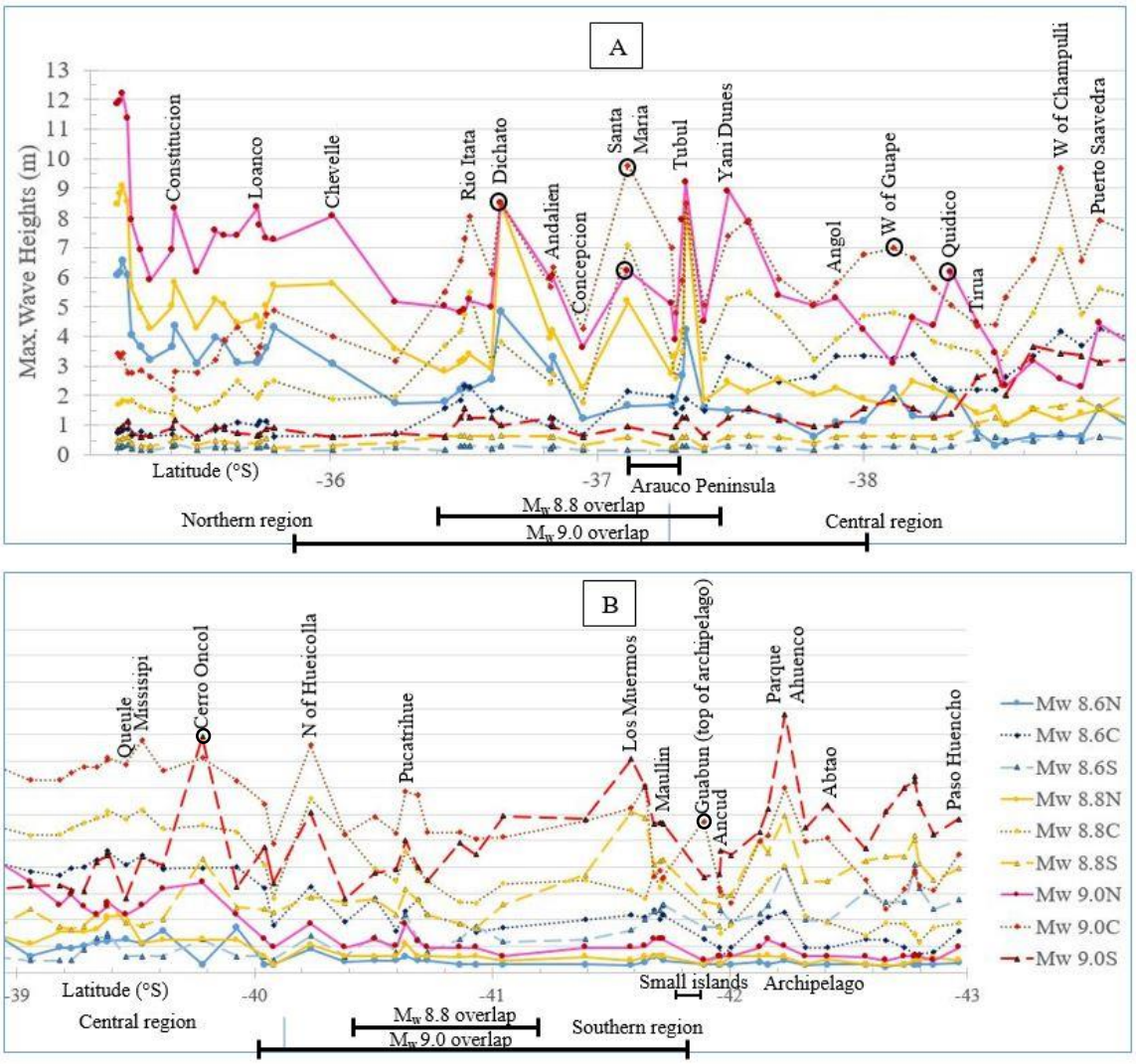


Figure 11: Variation in wave heights from tide gauges along the coast. Boxes A and B are a full graph when placed side-by-side. $M_w$ 8.6 earthquakes are blue, $M_w$ 8.8 earthquakes are yellow, and $M_w$ 9.0 earthquakes are red. Solid lines are northern earthquakes, dotted lines are central earthquakes, and dashed lines are southern earthquakes. Outliers discussed in the text are circled. $M_w$ 8.8 and 9.0 "overlap" indicates the latitudinal extent that these earthquake ruptures overlap. Refer to Figure 9 for full illustration of earthquake ruptures. Labels are place names of interest in the text.

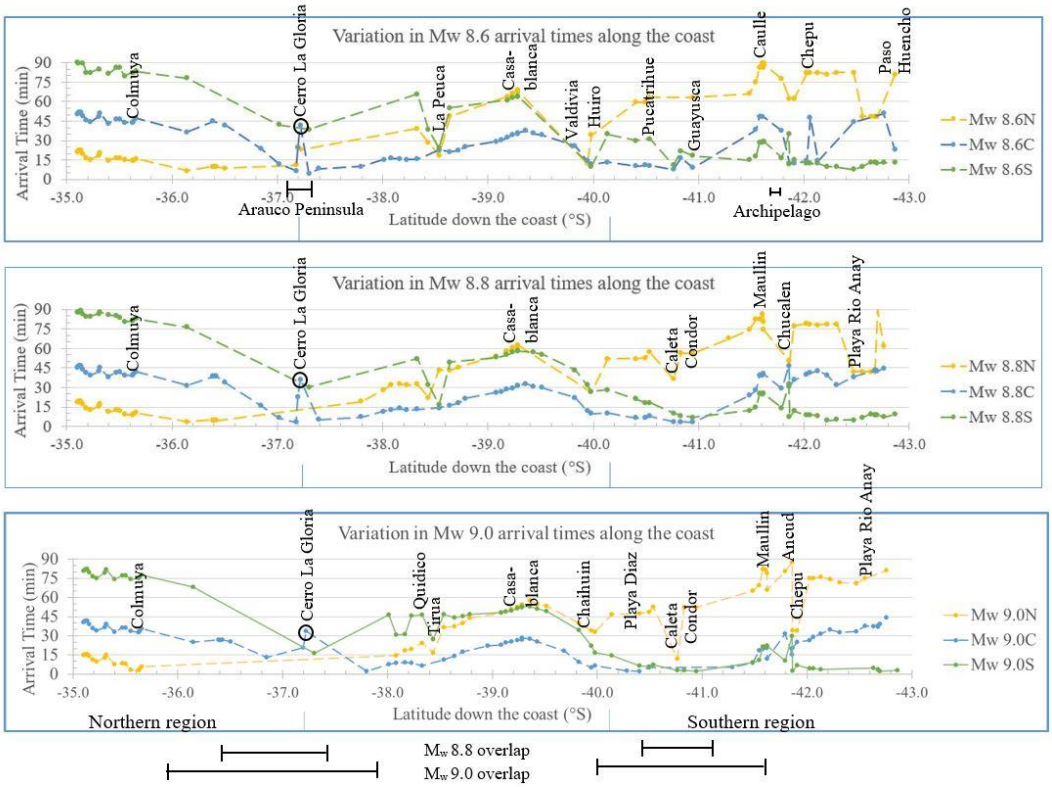


Figure 12: Variation in arrival time at tide gauges along the coast. I removed tide gauges where arrival times could not be determined. Yellow lines are northern earthquakes, blue lines are central earthquakes, and green lines are southern earthquakes. Outliers discussed in the text are circled. $M_w$ 8.8 and 9.0 "overlap" indicates the latitudinal extent that these earthquake ruptures overlap. Refer to Figure 9 for full illustration of earthquake rupture. Labels are place names of interest in the text.

Simulated tsunami wave heights or arrival times along the coast that distinctly differ from the overall trend are defined as outliers. Notable outliers from Figure 11 are mostly concentrated in the north-central region (mainly because of complex topography and shoreline directionality around the Arauco Peninsula). Outliers in wave heights, identified in Figure 11 are at Dichato, Santa Maria, West of Guape, Quidico, Cerro

Oncol, and Guabun. A notable outlier from the variation in arrival times along the coast is at Cerro La Gloria (Figure 12).

### Promising Sites for Magnifying Differences in Tsunami Effects

My numerical analysis of simulated tide gauges resulted in 60% (59/99) of sites having ≥0.5-m mean spacing between wave heights from all nine scenarios (Table 9). Waveforms from 5 sites were spaced ≥5.0 minutes on average between arrival times (Table 10). Out of the 5 sites from arrival time data, 1 site (Campihuapi) was spaced >10 min apart and 4 sites were spaced between 5 and 10 min apart.

With these 60 (59 from wave heights and 1 from arrival times) statistically promising sites, I determined that 22 of those sites had a low-lying marsh and/or flat and open coastal topography that fit a generic model for sites where tsunami inundation is possible to occur and leave tsunami deposits. Out of these final promising sites, all are highly susceptible to flooding (having flat topography, marshy areas nearby, and/or no berm). All $M_w$ 8.6, 8.8, and 9.0 scenarios at these sites would cause tsunami inundation and leave detectable tsunami deposits past the berm based on analysis of beach topography (Appendix A). Of these final promising sites, 21 are from wave height data and 1 is from arrival time data (Table 11). These sites are good places to look for past records of paleoearthquakes to determine their size and location.

Table 9: The average spacing of maximum wave heights from quantitative analysis.

| Dataset (if existing) | tide gauge | average spacing of maximum wave heights (m) | name |
|---|---|---|---|
| | 55 | 1.27 | Los Rabanos |
| | 2 | 1.26 | Matancilla Shores |
| | 3 | 1.16 | Matancilla Shores |
| **Paleotsunami** | 1 | 1.14 | La Trinchera |
| | 80 | 1.00 | West of Champulli |
| **Paleotsunami** | 6 | 0.88 | Constitucion |
| | 24 | 0.87 | Yani Dunes at Locobe |
| **Historical** | 70 | 0.84 | Santa Maria |
| | 56 | 0.83 | Matancilla Shores/Cuchi |
| | 14 | 0.83 | Chevelle |
| **Both** | 57 | 0.82 | offshore of Tirua |
| **Paleotsunami** | 64 | 0.81 | Queule |
| | 22 | 0.79 | El Paraiso |
| | 96 | 0.77 | Parque Ahuenco |
| **Both** | 35 | 0.76 | Valdivia |
| | 11 | 0.76 | Laguna Reloca (Empedrado) |
| **Paleotsunami** | 67 | 0.75 | Constitucion |
| **Paleotsunami** | 85 | 0.73 | Nueva Tolten |
| | 8 | 0.73 | Los Pellines |
| | 83 | 0.71 | Chelle |
| | 34 | 0.71 | South of Maquillahue |
| **Paleotsunami** | 65 | 0.70 | Missisipi |
| | 4 | 0.70 | La Lechuza |
| **Paleotsunami** | 66 | 0.69 | Lake Huelde |
| | 12 | 0.68 | Laguna Reloca (Empedrado) |
| **Both** | 31 | 0.67 | Puerto Saavedra |
| | 23 | 0.66 | Yani Dunes at Locobe |
| | 84 | 0.65 | Reduccion Porma |
| | 82 | 0.65 | Huente |
| | 58 | 0.65 | S of Mocha Island |
| | 13 | 0.64 | Laguna Reloca (Empedrado) |
| **Paleotsunami** | 27 | 0.62 | N of Quidico |
| | 18 | 0.62 | Rio Itata |
| **Paleotsunami** | 71 | 0.61 | Chaihuin |
| | 50 | 0.61 | South of Huentemo |

Table 9 (Continued): The average spacing of maximum wave heights from quantitative analysis.

| Dataset (if existing) | tide gauge | average spacing of maximum wave heights (m) | name |
|---|---|---|---|
| | 28 | 0.61 | Quidico |
| | 10 | 0.61 | Loanco |
| **Paleotsunami** | 48 | 0.60 | Chepu |
| | 9 | 0.59 | Los Pellines |
| | 81 | 0.57 | Northern Puerto Saavedra |
| **Both** | 29 | 0.57 | Tirua |
| | 86 | 0.56 | Cerro Oncol |
| | 76 | 0.56 | West of Lago Lleulleu |
| **Paleotsunami** | 72 | 0.56 | Pucatrihue |
| | 51 | 0.56 | North of Rahue |
| | 43 | 0.56 | North of Guabun (top of archipelago) |
| | 38 | 0.56 | Los Muermos |
| | 36 | 0.56 | North of Hueicolla |
| **Paleotsunami** | 68 | 0.55 | Tubul |
| | 17 | 0.55 | Rio Itata |
| | 5 | 0.55 | Matancilla Shores |
| | 97 | 0.54 | Abtao |
| | 52 | 0.54 | Rahue |
| | 7 | 0.54 | San Antonio |
| **Paleotsunami** | 33 | 0.53 | Nique Norter |
| | 25 | 0.53 | North of Quidico |
| | 94 | 0.52 | South of Guayusca |
| | 61 | 0.51 | West of Puraloco |
| | 54 | 0.51 | Paso Huencho |

Table 10: The average spacing of arrival times from quantitative analysis.

| Dataset | tide gauge | average arrival time spacing (mins) | name |
|---|---|---|---|
| | 99 | 16.62 | Campihuapi |
| | 54 | 7.55 | Paso Huencho |
| | 60 | 6.44 | Tirua |
| | 2 | 5.40 | Matancilla Shores |
| **Paleotsunami** | 6 | 5.25 | Constitucion |

Table 11: List of the 22 promising sites from qualitative analysis sorted largest to smallest by spacing.

| Tide gauge | lat | lon | name | analysis | average minimum spacing (m or min)[1] |
|---|---|---|---|---|---|
| **60** | -38.328062 | -73.537000 | Tirua* | Arrival Times | 6.44 |
| **55** | -35.109678 | -72.211204 | Los Rabanos | Wave Height | 1.27 |
| **6** | -35.315883 | -72.424995 | Constitucion* | Both | 0.88 m |
| **64** | -39.358523 | -73.231968 | Queule* | Wave Height | 0.81 |
| **85** | -39.180950 | -73.270188 | Nueva Tolten* | Wave Height | 0.73 |
| **34** | -39.515168 | -73.275059 | S of Maiquillahue | Wave Height | 0.71 |
| **83** | -39.081303 | -73.303089 | Chelle | Wave Height | 0.71 |
| **65** | -39.427001 | -73.246352 | Missisipi* | Wave Height | 0.7 |
| **66** | -42.634988 | -74.126936 | Lake Huelde/Cucao* | Wave Height | 0.69 |
| **31** | -38.785320 | -73.426751 | Puerto Saavedra* | Wave Height | 0.67 |
| **84** | -39.127511 | -73.286596 | Reduccion Porma | Wave Height | 0.65 |
| **27** | -37.898538 | -73.540263 | Playa Llancao | Wave Height | 0.62 |
| **28** | -38.011591 | -73.480821 | W of Guape | Wave Height | 0.61 |
| **71** | -39.943859 | -73.595580 | Chaihuin* | Wave Height | 0.61 |
| **48** | -42.060020 | -74.048317 | Chepu* | Wave Height | 0.6 |
| **29** | -38.229607 | -73.477270 | Quidico* | Wave Height | 0.57 |
| **81** | -38.717915 | -73.470454 | N Saavedra* | Wave Height | 0.57 |
| **76** | -38.084088 | -73.461696 | W of Lago Lleulleu | Wave Height | 0.56 |
| **72** | -40.535364 | -73.743268 | Pucatrihue* | Wave Height | 0.56 |
| **68** | -37.234248 | -73.427520 | Tubul* | Wave Height | 0.55 |
| **61** | -39.281829 | -73.240193 | W of Puraloco | Wave Height | 0.51 |
| **54** | -42.862732 | -74.196800 | Paso Huencho | Both | 0.51 m |

*The site is in the tsunami deposit database.
[1]Depending on analysis, the unit is either in meters or minutes.

Once I established my final 22 promising sites, 13 of them (59%) are tsunami deposit sites (two of which are also historical sites) and 9 are not (Table 11). These promising sites are highly susceptible to preserving deposits, which is likely due to their location and topography. The directionality of Tirua, Constitucion, Queule, Nueva

Tolten, Missisipi, Lake Huelde, Puerto Saavedra, Chepu, Quidico, and Pucatrihue are west-facing shores, yet are able to filter and magnify differences in tsunami effects. Chaihuin and Tubul are north-facing shores that are successful at distinguishing northern earthquakes from central and southern ones, as expected.

The 5 sites from arrival times that were spaced ≥5.0 minutes on average were Campihuapi, Paso Huencho, Tirua, Matancilla Shores, and Constitucion (Table 10). Paso Huencho is a promising site and Constitucion is a promising and tsunami deposit site. The locations and directionality of these sites make them capable of magnifying differences in arrival times. Campihuapi, a north-facing shoreline located in the south-central portion of the archipelago, is a unique site in that its mean spacing of all 9 arrival times was ~17 minutes. This is also one of the southernmost sites and located in the nearfield of the southern scenario, explaining why variation in arrival times are as low as 2 minutes and as high as 190 minutes. The mean spacing between arrival times at Paso Huencho, the southernmost site located on a straight stretch of coast, was ~8 minutes, with a range of 0.02 – 80 minutes. The range of arrival times at Paso Huencho can be explained by its proximity to the southern rupture. As expected, the north-facing Campihuapi got the tsunami wave sooner than Paso Huencho. As a general rule of thumb, tsunami waves from the north arrive at north facing coasts earlier than at coasts that are not north facing (and vice versa for southern waves arriving at south-facing shores).

At Tirua, the mean spacing between arrival times was ~6 minutes (Table 10), with an arrival time range of 6-65 minutes. Tirua is a northwest-facing shore, making Tirua a site that easily differentiates northern arrival times from central and southern scenarios.

The mean spacing between arrival times at both Matancilla and Constitucion was ~5 minutes. Both are northern locations within close proximity to the northern rupture, so differentiating northern arrival times is possible. Central scenario tsunami arrival times would be second to distinguish, because of the protection of the Arauco peninsula delaying the arrival of a central scenario tsunami.

## High-Resolution Inundation Maps

Eight inundation map areas built from high-resolution topography allow for detailed calculation of tsunami runups and inundation from my earthquake scenarios (Figure 13-16). Out of the previously discussed list of promising sites (Table 11), 4 of them have high-resolution inundation topography. These include Queule (both 1 and 2 versions), Quidico, Tirua, and Puerto Saavedra (both 1 and 2 versions; Figure 14-16). Most tsunamis flooded previously studied tsunami deposit locations, with the exception of the $M_w$ 8.6 central scenario at Queule 2 (Figure 14), Andalien (Figure 13), and Tirua (Figure 15). Paleotsunami site locations are also often in maximum flooding zones (see Figure 14-15).

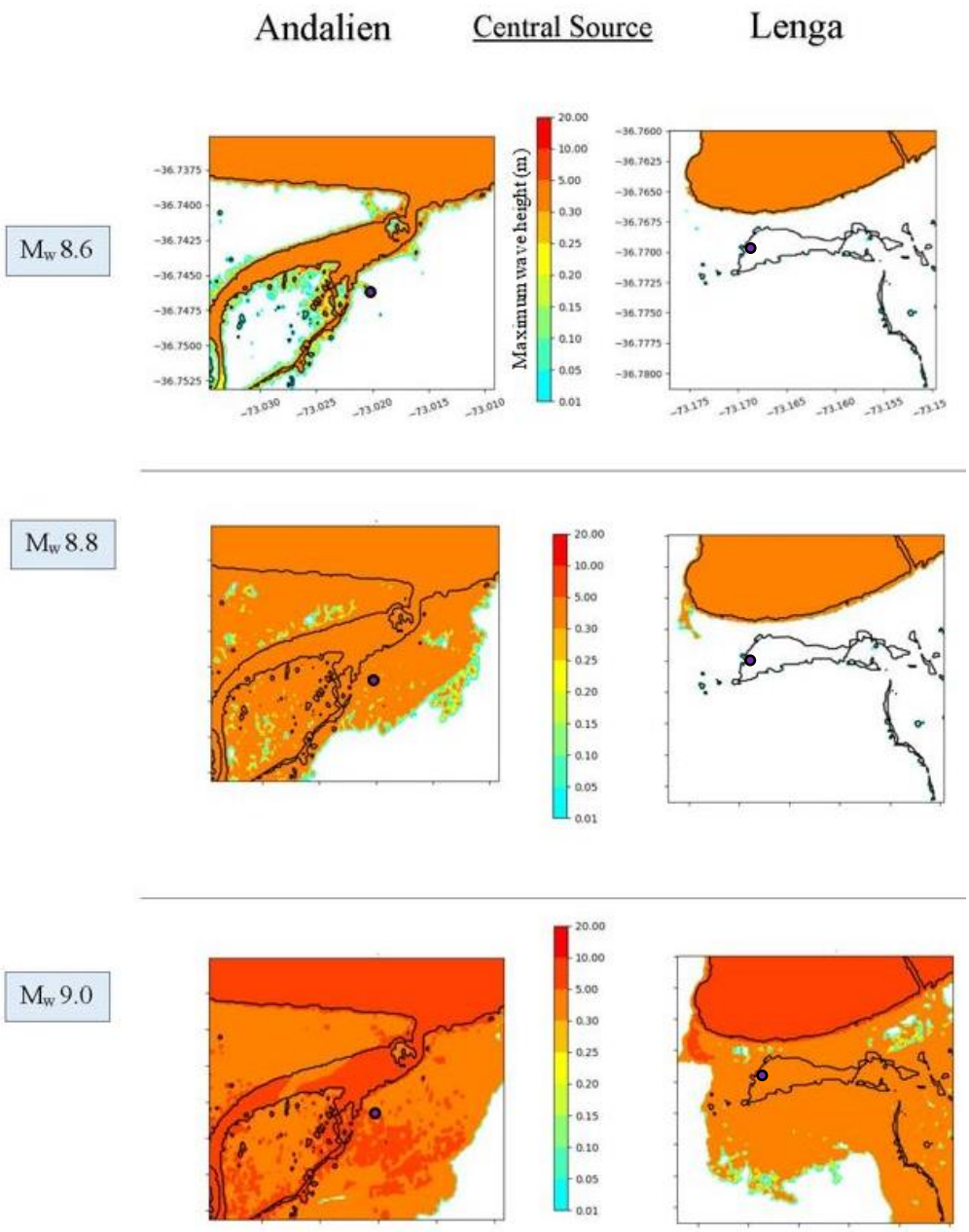


Figure 13: Tsunami inundation maps of Andalien and Lenga, Chile from central earthquakes on 0.40” topographic grids. The purple dots at the Andalien and Lenga sites mark the location of a tsunami deposit from L. Ely, pers. comm. (2017). The Lenga site has no record of a 2010 or 1960 tsunami, and my inundation map shows inundation from a $M_w$ 9.0 earthquake. In 1960 it is likely inundation occurred behind the beach berm, but left no sand deposits (L. Ely, pers. comm., 2018).

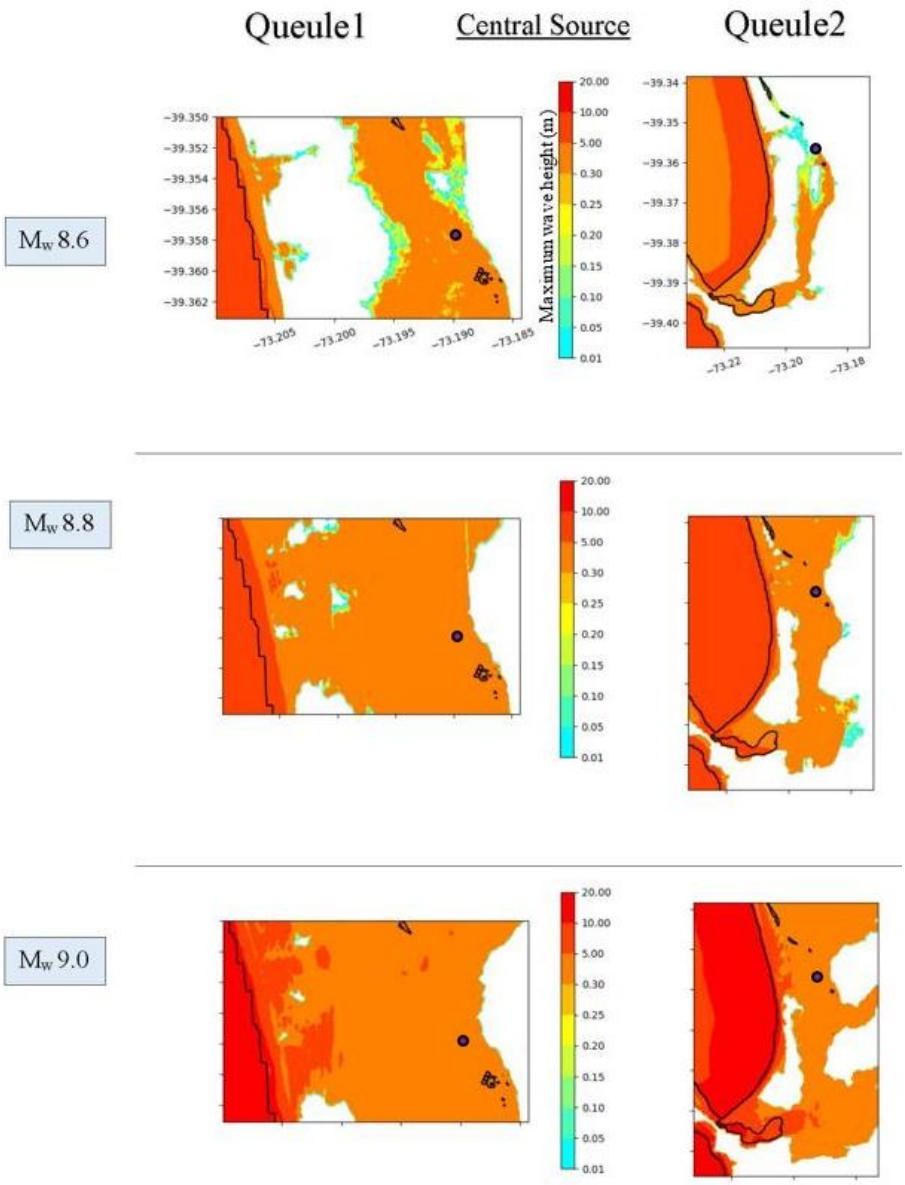


Figure 14: Inundation maps of Queule, Chile from central earthquakes. The purple dot marks the location of a 1960 tsunami deposit, L. Ely, pers. comm. (2017). The resolution on Queule 2 is 0.61” and Queule 1 is 0.28." The 1960 deposit was in many places throughout this site (L. Ely, pers. comm., 2018).

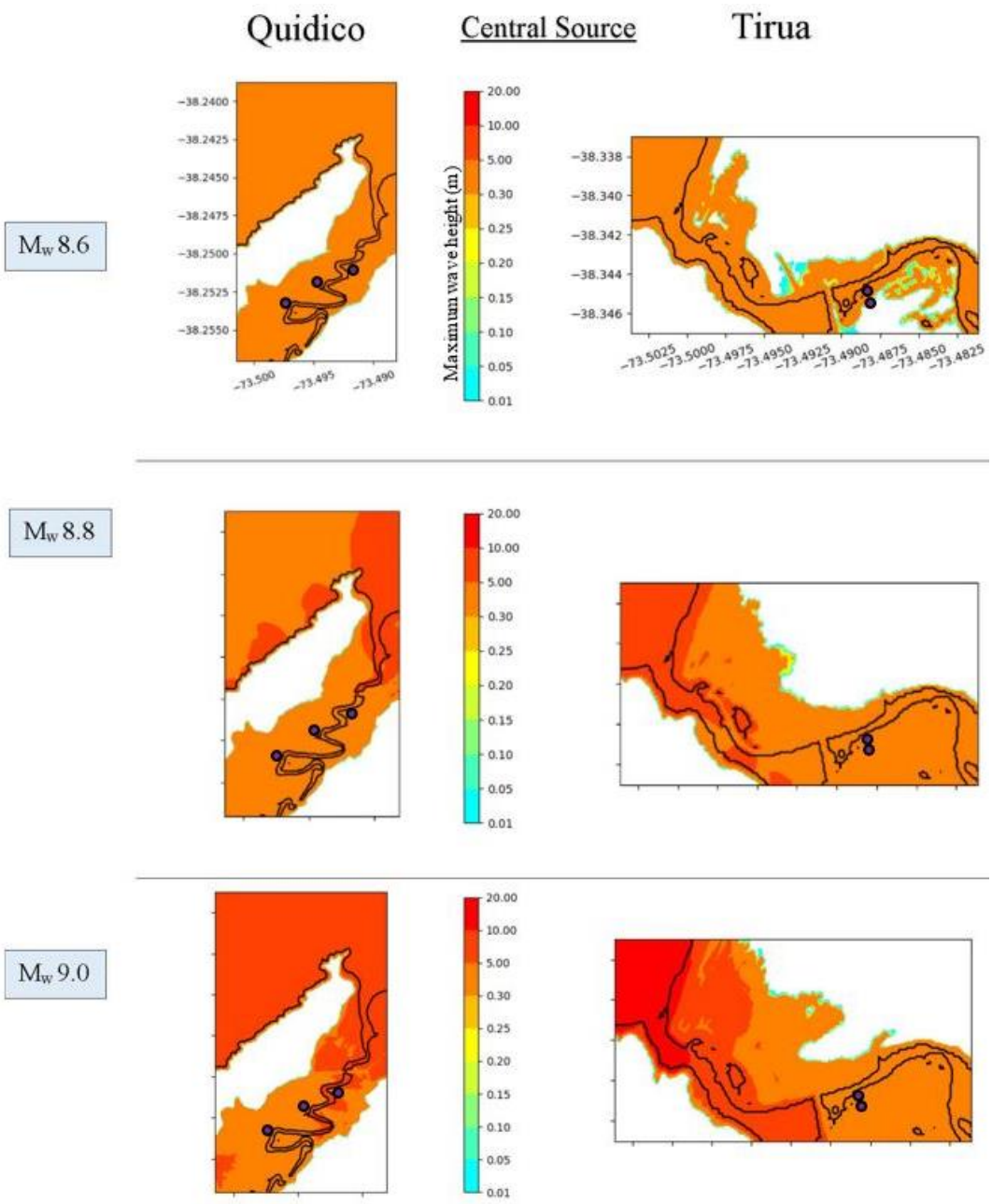


Figure 15: Inundation maps of Quidico (0.23" resolution) and Tirua (0.31" resolution), Chile from central earthquakes. The purple dots mark the locations of paleotsunami deposits and the 2010 tsunami deposit (Garrett et al., 2013; Ely et al., 2014; Nentwig et al., 2015; Hong et al., 2016; Cisternas et al., 2017; Dura et al., 2017).

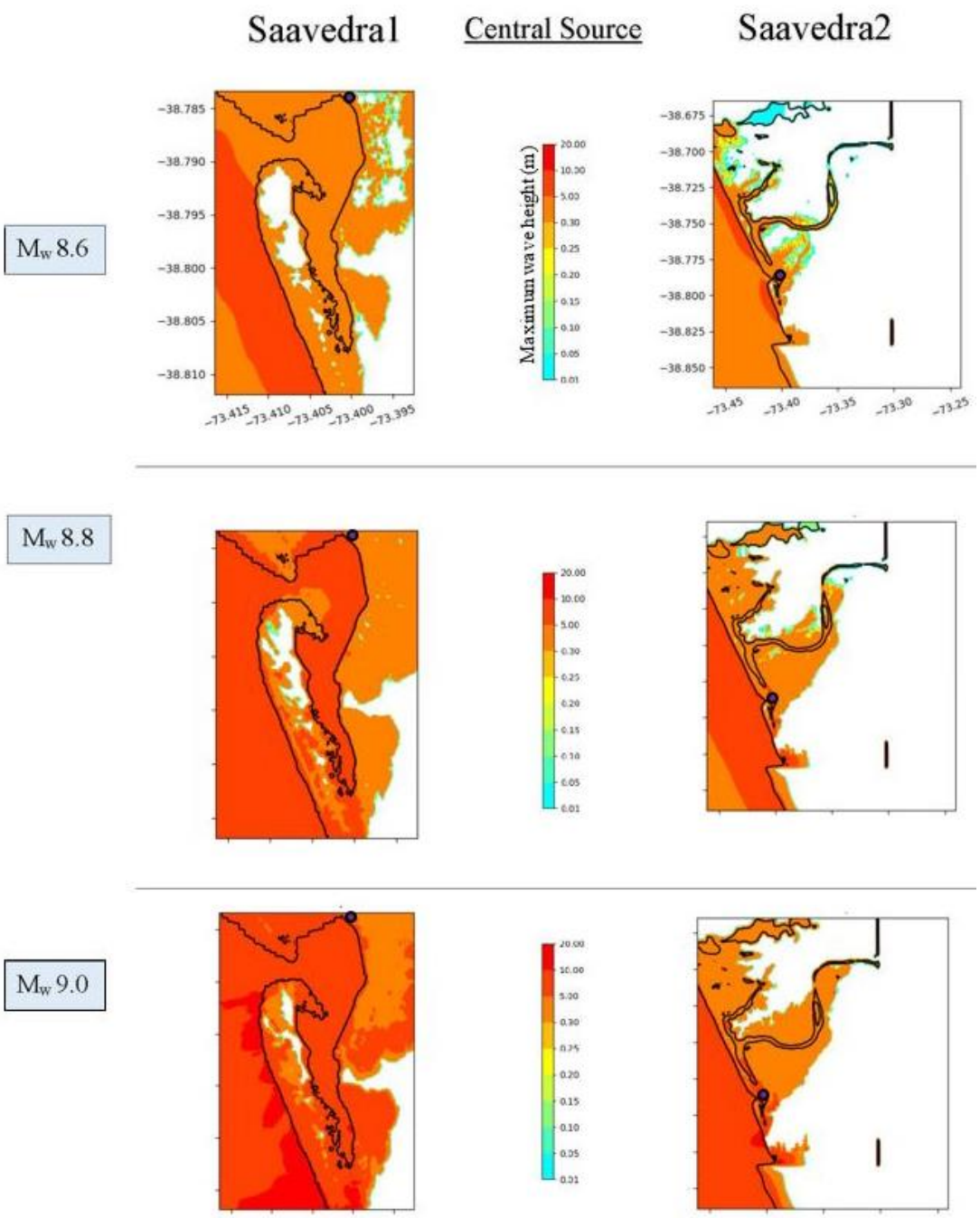


Figure 16: Inundation maps of Puerto Saavedra, Chile from central earthquakes. The purple dot marks the location of a paleotsunami deposit and the 1960 tsunami deposit from Wright and Mella (1963). The resolution on Saavedra 2 is 3.05” and Saavedra 1 is 0.40."

All inundation maps showed an increasing trend in tsunami wave heights and inundation extent with increasing earthquake magnitudes, as expected. For example, at Andalien (Figure 13), the inundation limit of the nearfield (central) earthquake was near the shoreline for the $M_w$ 8.6 scenario, 0.5 km inland for the $M_w$ 8.8 scenario, and an additional 0.2 km inland for the $M_w$ 9.0 scenario.

Although Andalien is a north-facing bay, the $M_w$ 8.8 scenario affected Andalien and not Lenga, a northwest-facing bay. The sensitivity of Andalien may be explained by the low-lying topography of the Andalien River that allows tsunami waves to propagate more inland than Lenga for the $M_w$ 8.8 scenario (Figure 13). Because the topography of Lenga is not low-lying (the shore has a 10-m berm), this explains why a scarce paleotsunami deposit record exists here.

At Queule (Figure 14), Quidico (Figure 15), Tirua (Figure 15), and Puerto Saavedra (Figure 16), the $M_w$ 8.6 scenarios inundates the Queule River, Quidico River, and Puerto Saavedra because they all have low-lying topography, which also explains why these locations are paleotsunami deposit sites.

## Comparing Tsunami Wave Heights with Published Data

All 99 simulated wave heights are comparable with published 2010 and 1960 wave heights since my maximum inundation data is in approximately the same location as the 2010 and 1960 observations. The published maximum wave heights for the 2010 Maule and 1960 Valdivia tsunami extends between 35.4°S and 40°S (Figure 17-18).

Simulated wave heights for the $M_w$ 8.8 northern scenario underestimated the published 2010 Maule wave heights at many locations, although some overlap exists at Concepcion (36.8°S), on the Arauco Peninsula (37.2°S), Quidico (38.2°S), and Puerto Saavedra (38.8° S). Sites with higher runup in 2010 (Figure 17), in particular Constitucion (35.4°S), Chevelle (35.9°S), Dichato (36.5°S), Tome (36.6°S), Concepcion (36.8°S), Locobe (37.3°S), and La Peuca (38.5°S), are underestimated in the range of 5-20 m.

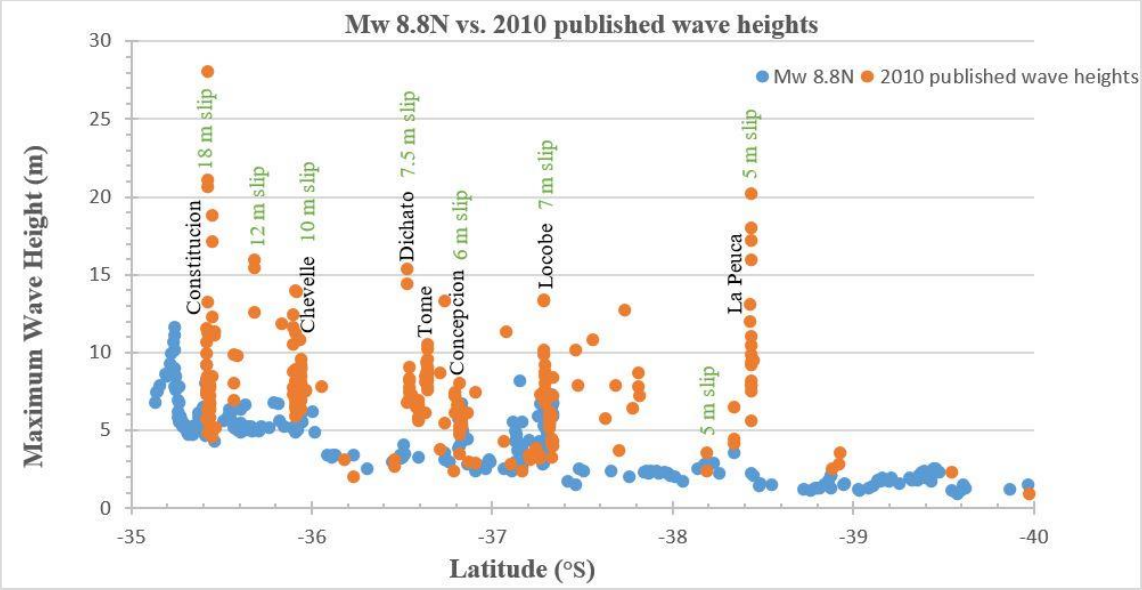


Figure 17: The published maximum wave heights for the 2010 Maule earthquake (NGDC/WDS, 2018a; orange dots) compared to the simulated maximum wave heights for a uniform slip $M_w$ 8.8 northern scenario (blue dots) shows the underestimation of simulated wave heights. The amount of slip on the subduction zone perpendicular to each tide gauge (green text) is from the published slip distribution of the 2010 Maule earthquake from Pollitz et al (2011). The $M_w$ 8.8 northern earthquake has a uniform 5 m slip everywhere from -35°S to -43°S.

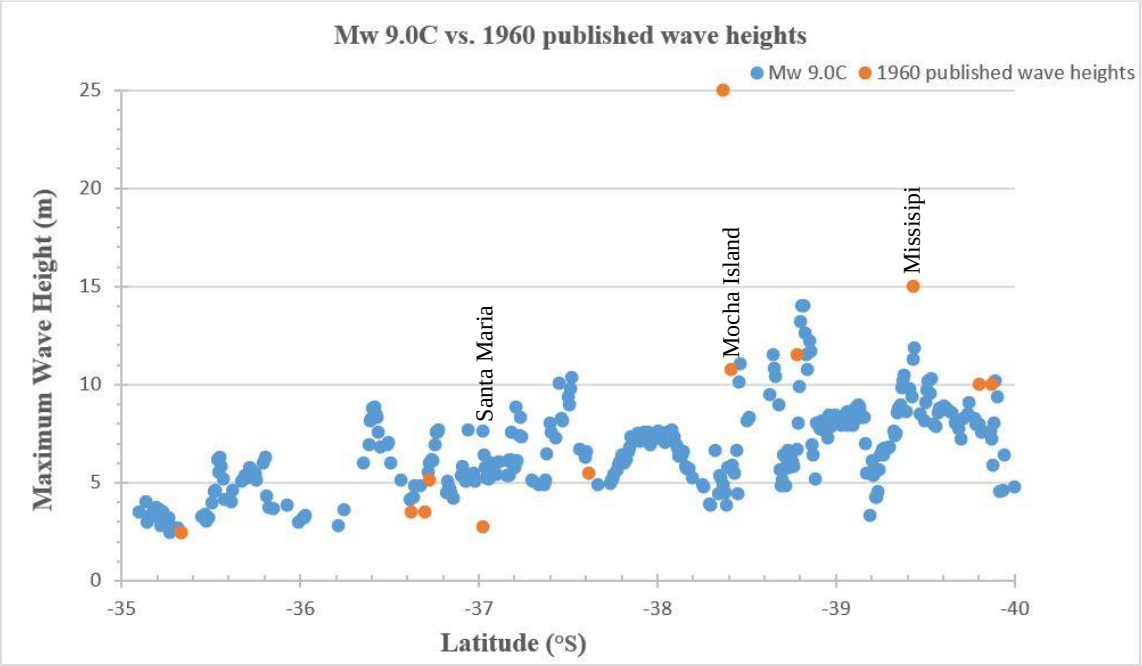


Figure 18: The published maximum wave heights for the 1960 Valdivia earthquake (NGDC/WDS, 2018a; orange dots) compared to the simulated maximum wave heights for a $M_w$ 9.0 central scenario (blue dots).

Agreement between the 1960 Valdivia tsunami observations and the $M_w$ 9.0 central scenario wave heights were relatively good (Figure 18). Data for 1960 is sparse; however, only at three sites did simulated wave heights deviate from observations (Figure 18): at Santa Maria (-37.02°S), the simulation was a few meters too high, 15 m too low at Mocha Island (-38.37°S), and a few meters too low at Missisipi (-39.43°S). I did not compare the 1960 Valdivia tsunami observations to the $M_w$ 9.0 southern scenario because my central rupture extended as far south as reported observations for the 1960 tsunami (NGDC/WDS, 2018a).

# CHAPTER VI

# DISCUSSION

## Outliers in Tsunami Wave Height and Arrival Time Distribution along the Coast

Notable outliers from my simulated wave heights along the coast are at Dichato, Santa Maria, West of Guape, Quidico, Cerro Oncol, and Guabun (Figure 11). At Dichato, tsunamis from all three northern ruptures were locally enhanced, as was the central $M_w$ 9.0 (and slightly the central $M_w$ 8.8); Dichato is in the nearfield for all of these scenarios as well. Dichato is a north-facing bay that is open to direct propagation from tsunamis generated by earthquakes with rupture to the north, whereas tsunamis propagating from central or southern earthquakes are obstructed by a peninsula on the west side of the bay.

Maximum wave heights in Santa Maria (an island 30-km west of the mainland coast of Chile) appear surprising in that the $M_w$ 9.0 northern scenario is smaller than the $M_w$ 9.0 central and $M_w$ 8.8 central scenarios. However, just to the south in Tubul and the Yani Dunes both the northern and central scenarios were highest (Figure 11). The gauge at Santa Maria is in the zone of earthquake overlap between the $M_w$ 9.0 central and northern rupture scenarios, thus is in the nearfield of both events, so I expected the wave heights to be similar (such is the case in Tubul). One explanation for the Santa Maria tide gauge is that it is on the western shore of Santa Maria Island, so wave heights from a northern scenario would dissipate once the tsunami hits the northern part of the Santa Maria shore and traveled to the western shore. However, the tide gauge on the western

shore of Santa Maria Island is in the direct path of tsunami waves from the central scenarios.

West of Guape wave heights for the $M_w$ 9.0 northern scenario were anomalously low while at nearby Quidico they were anomalously high compared to the background trend of the southward decreasing heights of this scenario (Figure 11). Both tide gauges at West of Guape and Quidico are in the nearfield of the central scenarios, so I expected both locations to be highest for the $M_w$ 9.0 central scenario. Wave heights for the $M_w$ 9.0 northern scenario at West of Guape were low because the tide gauge is protected from northern waves by the Arauco Peninsula (Figure 19). At Quidico, wave heights for the $M_w$ 9.0 northern scenario were so high because (1) the gauge is not protected by the Arauco Peninsula to the north, (2) the site is north-facing, and (3) Quidico sticks out to the west relative to its northern shores (Figure 19).

At Cerro Oncol, which is in the nearfield of the central segment, the $M_w$ 9.0 southern scenario produces 1-m higher wave heights than the $M_w$ 9.0 central scenario (Figure 11). The peninsula north of Cerro Oncol, Pillin, might be obstructing tsunami waves from the central nearfield, but does not obstruct a southern tsunami. Guabun, located in the southern nearfield, is similar in that the $M_w$ 9.0 central scenario produces >1m-higher wave heights than the $M_w$ 9.0 southern scenario (Figure 11). The top of the archipelago acts as a barrier for tsunamis waves from the south, but is easily accessible for waves coming from the $M_w$ 9.0 central scenario.

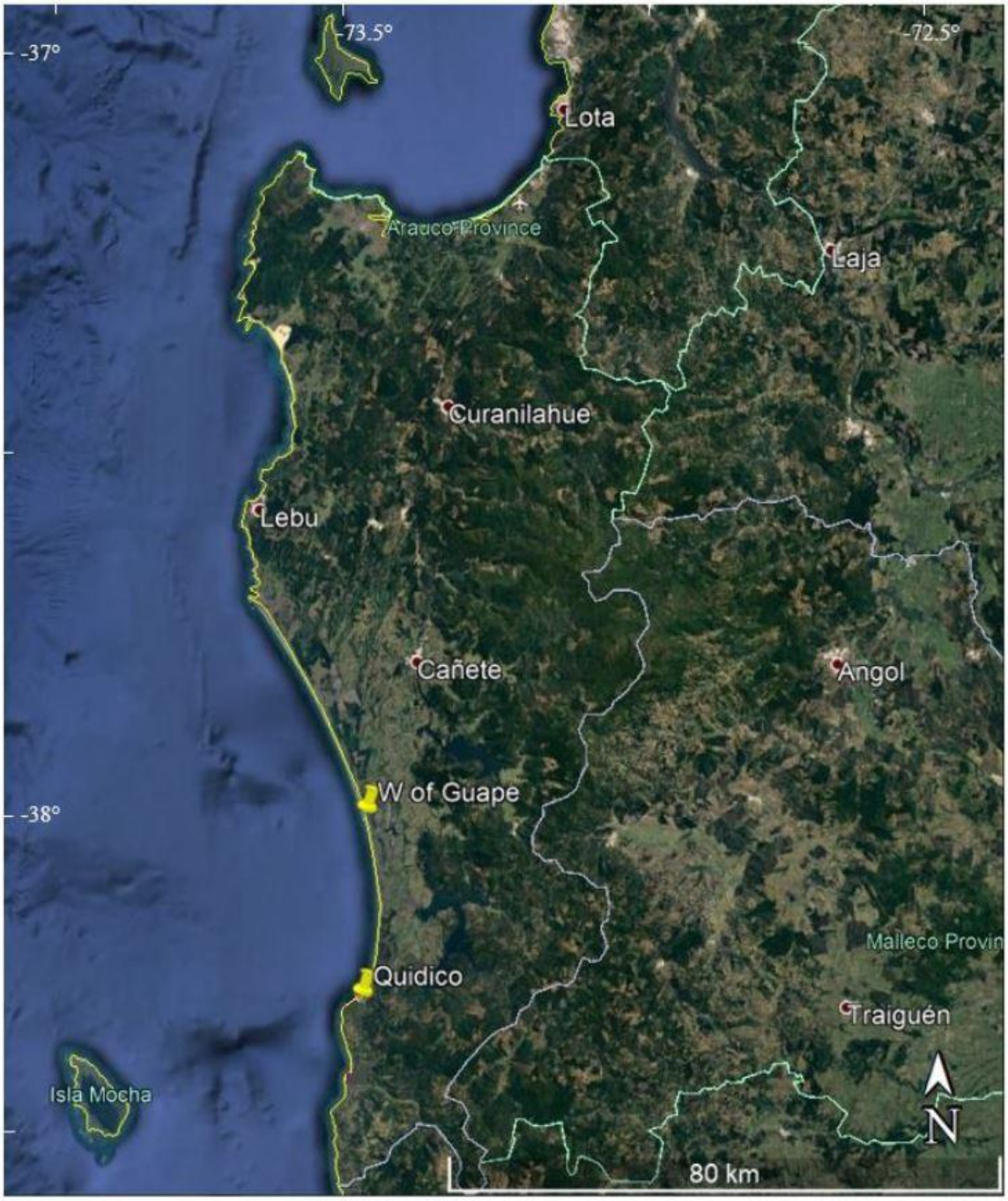


Figure 19: Quidico sticks out to the west relative to its northern shores, whereas West of Guape is protected from a northern scenario by the Arauco Peninsula. Google Earth Image.

There are few outliers in arrival times because many tsunami arrival times could not be determined (due to bathymetric resolution error) and were removed; only the remaining data points appear in Figure 12. However, one outlier from the variation in arrival times along the coast is at Cerro La Gloria (Figure 12), in the northern and central nearfield. Tsunami arrival times at Cerro La Gloria are later for the central scenario than the northern scenario. One possible explanation is the shoreline directly south of Cerro La Gloria contains three south-facing bays and the Yani Dunes at Locobe that might delay a tsunami wave from a southern direction (i.e., from a central scenario; Figure 20).

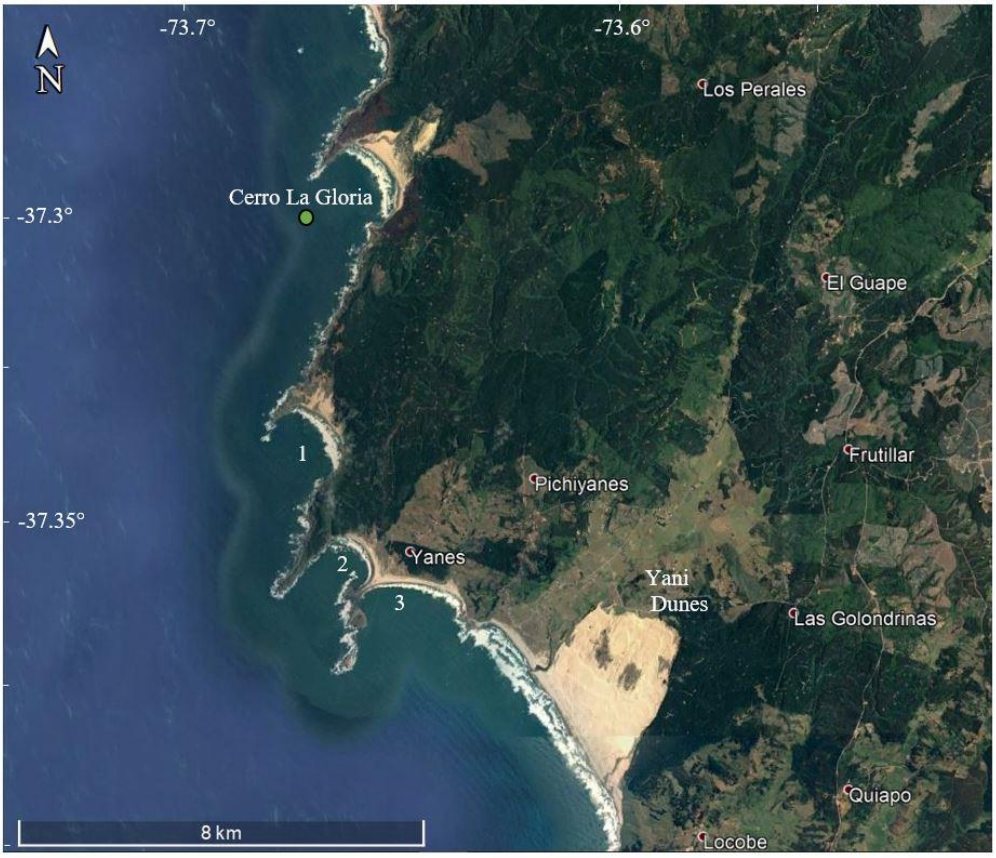


Figure 20: The shoreline directly south of Cerro La Gloria (green dot is the tide gauge) contains three south-facing bays (numbered) and the Yani Dunes that could delay a central tsunami wave at Cerro La Gloria. Google Earth Image.

### Comparing the 2010 and 1960 Recent Events with Simulated Scenarios

Comparing recent events with my tsunami simulations is an important validation tool for assessing how close my hypothetical scenarios are to real-world situations. Although the rupture area and magnitude of the combined $M_w$ 9.0 southern and central scenarios are only a $M_w$ 9.0, their land level change data showed a close match to the $M_w$ 9.5 1960 Valdivia earthquake. Observations for the 1960 Valdivia tsunami wave heights and the $M_w$ 9.0 central scenario agree with each other well, except at the following three sites (Figure 18): Santa Maria (-37.02°S), Mocha Island (-38.37°S), and Missisipi (-39.43°). However, the Mocha Island and Santa Maria sites should not be considered in the comparison, because these observations were not made at exactly the same longitude as my maximum inundation data. For example, there are two different wave height observations at -38.37°S, 25 m-high waves on Mocha Island and 11-m waves on mainland Chile near Tirua (Figure 18). Although both locations share the same latitude as my maximum inundation data, my wave heights were calculated on mainland Chile near Tirua, not on Mocha Island. Similarly, the Santa Maria wave height (-37.02°S) was observed on the island, but my simulation measured on the mainland. Therefore, these sites can be disregarded. My simulated wave height at Missisipi is 3 m too low and is in the same location as the observed wave heights, so this site can be noted as an outlier. It is possible the 1960 tsunami at Missisipi produced greater wave heights than my $M_w$ 9.0 central scenario, being generated by a larger earthquake at a coastal river inlet where wave amplification could factor in.

The rupture area and magnitude of the $M_w$ 8.8 northern scenario is similar to the $M_w$ 8.8 2010 Maule earthquake, and coastal land-level change between observations of 2010 Maule and the seafloor deformation for my scenario showed less than 20% difference. Comparing the 2010 Maule tsunami wave heights with my simulations of a $M_w$ 8.8 northern scenario shows similar values at Concepcion (36.8°S), on the Arauco Peninsula (37.2°S), Quidico (38.2°S), and Puerto Saavedra (38.8°S; Figure 17). However, at Constitucion (35.4°S), Chevelle (35.9°S), Dichato (36.5°S), Tome (36.6°S), Concepcion (36.8°S), Locobe (37.3°S), and La Peuca (38.5°S), simulated wave heights are much smaller than published observations (compare maximum 9-m simulated wave heights vs. 28 m observed at Constitucion; Figure 17). As a first-order interpretation, the low-resolution bathymetry does not resolve bathymetric features at a smaller scale than 30 arcseconds that affect shoaling of a tsunami (Tang et al., 2009; Pan et al., 2010). Resolutions ~100 times finer (1/3 arcsecond) are recommended for onshore modeling of runup and inundation (Tang et al., 2009). However, this interpretation cannot be verified without better bathymetric data at the sites in question.

Shelf resonance (the entrapment and amplification of wave energy over the wide continental shelf and slope; Yamazaki and Cheung, 2011) and resulting edge waves (the refraction of waves into multiple directions when tsunami waves amplify in relatively shallower water; Yamazaki and Cheung, 2011) are thought to have been created at Constitucion and the bay of Concepcion for the 2010 Maule tsunami resulting in an amplification of wave heights (Figure 17; Yamazaki and Cheung, 2011) and these

particular locations having the highest maximum wave heights. If edge waves were not created, especially if the low-resolution of the bathymetry does not allow resonance to occur, GeoClaw would underestimate the amplified wave heights.

A final effect of the low-resolution bathymetry in comparing the 2010 Maule tsunami to the $M_w$ 8.8 northern scenario is problems capturing runup effects around embayments and peninsulas (i.e., the Dichato embayment, the Tome embayment, the Corral embayment, the Arauco Peninsula, the Concepcion peninsula, and the southern Valdivia Province peninsula), which make up most of the points on the coast with low and high runup in the same region (Figure 17). The role of bay and shelf resonance during tsunami propagation has been investigated at different locations for several events (Bellotti et al., 2012; Yamazaki and Cheung, 2011; Roeber et al., 2010; Horrillo et al., 2008). Propagating tsunamis tend to excite and amplify natural frequencies of bays, leading to higher runup in these coastal areas (Bellotti et al., 2012).

In addition to bathymetry contributing to differences between tsunami observations and the simulation (Figure 17), the 2010 Maule earthquake ruptured with a complex slip distribution of slip over 110 seconds (Delouis et al., 2010), while the $M_w$ 8.8 northern scenario ruptured with uniform slip instantaneously. The location of maximum 28 m wave heights at Constitucion was trench-perpendicular to the estimated location of maximum slip (18 m; Pollitz et al., 2011). Locations farther south, Chevelle, Dichato, Tome, Concepcion, etc., with significantly higher wave heights than the $M_w$ 8.8 scenario displayed trench-perpendicular slip values that roughly corresponded to runup.

For example, slip was 10 m at Chevelle (with a maximum wave height of 14 m), 7.5 m at Dichato (with a maximum wave height of 15 m), 6 m at Concepcion (with a maximum wave height of 7 m), and 7 m at Locobe (with a maximum wave height of 13 m; Pollitz et al., 2011). In comparison, the $M_w$ 8.8 northern scenario slip was 5 m, extending to -43°S, roughly the average wave height value for that section of the coast (Figure 17).

By making a comparison between wave heights from simulated scenarios and the 2010 wave heights, there is a similar trend between both, where outliers are explained by either the low resolution bathymetry used or the complex slip distribution of the 2010 Maule tsunami. Figure 17 is a great visual indicator of how close my hypothetical scenarios are to real-world events. Although most of the outliers in the 2010 published wave heights can be explained by slip distribution, there is an overall trend in the $M_w$ 8.8 northern scenario that shows wave height values decreasing to the south where the highest waves are located in the areas with the largest slip (Figure 17). My scenarios coincide with the general trend of tsunami effects (i.e., runup), therefore tsunami models are a useful and powerful tool for matching paleotsunami deposits and historical accounts of past earthquakes to source magnitudes and locations of paleoearthquakes in Chile.

## Northern and Central Sites Are More Sensitive to the Earthquake Source Location/Magnitude than Southern Sites

To infer pre-instrumental earthquake properties, further investigation from simulated wave height spacing from the 99 tide gauges (33 in each region) is necessary to

understand which sites are more sensitive to source location or the magnitude of the earthquake. In the northern region, there are 25 of 33 sites (76% of all sites in the north) with spacing ≥0.5 m between all simulations, and 22 of 33 sites (67%) in the central region with spacing ≥0.5 m. However, there are only 12 of 33 sites (36%) with spacing ≥0.5 m (Figure 21) in the southern modeling region. The northern and central regions therefore have better filtering capabilities between tsunamis from earthquakes of differing magnitudes and from different source locations than those of the southern region.

Looking at only $M_w$ 8.8 and $M_w$ 9.0 earthquakes (data suggests the $M_w$ 8.6 typically are too small to leave extensive deposits) 72 of the 99 gauges (73%) have an average spacing of ≥0.5 m between northern, central, and southern earthquakes, showing a sensitivity to earthquake location, regardless of magnitude (Figure 22). The northern section had 27 of 33 (82%) sensitive sites, the central section had 28 of 33 (85%) sensitive sites, and the southern section had 17 of 33 (52%) sensitive sites. One possible explanation for the southern section having less promising sites than the central or northern sections is that the bathymetry off the southern continental slope might be different from that of the northern and central continental slopes, which can heavily influence tsunami wave interaction.

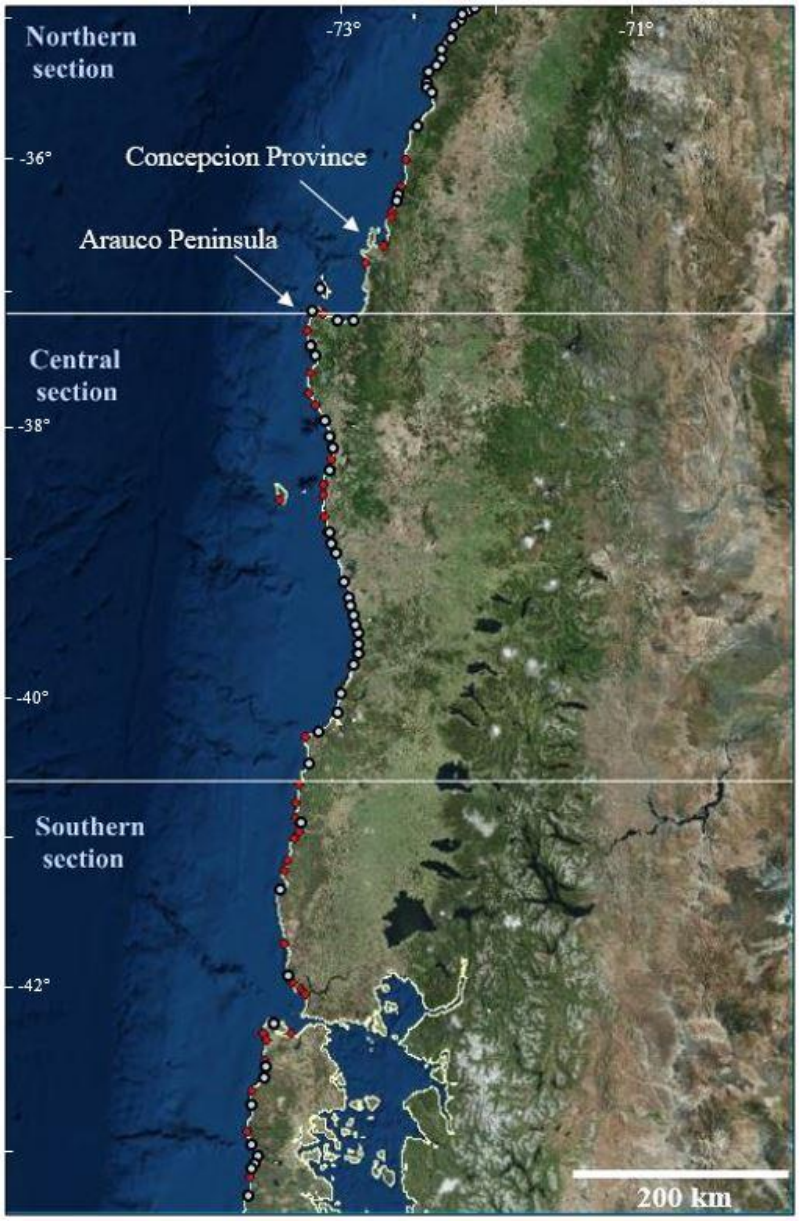


Figure 21: Locations of tide gauges that are determined to be sensitive to earthquake magnitude (grey dots; red dots are non-promising sites). The northern section had 25 sensitive sites, the central section had 22 sensitive sites, and the southern section had 12 sensitive sites, making a total of 59 sites. I did not include sites from arrival time data because they overlapped with the statistically promising sites from wave height data. These 59 grey dots also make up my statistically (but not final) promising sites.

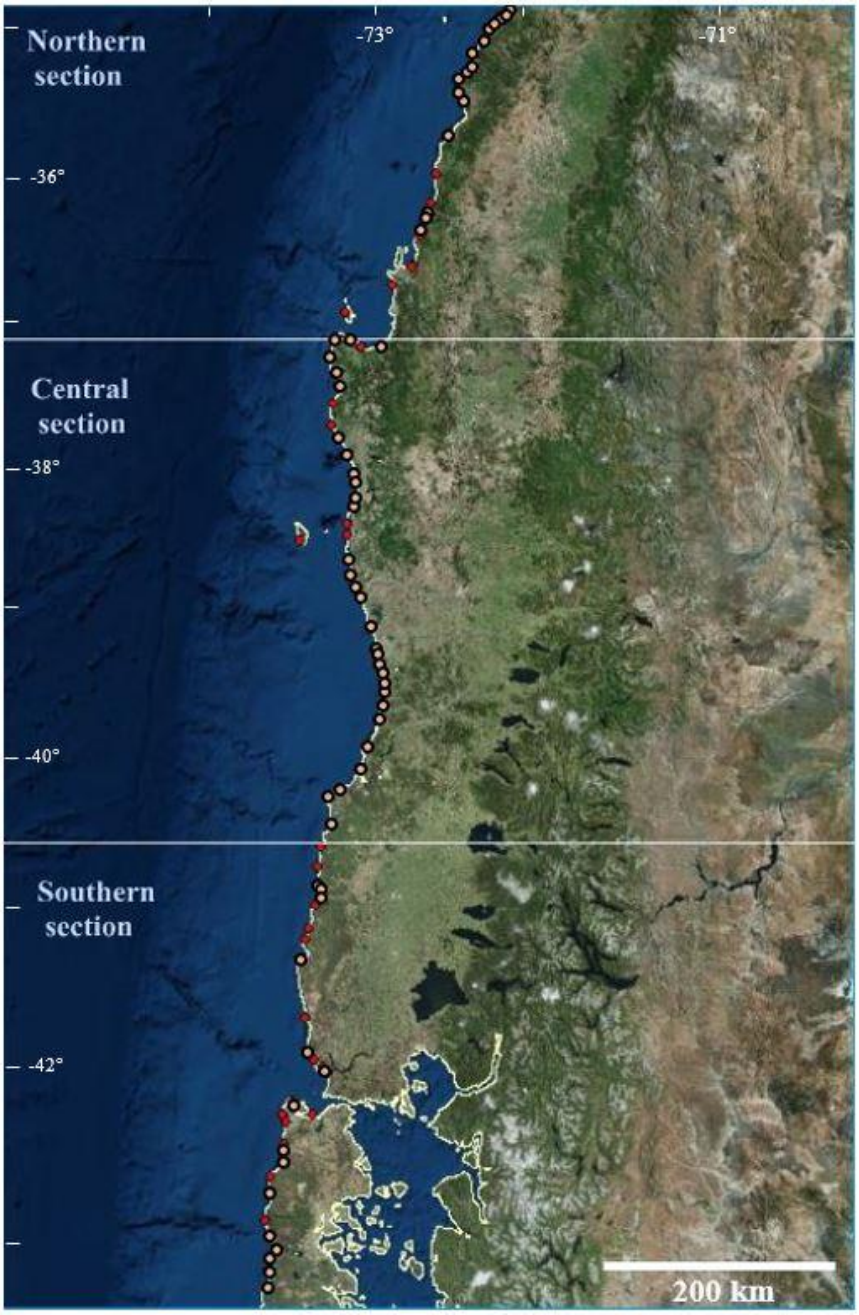


Figure 22: Locations of tide gauges that are determined to be sensitive to earthquake location, regardless of magnitude (orange dots; red dots are non-promising sites). For this analysis average minimum spacing for only $M_w$ 8.8 and $M_w$ 9.0 scenarios were used. The northern section had 27 sensitive sites, the central section had 28 sensitive sites, and the southern section had 17 sites, making a total of 72 sites.

The bathymetry of the continental slope is likely the reason the northern and central sections are more sensitive to earthquake magnitude and source location than the southern section. In general, the interaction of tsunami waves with bathymetric irregularities (i.e., aseismic ridges and seamounts) on the continental slope results in increased amplitudes and reduced wavelengths as the wave shoals (Horsburgh et al., 2008). The southern continental shelf is wider, has more ridges (Kelleher and McCann, 1976) and is prone to more wave resonance phenomena due to the refractive effects of the bathymetry (Bellotti et al., 2012). Wave reflection and energy dissipation is the energetic result from wave interference due to slope irregularities (i.e., the Chile Ridge at -40°S; Figure 23) and the trapping of long waves such as tsunamis in the south (Horsburgh et al., 2008; Bellotti et al., 2012), leading to smaller and therefore more similar wave heights between scenarios.

Maximum wave heights from all my scenarios reached 6-7 m in the south and ~7-10 m in the north (Figure 11). This wave height difference could be explained by bathymetric irregularities from the continental slope. Since bathymetric irregularities control the dissipation of tsunami waves (Horsburgh et al., 2008; Bellotti et al., 2012), I inspected the locations of Chilean continental slope irregularities in ArcGIS. Smooth continental slopes, defined as having smooth seafloor morphology, are generally concentrated in the northern region (-35° to -39°S; Figure 23) and rough slopes are concentrated in the south-central region (-39° to -42°S; Figure 23). At -42°S, the slope is smooth, but the two peaks pointed out in Figure 23 are high enough in the profile to trap

long waves. In comparison, there are fewer promising sites between -39° and -42°S than -35° to -39°S. Notice the flat continental slope at 43°S (Figure 23), which correlates with a cluster of 5 promising sites in the south (Figure 23).

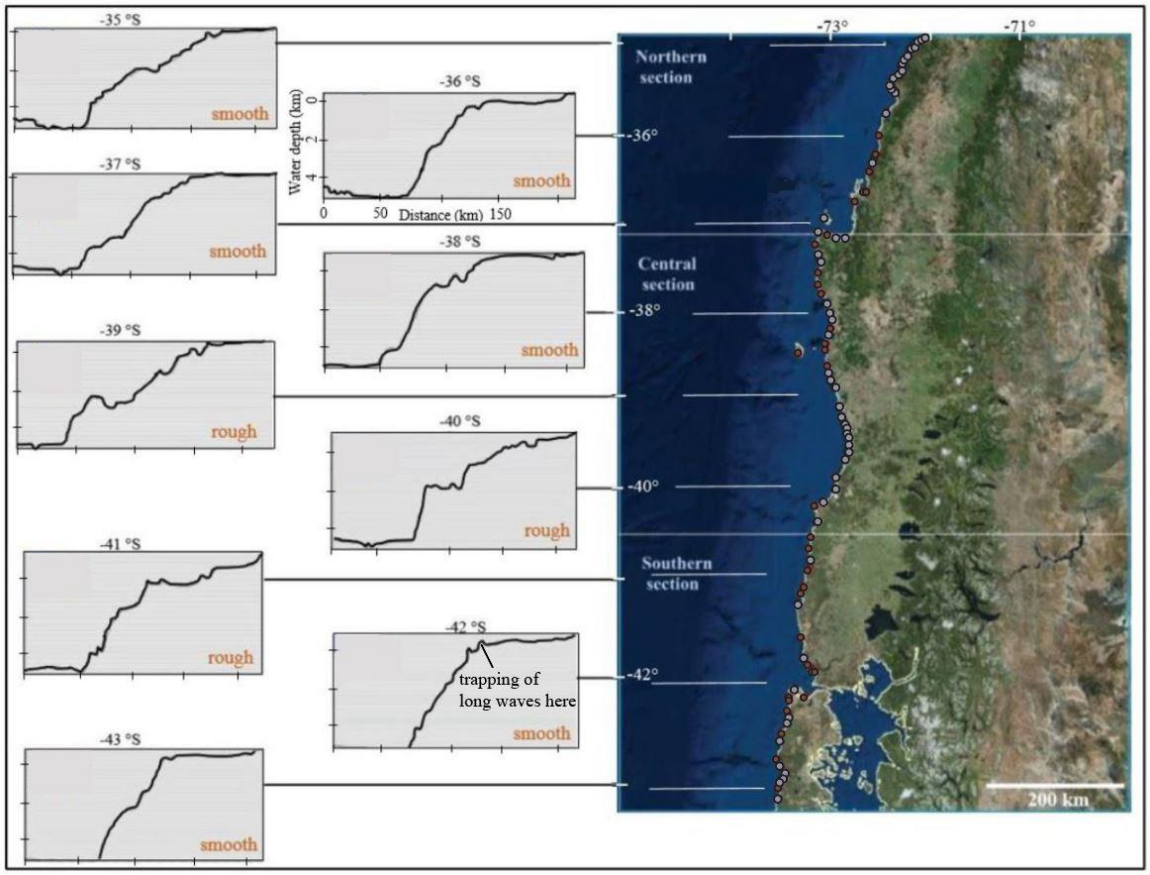


Figure 23: Profiles of the Chilean continental slope constructed from ArcGIS. "Smooth" and "rough" slope designations are based on the profile shape and its morphology visible in Google Earth. White lines are the length of the profile. Widths were measured in ArcGIS using the online basemap. The grey dots are my 59 statistically promising sites, and the red dots are non-promising sites. At -42°S, the slope is gentle, but the two peaks are high enough in the profile to trap long waves.

## Will My Method Work to Distinguish Paleoearthquake Properties from Paleotsunami Deposits?

Assessing maximum wave heights from my nine simulations at tsunami deposit and historical site locations is important for preliminary interpretations of distinguishing paleotsunami rupture location and magnitudes. At each site along the coast in the database, I can use the data presented in Figure 11 to calculate which of my nine simulated tsunamis could leave a deposit at paleotsunami locations, because the elevation of the backshore and coastal plain is obtainable in Google Earth. Many of the nine scenarios would be expected to leave a deposit at most of the paleotsunami deposit sites in the database; at 23 of 25 sites in the tsunami deposit database the backshore and coastal plain was at lower elevation than maximum tsunami waves from one or more simulations (Table 12). Two sites (Angol and Ancud) could not have tsunami deposits from any of my simulations because the maximum tsunami waves were not high enough to overtop the backshore and inundate the coastal plain.

Table 12: Location-specific potential for leaving tsunami deposits (highlighted orange) for each of the nine scenarios. Underlined places mark sites where high-resolution inundation maps were used for analysis rather than Google Earth.

| | Name | known record | absence of evidence* | lat (°S) | $M_w$ 8.6 N | $M_w$ 8.6 C | $M_w$ 8.6 S | $M_w$ 8.8 N | $M_w$ 8.8 C | $M_w$ 8.8 S | $M_w$ 9.0 N | $M_w$ 9.0 C | $M_w$ 9.0 S |
|---|---|---|---|---|---|---|---|---|---|---|---|---|---|
| **Northern section** | La Trinchera | 1960 | | -35.102 | | x | x | | | x | | | x |
| | Constitu-cion | 1960 | | -35.316 | | x | x | | x | x | | | x |
| | Coliumo | 1835, 2010 | | -36.504 | x | x | x | | | x | | | x |
| | Dichato | 2010 | | -36.538 | x | x | x | | x | x | | | x |
| | Penco | 1575, 1835, 1960, 2010 | 1737, 1837 | -36.727 | x | x | x | | x | x | | | x |
| | Andalien | 2010 | | -36.735 | | x | x | | | x | | | x |
| | Concepci-on/Talca-huano | 1960, 2010 | | -36.846 | x | x | x | x | x | x | | | x |
| | Santa Maria | 1835 | | -37.017 | x | x | x | x | x | x | x | | x |
| | Llico | 2010 | | -37.194 | x | x | x | x | x | x | | | x |
| | Tubul | 2010 | | -37.234 | x | x | x | | | x | | | x |
| **Central section** | Quidico | 1835, 1960, 2010 | 1575, 1737, 1837 | -38.230 | x | | x | | | x | | | x |
| | Tirua | 1575, 1960, 2010 | 1835, 1737 | -38.328 | x | | x | x | | x | | | x |
| | Mocha Island | 2010 | 1835 | -38.433 | x | | x | x | | x | | | x |
| | Puerto Saavedra | 1575, 1960 | | -38.785 | x | | x | x | | x | | | |
| | Queule | ????, 1960 | | -39.359 | x | | x | x | | x | x | | x |
| | Missisipi | 1960 | | -39.427 | x | | x | x | | x | x | | |
| | Valdivia | 1575, 1837, 1960 | 1835, 2010 | -39.826 | x | | x | x | | x | x | | |
| | Chaihuin | 1960 | | -39.944 | x | x | x | x | x | x | x | | x |
| **Southern** | Pucatrihue | 1960 | | -40.535 | x | x | x | x | | x | x | | |
| | Maullin | 1575, 1837, 1960 | 1835, 2010 | -41.618 | x | x | x | x | x | x | x | x | |
| | | | | | | | | | | | | | |

Table 12 (Continued): Location-specific potential for leaving tsunami deposits (highlighted orange) for each of the nine scenarios. Underlined places mark sites where high-resolution inundation maps were used for analysis rather than Google Earth.

| | Name | known record | absence of evidence* | lat (°S) | $M_w$ 8.6 N | $M_w$ 8.6 C | $M_w$ 8.6 S | $M_w$ 8.8 N | $M_w$ 8.8 C | $M_w$ 8.8 S | $M_w$ 9.0 N | $M_w$ 9.0 C | $M_w$ 9.0 S |
|---|---|---|---|---|---|---|---|---|---|---|---|---|---|
| | Ancud | 1837, 1960 | | -41.857 | x | x | x | x | x | x | x | x | x |
| | Chucalen | 1575, 1960, 2010 | | -41.863 | x | x | x | x | x | x | x | x | |
| | Cocotue | 1575, 1837, 1960 | | -41.905 | x | x | x | x | x | x | x | | |
| | Lake Huelde | 1575, 1837, 1960 | 1835, 2010 | -42.635 | x | x | | x | x | | x | | |

*for historical sites: records of an earthquake but no tsunami dated; for deposit sites: well-studied sites with no dates from earthquake

???? There is a deposit here (undated) older than 1960.

Interpreting paleoearthquake rupture locations and magnitudes from tsunami deposits can help refine today's knowledge of rupture extent from past events. Looking at sites in the database of tsunami deposits and historical accounts, specific rupture location and magnitudes can be calculated based on where tsunamis for the 1575, 1737, 1835, 1837, 1960, and 2010 earthquakes were and were not recorded (Table 12). For example, we know the rupture area solution for the 1960 earthquake was the combined area of $M_w$ 9.0 central and southern scenarios, with the total slip amount underestimated (see end of my Results section). If we analyze the combined simulations of all scenarios (Table 12), we could come to the same solution: central $M_w$ 9.0 scenarios show deposition possible between La Trinchera and Pucatrihue and southern $M_w$ 9.0 scenarios show 1960 deposition between Pucatrihue and Lake Huelde. However, at sites inundated by the 2010 tsunami, simulations do not compare well with 2010 observations, because inundation from a northern $M_w$ 9.0 matches better than the known solution of a northern $M_w$ 8.8

scenario. See section “Comparing the 2010 and 1960 recent events with simulated scenarios” for discussion of why the $M_w$ 8.8 scenarios have a poor match with the observations.

Simulations strongly suggest a tsunami from a $M_w$ 9.0 earthquake in the southern region is relatively consistent with the 1575 tsunami observations. However, Quidico, a north facing shore in the northern nearfield, does not have the 1575 tsunami deposit, but Penco, farther north, does have a record of a tsunami. This implies possibly that the 1575 northern rupture boundary extends farther north than the $M_w$ 9.0 southern scenario in order for tsunami waves to inundate at Penco but presumably not at Quidico. However, Penco (in Concepcion Bay) is a site where my simulation consistently underestimates wave heights (see 1835 example below), so moving the boundary might not be necessary.

For the 1737 earthquake, which lacked a tsunami, simulations suggest that the earthquake was smaller than a $M_w$ 8.6 if a central, smaller than a $M_w$ 8.8 if a northern, or as big as a $M_w$ 9.0 if a southern earthquake. Otherwise, a deposit or historical observation would likely have been noted in Penco, Quidico, or Tirua.

At 2 of the 3 sites inundated by the 1835 tsunami, the northern $M_w$ 8.8 scenario could leave deposits, while at the same time would not inundate sites with an absence of evidence of that event (Table 12). The site not inundated by the northern $M_w$ 8.8 scenario is Concepcion Bay. However, both the 2010 and 1835 tsunamis were observed to be 13-m high in Concepcion Bay (Lomnitz, 1970; NGDC/WDS, 2018a). As discussed earlier, bathymetric resolution issues underestimate inundation and wave heights at embayments.

If we predict the reasons the northern $M_w$ 8.8 scenario was not large enough in Concepcion Bay to recreate the 2010 observations are the same for the 1835 case, then a solution of a northern $M_w$ 8.8 scenario for the 1835 event is likely robust.

The best solution for the 1837 event is a $M_w$ 9.0 earthquake lying between the central and southern rupture areas. There are 4 well-studied sites inundated by the 1837 tsunami: Valdivia, Maullin, Cocotue, and Lake Huelde, and 2 sites with suspected evidence of no inundation (Table 12). Both central and southern $M_w$ 9.0 scenarios are possible, but neither are ideal because Lake Huelde is in favor of a southern scenario while Valdivia is in favor of a central scenario (Table 12). Therefore, the northern boundary of this earthquake is likely in between my central and southern regions. Future modeling of new scenarios can test this hypothesis.

The estimated magnitudes for past earthquakes are as follows: ~$M_w$ 8.0-8.5 for the 1575 earthquake, ~$M_s$ 8-8.5 for the 1835 earthquake, and $M_w$ 8.0 for the 1837 earthquake (Lomnitz, 2004; Cisternas et al., 2005). Overall, my work suggests that these magnitudes need to be revised (if uniform slip is assumed), and not only the source rupture extent.

## Sources of Error

Sources of error associated with modeling on low-resolution bathymetry and topography have previously been discussed in this thesis; however, additional sources of error associated with the earthquake source scenario also exist. Slip on my subfault

planes translated to the tsunami waveform requires many assumptions. In my method, slip produced seafloor deformation using the Okada (1985) formulation, which was directly translated to the initial tsunami input. Uniform displacement over a finite rectangular subfault leads to a deformed surface when inserted in a homogeneous elastic half space (Mandli et al., 2016). However, this is only an approximation since the actual seafloor in rarely flat, and the actual earth is not a homogeneous isotropic elastic material as assumed in this model (Mandli et al., 2016). As a result, the deformation of the seafloor is oversimplified. However, because these approaches are standard practice (Mandli et al., 2016) and assume simplicity, it is acceptable for first-order interpretation.

The widths used for the southern rupture scenarios using a length to width scaling (4:1) are potentially problematic, as illustrated by ongoing controversial discussions on whether the Chilean seismogenic zone narrows to the south (Cande et al., 1987; Wang et al., 2007). I did not take into consideration the possibility that the seismogenic zone in southern Chile might not be the same width as the northern rupture. For very large earthquakes, the scale of earthquake-stress drop must be reconciled somehow with the finite width of the seismogenic zone (Mai and Beroza, 2000). Once large earthquakes reach a certain size, their continued growth is constrained in width (Mai and Beroza, 2000): the seismogenic zone is limited in extent by the surface and by the brittle-ductile transition at depth (Scholz, 1982). If I considered a relatively narrow seismogenic zone to the south but maintained the same magnitude, my slip, and therefore seafloor deformation and associated tsunami in the south would be slightly larger.

# CHAPTER VII

# CONCLUSIONS

The 1960 earthquake in Chile ruptured at least 900 km, which triggered a destructive tsunami with waves up to 15 m (Kanamori, 1977; Heaton and Hartzell, 1987; Cisternas et al., 2005). An earthquake of this size in the future could be even more destructive as Chile's population continues to grow. Paleoseismological studies show that earthquakes and tsunamis affect Chilean coastal communities approximately every century (Lay and Kanamori, 1981; Moreno et al., 2010; Ely et al., 2014). By understanding where large earthquakes are more likely to occur from paleotsunami studies, these communities can better plan for future events.

Previous extensive field studies in Chile over several field seasons has allowed me to collect a dataset of tsunami deposits and historical accounts associated with south-central (35-43°S) Chilean tsunamigenic earthquakes (Lomnitz, 2004; Cisternas et al., 2005; Nelson et al., 2009; Fujii and Satake, 2013; Ely et al., 2014; Moernaut et al., 2014; Dura et al., 2015; Garrett et al., 2015; Nentwig et al., 2015; Hong et al., 2016). The overall purpose of this project was to determine if unknown rupture parameters (i.e., magnitude and source location) from past megathrust earthquakes along the coast of Chile can be predicted with tsunami simulations guided by on-land observations (i.e., tsunami deposits or historic written records). To determine whether tsunami simulations are capable of matching these observations, I investigated the sensitivities of tsunami effects (e.g., wave heights and inundation) generated from nine hypothetical

tsunamigenic large earthquakes in south-central Chile that cover the diversity of characteristics from actual past events. The goals of this research are twofold: evaluate the methodology of comparing the tsunami deposit and historical account database to tsunami simulations and develop a proposed list of promising sites for future study of paleotsunamis. These promising sites identify locations on the coast that filter and/or amplify earthquakes from variable rupture sizes and source locations by magnifying differences in tsunami inundation and runup values.

I created nine earthquake scenarios using the tsunami model GeoClaw: $M_w$ 8.6, 8.8, and 9.0 at a northern, central, and southern location. I based their rupture parameters (i.e., length, width, and slip) off recent earthquakes in Chile that had similar magnitudes: the 2010 $M_w$ 8.8 Maule earthquake, the 2015 $M_w$ 8.3 Illapel earthquake, and the 1960 $M_w$ 9.5 Valdivia earthquake. To compare simulations with onshore data and with each other, I used synthetic tide gauges to record waveform data from each model run. I created 99 tide gauges near the shoreline and evenly distributed them throughout the northern, central, and southern modeling boundaries, including tsunami deposit and historical site locations. Analysis of the synthetic tide gauge waveforms enables calculation of arrival times of the tsunami at the tide gauge and wave height highs and lows, and the maximum wave heights allows for projection of tsunami inundation onshore.

After quantitatively and qualitatively assessing sites from tide gauge data, I ended up with 22 promising sites, or locations onshore that magnify differences between tsunami wave heights/arrival times, and therefore filters the earthquake magnitude and/or

source location. These sites are good places to look for past records to determine paleoearthquake size and location. I made additional high-resolution simulations at Andalien, Lenga, Puerto Saavedra, Queule, Quidico, and Tirua that show maximum inundation at each site because the 30-arcsecond resolution of bathymetry and topography used in GeoClaw is not detailed enough to model the dynamics of inundation.

As expected, increasing earthquake magnitude produced larger tsunami wave heights, more sites with tsunami inundation, farther inundation extent, higher seafloor deformation, generally earlier arrival times and greater values of subsidence and uplift. Simulations showed tsunamis from $M_w$ 9.0 earthquakes can inundate coastal plains from nearfield sources, but not exclusively as $M_w$ 8.6 and $M_w$ 8.8 earthquake tsunamis can produce wave heights over 5 m at some sites. At my promising sites, at least one of the three earthquake epicenter locations can be ruled out as a possible source area. Refer to Appendix B for the tide gauge waveforms at all promising sites.

My earthquake input parameters resulted in both uplift and subsidence, which varied due to location and wider seafloor deformation for larger width earthquakes. The northern $M_w$ 8.8 earthquake rupture extent and seismic moment are equivalent to the 2010 earthquake. However, simulated wave heights are smaller than observed wave heights in 2010 likely because of (1) the complex 2010 Maule rupture slip distribution and (2) shelf resonance and edge waves amplifying the wave heights at Constitucion and Concepcion. The central and south $M_w$ 9.0 earthquake is equivalent to the 1960 earthquake in terms of rupture area and seismic moment (Fujii and Satake, 2013;

Moernaut et al., 2014). Between my simulated $M_w$ 9.0 central wave heights and the wave heights that exist from 1960, there is mostly overlap with few exceptions.

Wave heights showed a similar trend between all nine simulations, with wave heights from southern earthquakes being lowest in the northern section and wave heights from northern earthquakes being lowest in the southern section, as expected. Arrival times also showed a predictable trend, with shorter arrival times from northern earthquakes in the north, and longer arrival times from southern earthquakes in the north, for example.

Northern and central sites are more sensitive to the earthquake source location and/or magnitude. The bathymetry on the continental shelf might be the reason the southern section is not as sensitive to earthquake magnitude as the northern and central sections. The energetic consequence resulting from wave interference due to slope irregularities in the southern region are wave reflection and energy dissipation (Horsburgh et al., 2008; Bellotti et al., 2012), resulting in lower and therefore more similar wave heights between scenarios in the south.

Looking at sites within the database of tsunami deposits and historical accounts, specific rupture location and magnitudes are likely to preserve in the tsunami record for the 1575, 1737, 1835, 1837, 1960, and 2010 earthquakes. Data strongly suggests a tsunami from a $M_w$ 9.0 earthquake in the southern region is relatively consistent with the 1575 tsunami observations. Because Quidico, a north-facing shore in the northern nearfield, does not have the 1575 deposit, but Penco does have a record of a tsunami, it is

likely the 1575 northern rupture boundary extends farther north than the $M_w$ 9.0 southern scenario. At sites inundated by the 1835 tsunami, a northern $M_w$ 8.8 scenario is the best solution, while a $M_w$ 9.0 scenario between the central and southern rupture areas is the best solution for the 1837 tsunami. Future tsunami modeling is needed to test all interpretations for past earthquake rupture locations and magnitudes.

In order to apply forward tsunami modeling methods to interpret paleotsunami deposits, it is important to assess the validity of matching on-land observations (i.e., paleotsunami deposits) from the tsunami to the paleoearthquake properties. At 60% of my sites, tsunami wave heights averaged ≥0.5 m between simulations, which is a substantial number of sites in the 1,000-km stretch of the coast of south-central Chile. The number of sites sensitive to magnitude and/or source location amounted to more than half of the total, which leads me to believe these results are tangible considering the quality of bathymetry available. My nine scenarios showed that more extensive comparisons of possible paleoearthquake parameters with on-land observations is an effective and promising approach to defining characteristics of historical and prehistoric events.

# REFERENCES


Abe, K., 1979, Size of great earthquakes of 1837-1974 inferred from tsunami data: Journal of Geophysical Research, v. 84, p. 1561-1568.

Amante, C., and Eakins, B.W., 2009, ETOPO1 1 Arc-Minute Global Relief Model: Procedures, Data Sources and Analysis: NOAA Technical Memorandum NESDIS NGDC-24. National Geophysical Data Center, NOAA, doi:10.7289/V5C8276M (accessed 20 July, 2017).

An, C., Sepulveda, I., and Liu, P.L.F., 2014, Tsunami source and its validation of the 2014 Iquique, Chile, earthquake: Geophysical Research Letters, v. 41, p. 3988–3994.

Angermann, D., Klotz, J., and Reigber, C., 1999, Space-geodetic estimation of the Nazca-South America Euler vector: Earth and Planetary Science Letters, v. 171, p. 329-334.

Arias, J.P., Bronfman, N.C., Cisternas, P.C., and Repetto, P.B., 2017, Hazard proximity and risk perception of tsunamis in coastal cities: Are people able to identify their risk?: PLoS ONE, v. 12, p. 1-13.

Atwater, B.F., Cisternas, M., Yulianto, E., Prendergast, A.L., Jankaew, K., Eipert, A.A., Fernando, W.I.S., Tejakusuma, I., Schiappecasse, I., and Sawai, Y., 2013, The 1960 tsunami on beach-ridge plains near Maullin, Chile: Landward descent, renewed breaches, aggraded fans, multiple predecessors: Andean Geology, v. 40, p. 393-418, doi: 10.5027/andgeoV40n2-a01.

Bahlburg, H., and Spiske, M., 2015, Styles of early diagenesis and the preservation potential of onshore tsunami deposits- A resurvey of Isla Mocha, Central Chile, 2 years after the February 27, 2010, Maule tsunami: Sedimentary Geology, v. 326, p. 33-44.

Barrientos, S., and Ward, S., 1990, The 1960 Chile Earthquake: Coseismic slip from surface deformation: Geophysical Journal International, v. 103, p. 589-598.

Becker, J.J., Sandwell, D.T., Smith, W.H., Braud, F.J., Binder, B., Depner, J., Fabre D., Factor, J., Ingalls, S., Kim, S-H., Ladner, R., Marks, K., Nelson, S., Pharoah, A., Trimmer, R., Von Rosenberg, J., Wallace, G., Weatherall, P., 2009, Global Bathymetry and Elevation Data at 30 Arc seconds Resolution: SRTM30_PLUS: Marine Geodesy, v. 32, p. 355-371.

Bellotti, G., Briganti, R., and Beltrami, G.M., 2012, The combined role of bay and shelf modes in tsunami amplification along the coast: Journal of Geophysical Research, v. 117, p. C08027, doi:10.1029/2012JC008061.

Berger, M.J., and LeVeque, R.J., 1998, Adaptive Mesh Refinement using Wave-Propagation Algorithms for Hyperbolic Systems: Society for Industrial and Applied Mathematics, v. 35, p. 2298-2316.

Bertrand, S., Charlet, F., Chapron, E., Fagel, N., and Batist, M.D., 2008, Reconstruction of the Holocene seismotectonic activity of the Southern Andes from seismites recorded in Lago Icalma, Chila, 39 °S: Elsevier, v. 259, p. 301-322.

Bilek, S.L., 2009, Seismicity along the South American subduction zone: Review of large earthquakes, tsunamis, and subduction zone complexity: Tectonophysics, n.v., n.p., doi:10.1016/j.tecto.2009.02.037.

Bodin, P., and Klinger, T., 1986, Coastal uplift and mortality of intertidal organisms caused by the September 1985 Mexico earthquakes: Science, v. 233, p., 1071-1073.

Bondevik, S., Mangerud, J., Dawson, S., Dawson, A., Lohne, O., 2005, Evidence for three North Sea tsunamis at the Shetland Islands between 8000 and 1500 years ago: Quaternary Science Reviews, v. 24, p. 1757-1775.

Borrero, J.C., Weiss, R., Okal, E.A., Hidyat, R., Suranto, A.D., and Titov, V.V., 2009, The tsunami of 2007 September 12, Bengkulu province, Sumatra, Indonesia:

Post-tsunami field survey and numerical modeling: Geophysical Journal International, v. 178, p. 180-194.

Borrero, J.C., LeVeque R.J., Greer, S.D., O'Neill, S., and Davis, B.N., 2015, Observations and modelling of tsunami currents at the port of Tauranga, New Zealand: Australasian Coasts and Ports Conference 2015: 22nd Australasian Coastal and Engineering Conference and the 15th Australasian Port and Harbour Conference, p. 90.

Bourgeois, J., and Reinhart, M.A., 1989, Onshore erosion and deposition by the 1960 tsunami at Rio Lingue estuary, south-central Chile: Eos Transactions, v. 70, p. 1331.

Campos, J., Hatzfield, D., Madariaga, R., Lopez, G., Kausel, E., Zollo, A., Iannacone, G., Fromm, R., Barrientos, S., and Caen, H.L., 2002, A seismological study of the 1835 seismic gap in south-central Chile: Elsevier, v. 132, p. 177-195.

Cande, S.C., Leslie, R.B., Parra, J.C., and Hobart, M., 1987, Interaction between the Chile Ridge and Chile Trench: geophysical and geothermal evidence: Journal of Geophysical Research: Solid Earth, v. 92, p. 495-520.

Carvajal, M., Cisternas, M., and Catalan, P.A., 2017, Source of the 1730 Chilean earthquake from historical records: Implications for the future tsunami hazard on the coast of Metropolitan Chile: Journal of Geophysical Research Solid Earth, v. 122, p. 3648-3660, doi:10.1002/2017JB014063.

Cifuentes, I., 1989, The 1960 Chilean earthquakes: Journal of Geophysical Research, v. 94, p. 665-680.

Cisternas, M., Atwater, B.F., Torrejón, F., Sawai, Y., Machuca, G., Lagos, M., Eipert, A., Youlton, C., Salgado, I., Kamataki, T., Shishikura, M., Rajendran, C.P., Malik, J.K., Rizal, Y., and Husni, M., 2005, Predecessors of the giant 1960 Chile earthquake: Nature, v. 437, p. 404–407, doi:10.1038/nature03943.

Cisternas, M., Torrejon, F., Gorigoitia, N., 2012, Amending and complicating Chile's seismic catalog with the Santiago earthquake of 7 August 1580: Journal of South American Earth Sciences, v. 33, p. 102-109, doi:10.1016/j.jsames.2011.09.002.

Cisternas, M., Garrett, E., Wesson, R., Dura, T., and Ely, L., 2017, Unusual geologic evidence of coeval seismic shaking and tsunamis shows variability in earthquake size and recurrence in the area of the giant 1960 Chile earthquake: Elsevier, v. 385, p. 101-113.

Clague, J.J., and Bobrowsky, P.T., 1994, Evidence for a large earthquake and tsunami 100-400 yr ago on western Vancouver Island, British Columbia: Quaternary Research, v. 41, p. 176-184.

Clawpack Development Team, accessed 2017, Clawpack Version 5.4.1, http://www.clawpack.org, doi:10.5281/zenodo.262111.

Comte, D., Pardo, M., Dorbath, L., Dorbath, C., Haessler, H., Rivera, L., Cisternas, A., and Ponce, L., 1994, Determination of seismogenic interpolate contact zone and crustal seismicity around Antofagasta, northern Chile using local data: Geophysical Journal International, v. 116, p. 553-561.

Darwin, C., 1851, Geological observations on coral reefs, volcanic islands and on South America: Londres, 768 pp.

Dawson, A.G., 1994, Geomorphological effects of tsunami runup and backwash: Geomorphology, v. 10, p. 83-94.

Delouis, B., Nocquet, J.M., and Vallee, M., 2010, Slip distribution of the February 27, 2010 Mw=8.8 Maule earthquake, central Chile, from static and high-rate GPS, InSAR, and broadband teleseismic data: Geophysical Research Letters, v. 37, p. 1-7, doi:10.1029/2010GL043899.

Dura, T., Cisternas, M., Horton, B.P., Ely, L.L., Nelson, A.R., Wesson, R.L., Pilarczyk, J.E., 2015, Coastal evidence for Holocene subduction-zone earthquakes and tsunamis in central Chile: Quaternary Science Reviews, v. 113, p.93-111.

Dura, T., Horton, B., Cisternas, M., Ely, L.L., Hong, I., Nelson, A.R., Wesson, R., Pilarczyk, J.E., Parnell, A.C., and Nikitina, D., 2017, Subduction zone slip variability during the last millennium, south-central Chile: Elsevier, v. 175, p. 112-137.

Ely, L.L., Cisternas, M., Wesson, R.L., and Dura, T., 2014, Five centuries of tsunamis and land level changes in the overlapping rupture area of the 1960 and 2010 Chilean earthquakes: Geology, v. 42, p. 995–998, doi:10.1130/G35830.1.

Farias, M., Vargas, G., Tassara, G., Carretier, S., Baize, S., Melnick, D., and Bataille, K., 2010, Land-level changes produced by the Mw 8.8 2010 Chilean Earthquake: Science Express, n.v., p. 1-2.

Fowler, C.M.R., 1990, The solid earth: Cambridge, UK, Cambridge University Press, 472 pp.

Fujii, Y., Satake, K., Sakai, S.I., Shinohara, M., and Kanazawa, T., 2011, Tsunami source of the 2011 off the Pacific coast of Tohoku Earthquake: Earth, Planets, and Space, v. 63, p. 55.

Fujii, Y., and Satake, K., 2013, Slip distribution and seismic moment of the 2010 and 1960 Chilean earthquakes inferred from tsunami waveforms and coastal geodetic data: Pure and Applied Geophysics, n.v., p. 1493-1509, doi:10.1007/s00024-012-0524-2.

Fujiwara, O., Masuda, F., Sakai, T., Irizuki, T., Fuse, K., Daiyoni, K., 1999, Holocene tsunami deposits detected by drilling in drowned valleys of Boso and Miura peninsulas: Quaternary Research, v. 38, p. 41-58.

Garrett, E., Shennan, I., Watcham, E.P., and Woodroffe, S.A., 2013, Reconstructing paleoseismic deformation, 1: Modern analogues from the 1960 and 2010 Chilean great earthquakes: Quaternary Science Reviews, v. 75, p. 11-21, doi: 10.1016/j.quascirev.2013.04.007.

Garrett, E., Shennan, I., Woodroffe, S.A., Cisternas, M., Hocking, E.P., and Gulliver, P., 2015, Reconstructing paleoseismic deformation, 2: 1000 years of great earthquakes at Chucalén, south central Chile: Quaternary Science Reviews, v. 113, p. 112–122, doi:10.1016/j.quascirev.2014.10.010.

Geist, E.L., 2002, Complex earthquake rupture and local tsunamis: Journal of Geophysical Research, v. 107, p. 1-6.

George, D.L., and LeVeque, R.J., 2006, Finite volume methods and adaptive refinement for global tsunami propagation and local inundation: Science of Tsunami Hazards, v. 24, p. 319-328.

Goda, K., Mai, P.M., Yasuda, T., Mori, N., 2014, Sensitivity of tsunami wave profiles and inundation simulations to earthquake slip and fault geometry for the 2011 Tohoku earthquake: Earth, Planets and Space, v. 66, p. 105. http://dx.doi.org/10.1186/1880-5981-66-105.

Goff, J., Pearce, S., Nichol, S.L., Chague-Goff, C., Horrocks, M., Strotz, L., 2010, Multi-proxy records of regionally-sourced tsunamis, New Zealand: Elsevier, v. 188, p. 369-382.

Gonzalez, F., R. J. LeVeque, P. Chamberlain, B. Hirai, J. Varkovitzky, and D.L. George, 2011, GeoClaw Results for the NTHMP Tsunami Benchmark Problems, [NTHMP] National Tsunami Hazard Mitigation Program: Proceedings and Results of the 2011 NTHMP Model Benchmarking Workshop, Boulder: U.S. Department of Commerce/NOAA/NTHMP (NOAA Special Rpt), n.v., p. 436.

Goto, K., Chague-Goff, C., Fujino, S., Goff, J., Jaffe, B., Nishimura, Y., Richmond, B., Sugawara, D., Szcucinski, W., Tappin, D.R., and Witter, R.C., 2011, New insights

of tsunami hazard from the 2011 Tohoku-oki event: Marine Geology, v. 290, p. 46-50.

Gusman, A.R., Tanioka, Y., MacInnes, B., and Tsushima, H., 2014, A methodology for near-field tsunami inundation forecasting: Application to the 2011 Tohoku tsunami: Journal of Geophysical Research: Solid Earth, v. 119, p. 8186-8206, doi: 10.1002/2014JB010958.

Haberland, C., Rietbrock, A., Lange, D., Bataille, K., and Dahm, T., 2009, Structure of the seismogenic zone of the southcentral Chilean margin revealed by local earthquake traveltime tomography: Journal of Geophysical Research, v. 114, p. 1-17, doi: 10.1029/2008JB005802.

Hayes, G.P., Wald, D.J., and Johnson, R.L., 2012, Slab 1.0: A three-dimensional model of global subduction zone geometries: Journal of Geophysical Research, v. 117, n.p., doi: 10.1029/2011JB008524.

Hayes, G.P., Herman, M.W., Barnhart, W.D., Furlong, K.P., Riquelme, S., Benz, H., Bergman, E., Barrientos, S., Earle, P.S. and Samsonov, S., 2014, Continuing megathrust earthquake potential in Chile after 2014 Iquique earthquake: Nature, v. 512, p. 295.

Heaton, T.H., and Hartzell, S.H., 1987, Earthquake hazards on the Cascadia subduction zone: Science, v. 236, p. 162-168.

Hirata, K., Geist E.L., Stake, K., Tanioka, Y. and Yamaki S., 2003, Slip distribution of the 1952 Tokachi-Oki earthquake (M 8.1) along the Kuril Trench from tsunami waveform inversion: Journal of Geophysical Research, v. 108, doi: 10.1029/2002JB001976.

Hong, I., Dura, T., Ely, L.L., Horton, B.P., Nelson, A.R., Cisternas, M., Nikitina, D., and Wesson, R.L., 2016, A 600-year-long stratigraphic record of tsunamis in south-central Chile: The Holocene, n.v., p. 1-13, doi: 10.1177/0959683616646191.

Horrillo, J., Knight, W., and Kowalik, Z., 2008, Kuril islands tsunami of November 2006: 2. Impact at Crescent City by local enhancement: Journal of Geophysical Research, v. 113, p. C01021, doi: 10.1029/2007JC004404.

Horsburgh, K.J., Wilson, C., Baptie, B.J., Cooper, A., Cresswell, D., Musson, R.M.W., Ottemoller, L., Richardson, S., and Sargeant, S.L., 2008, Impact of a Lisbon-type tsunami on the U.K. coastline and the implications for tsunami propagation over broad continental shelves: Journal of Geophysical Research, v 113, p. C04007, doi:10.1029/2007JC004425.

Ide, S., Baltay, A., and Beroza, G.C., 2011, Shallow dynamic overshoot and energetic deep rupture in the 2011 Mw 9.0 Tohoku-Oki earthquake: Science, v. 332, p. 1426-1429.

Imamura, F., 2009, Tsunami modeling: inundation, in The Sea: Tsunamis, E.N. Bernard and A.R. Robinson (Editors): Harvard University Press, v.15, p. 321-332.

Intergovernmental Oceanographic Commission, accessed 2014, The GEBCO_2014 Grid: International Hydrographic Organization and Intergovernmental Oceanic Commission of UNESCO.

Jaffe, B. E., and Gelfenbaum, G., 2002, Using tsunami deposits to improve assessment of tsunami risk: Solutions to Coastal Disasters ‘02, Conference Proceedings, ASCE, p. 836-847.

Jaffe, B. E., and Gelfenbaum, G., 2007, A simple model for calculating tsunami flow speed from tsunami deposits: Sedimentary Geology, v. 200, p. 836-847.

Jankaew, K., Atwater, B., Sawai, Y., Choowang, M., Charoentitirat, T., Martin, M., and Prendergast, A., 2008, Medieval forewarning of the 2004 Indian Ocean tsunami in Thailand: Nature, v. 455, p. 1228-1231.

Kanamori, H., 1977, The energy release in great earthquakes: Journal of Geophysical Research, v. 82, p. 2981-2987.

Kanamori, H., 1978, Quantification of Earthquakes: Nature, v. 271, p. 411-414.

Kelleher, J., and McCann, W., 1976, Buoyant Zones, Great Earthquakes, and Unstable Boundaries of Subduction: Journal of Geophysical Research, v. 81, p. 4885-4896.

Kelsey, H.M., Witter, R.C., Hemphill-Haley, E., 2002, Plate-boundary earthquakes and tsunamis of the past 5500 yr, Sixes River estuary, southern Oregon: Geological Society of America Bulletin, v. 114, p. 298-314.

Kempf, P., Moernaut, J., Van Daele, M., Vandoorne, W., Pino, M., Urrutia, R., and De Batist, M., 2017, Coastal Lake sediments reveal 5500 years of tsunami history in south central Chile: Elsevier, v. 161, p. 99-116, http://dx.doi.org/10.1016/j.quascirev.2017.02.018 0277-3791.

Lander, J.F., and Lockridge, P.A., 1989, United States tsunamis 1690-1988: National Geophysical Data Center Publications, n.v., p. 41-42.

Lario, J., Zazo, C., and Goy, J.L., 2016, Tectonic and morphosedimentary features of the 2010 Chile earthquake and tsunami in the Arauco Gulf and Mataquito River (Central Chile): Geomorphology, v. 267, p. 16-24.

Lay, T., and Kanamori, H., 1981, An asperity model of large earthquake sequences: Earthquake prediction, n.v., p. 579-592.

Lay, T., Ammon, C.J., Kanamori, H., Koper, K.D., Sufri, A., and Hutko, A.R., 2010, Teleseismic inversion for rupture process of the 27 February 2010 Chile (Mw 8.8) earthquake: Geophysical Research Letters, v. 37, p. 1-5, doi:10.1029/2010GL043379.

Leonard, L.J., Currie, C.A., Mazzotti, S., and Hyndman, R.D., 2010, Rupture area and displacement of past Cascadia great earthquakes from coastal coseismic

subsidence: Geological Society of America Bulletin, n.v., p. 1-18, doi:10.1130/B30108.

LeVeque, R.J., 2002, Finite volume methods for hyperbolic problems: Cambridge University Press, v. 31, 558 pp.

LeVeque, R.J., George, D.L., and Berger, M.J., 2011, Tsunami modelling with adaptively refined finite volume methods: Acta Numerica, v. 20, p. 211–289, doi:10.1017/S0962492911000043.

Li, L., Lay, T., Cheung, K.F., and Ye, F., 2016, Joint modeling of teleseismic and tsunami wave observations to constrain the 16 September 2015 Illapel, Chile, Mw8.3 earthquake rupture process: Geophysics Research Letters, v. 43, p. 4303–4312, doi:10.1002/2016GL068674.

Liu, P., 2009, Tsunami modeling: Propagation, in The Sea: Tsunamis E.N. Bernard and A.R. Robinson (Editors): Harvard University Press, v. 15, p. 295-319.

Lockridge, P.A., 1985, Tsunamis in Peru-Chile: World Data Center A for Solid Earth Geophysics, report SE-39, n.v., n.p.

Lomnitz, C., 1970, Major earthquakes and tsunamis in Chile during the period 1535 to 1955, Geologische Rundschau, v. 59, p. 938-960.

Lomnitz, C., 2004, Major earthquakes of Chile: A Historical Survey, 1535-1960: Seismological Research Letters, v. 75, p. 368-378, doi:10.1785/gssrl.75.3.368.

Lorito, S., Romano, F., Atzori, S., Tong, X., Avallone, A., McCloskey, M., Cocco, M., Boschi, E., and Piatanesi, A., 2011, Limited overlap between the seismic gap and coseismic slip of the great 2010 Chile earthquake: Nature Geoscience Letters, n.v., p. 1-5, doi:10.1038/NGEO1073

MacInnes, B.T., Weiss, R., Bourgeois, J., and Pinegina, T.K., 2010, Slip Distribution of the 1952 Kamchatka Great Earthquake Based on Near-Field Tsunami Deposits and Historical Records. Bulletin of the Seismological Society of America, v. 100, p. 1695-1709, doi: 10.1785/0120090376.

MacInnes, B.T., Gusman, A.R., LeVeque, R.J., and Tanioka, Y., 2013, Comparison of Earthquake Source Models for the 2011 Tohoku Event Using Tsunami Simulations and Near-Field Observations. Bulletin of the Seismological Society of America, v. 103, p. 1256–1274, doi:10.1785/0120120121.

Mai, M., and Beroza, G.C., 2000, Source scaling properties from finite-fault-rupture models: Bulletin of Seismological Society of America, v. 90, p. 604-615.

Mandli, K.T., Ahmadia, A.J., Berger, M., Calhoun, D., George, D.L., Hadjimichael, Y., Ketcheson, D.I., Lemoine, G.I., and LeVeque, R.J., 2016, Clawpack: building an open source ecosystem for solving hyperbolic PDEs: PeerJ Computer Science, n.v., n.p., doi10.7717/peerj-cs.68.

Martin, M.E., Weiss, R., Bourgeois, J., Pinegina, T.K., Houston, H., and Titov, V.V, 2008, Combining constraints from tsunami modeling and sedimentology to untangle the 1969 Ozernoi and 1971 Kamchatskii tsunamis: Geophysical Research Letters, v. 35, p. 1-6, doi: 10.1029/2007GL032349.

Martin, M.W., Kato, T.T., Rodriguez, C., Godoy, E., Duhart, P., McDonough, M., and Campos, A., 1999, Evolution of the late Paleozoic accretionary complex and overlying forearc-magmatic arc, south-central Chile (38°–41°S): Constraints for the tectonic setting along the southwestern margin of Gondwana: Tectonics, v. 18, p. 582-605, doi: 10.1029/1999TC900021.

McCloskey, J., Antonioli, A., Piatanesi, A., Sieh, K., Steacy, S., Nalbant, S., Cocco, M., Giunchi, C., Huang, J.D., Dunlop, P., 2008, Tsunami threat in the Indian Ocean from a future megathrust earthquake west of Sumatra: Earth and Planetary Science Letters, v. 265, p. 61–81.

Melnick, D., Bookhagen, B., Echtler, H.P., and Strecker, M.R., 2006, Coastal deformation and great subduction zone earthquakes, Isla Santa Maria, Chile (37 S): Geological Society of America Bulletin, v. 118, p. 1463-1480.

Melnick, D., Cisternas, M., Moreno, M., & Norambuena, R., 2012, Estimating coseismic coastal uplift with an intertidal mussel: calibration for the 2010 Maule Chile earthquake (Mw 8.8): Quaternary Science Reviews, v. 42, p. 29–42. doi:10.1016/j.quascirev.2012.03.012.

Metois, M., Vigny, C., Socquet, A., Delorme, A., Morvan, S., Ortega, I., and Valderas-Bermejo, C.M., 2014, GPS-derived interseismic coupling on the subduction and seismic hazards in the Atacama region, Chile: Geophysical Journal International, v. 196, p. 644-655, https://doi.org/10.1093/gji/ggt418.

Minoura, K., and Nakaya, S., 1991, Traces of tsunami preserved in intertidal lacustrine and marsh deposits: Some examples from northeast Japan: Journal of Geology, v. 99, p. 265-287.

Moernaut, J., Batist, M.D., Charlet, F., Heirman, K., Chapron, E., Pino, M., Brummer, R., and Urrutia, R., 2007, Giant earthquakes in south-central Chile revealed by Holocene mass-wasting events in Lake Puyehue: Sedimentary Geology, v. 195, p. 239-256. doi:10.1016/j.sedgeo.2006.08.005.

Moernaut, J., Daele, M.V., Heirman, K., Fontijn, K., Strasser, M., Pino, M., Urrutia, R., and De Batist, M., 2014, Lacustrine turbidites as a tool for quantitative earthquake reconstruction: New evidence for a variable rupture mode in south central Chile: Journal of Geophysical Research Solid Earth, v. 119, p. 1607–1633, doi:10.1002/2013JB010738.

Monecke, K., Finger, W., Klarer, D., Kongko, W., McAdoo, B.G., Moore, A.L., Sudrajat, S.U., 2008, A 1,000-year sediment record of tsunami recurrence in northern Sumatra: Nature, v. 455, p. 1232-1234.

Moreno, M.S., Bolte, J., Klotz, J., and Melnick, D., 2009, Impact of megathrust geometry on inversion of coseismic slip from geodetic data: Application to the 1960 Chile

earthquake: Geophysical Research Letters, v. 36, n.p., doi:10.1029/2009GL039276.

Moreno, M., Rosenau, M., and Oncken, O., 2010, 2010 Maule earthquake slip correlates with pre-seismic locking of Andean subduction zone: Nature, v. 467, p. 198–202, doi:10.1038/nature09349.

Moreno, M., Melnick, D., Rosenau, M., Bolte, J., Klotz, J., Echtler, H., Baez, J., Bataille, K., Chen, J., Bevis, M., Hase, H., and Oncken, O., 2011, Heterogeneous plate locking in the South-Central Chile suduction zone: Building up the next great earthquake: Earth and Planetary Science Letters, v. 305, p. 413-424. doi:10.1016/j.epsl.2011.03.025.

Mori, N., Mai, P.M., Goda, K., and Yasuda, T., 2017, Tsunami inundation variability from stochastic rupture scenarios: application to multiple inversions of the 2011 Tohoku, Japan earthquake: Elsevier, v. 127, p. 88-105, doi:10.1016/j.coastaleng.2017.06.013.

Morton, R.A., Gelfenbaum, G., Buckley, M.L., and Richmond, B.M., 2011, Geological effects and implications of the 2010 tsunami along the central coast of Chile: Elsevier, v. 242, p. 34-51, doi: 10.1016/j.sedgeo.2011.09.004.

Munoz, J., Troncosco, R., Duhart, P., Crignola, P., Farmer, L., and Stern, C.R., 2000, The relation of the mid-Tertiary coastal magmatic belt in south-central Chile to the late Oligocene increase in plate convergence rate: Revista geologica de Chile, v. 27, n. p., http://dx.doi.org/10.4067/S0716-02082000000200003.

National Geophysical Data Center/World Data Service (NGDC/WDS), (accessed 2017) GEODAS search criteria selection: NOAA, http://www.ngdc.noaa.gov/mgg/geodas/geodas.html.

National Geophysical Data Center/World Data Service (NGDC/WDS), (accessed 2018a) Global Historical Tsunami Database: National Geophysical Data Center, NOAA, doi: 10.7289/V5PN93H7.

National Geophysical Data Center/World Data Service (NGDC/WDS), (accessed 2018b) Significant Earthquake Database: National Geophysical Data Center, NOAA, doi: 10.7289/V5TD9V7K.

Nanayama, F., Satake, K., Furukawa, R., Shimokawa, K., Atwater, B.F., Shigeno, K., Yamaki, S., 2003, Unusually large earthquakes inferred from tsunami deposits along the Kuril trench: Nature, v. 242, p. 660-663.

Nelson, A.R., Shennan, I., and Long, A.J., 1996, Identifying coseismic subsidence in tidal-wetland stratigraphic sequences at the Cascadia subduction zone of western North America: Journal of Geophysical Research, v. 101, p. 6115-6135.

Nelson, A.R., Kashima, K., Bradley, L.A., 2009, Fragmentary evidence of great earthquake subsidence during Holocene Emergence, Valdivia Estuary, South Central Chile: Bulletin of the Seismological Society of America, v. 99, p. 71-86, doi: 10.1785/0120080103.

Nentwig, V., Tsukamoto, S., Frechen, M., and Bahlburg, H., 2015, Reconstructing the tsunami record in Tirua, Central Chile beyond the historical record with quartz-based SAR-OSL: Quaternary Geochronology, n.v. p. 1-7, http://dx.doi.org/10.1016/j.quageo.2015.05.020.

Ninomiya, S., 1960, Tsunami in Tohoku coast induced by earthquake in Chile; a chronological review: Tohoku Kenkyu [in Japanese with English summary], v. 10, p. 19-23.

Okada, R., 1985, Surface deformation due to shear and tensile faults in a half-space: Bulletin of the Geological Society of America, v. 75, p. 1135-1154.

Okal, E.A., and Synolakis, C.E., 2004, Source discriminants of near-field tsunamis: Geophysical Journal International, v. 158, p. 899–912.

Okal, E.A., 2009, Excitation of tsunamis by earthquakes, in The Sea: Tsunamis v. 15, p. 137–177.

Omira, R., Baptista, M.A., Lisboa, F., 2016, Tsunami Characteristics Along the Peru–Chile Trench: Analysis of the 2015 Mw8.3 Illapel, the 2014 Mw8.2 Iquique and the 2010 Mw8.8 Maule Tsunamis in the Near-field: Pure and Applied Geophysics, n.v., n.p., doi:10.1007/s00024-016-1277-0.

Peterson, C.D., Carver, G.A., Cruikshank, K.M., Abramson, H.F., Garrison-Laney, C.E., Dengler, L.A., 2011, Evaluation of the use of paleotsunami deposits to reconstruct inundation distance and runup heights associated with prehistoric inundation events, Crescent City, southern Cascadia margin: Earth Surface Processes and Landforms, v. 36, p. 967-980.

Pinegina, T.K., and Bourgeois, J., 2001, Historical and paleo-tsunami deposits on Kamchatka, Russia: long-term chronologies and long-distance correlations: Natural Hazards and Earth System Sciences, v. 1, p. 177-185.

Plafker, G., and Savage, J., 1970, Mechanisms of Chilean earthquakes of May 21 and May 22, 1960: Geological Society of America Bulletin, v. 81, p. 1001-1030.

Plafker, G., 1972, Alaskan earthquake of 1964 and Chilean earthquake of 1960-Implications for arc tectonics: Journal of Geophysical Research, v. 77, p. 901-925.

Pollitz, F.F., Brooks, B., Tong, X., Bevis, M.G., Foster, J.H., Burgmann, R., Smalley Jr., R., Vigny, C., Socquet, A., Ruegg, J.C., Campos, J., Barrientos, S., Parra, H., Baez Soto, J.C., Cimbaro, S., and Blanco, Mauro, 2011, Coseismic distribution of the February 27, 2010 Mw 8.8 Maule, Chile earthquake: Geophysical Research Letters, v. 38, p. L09309, doi:10.1029/2011GL047065.

Rhodes, B., Tuttle, M., Horton, B., Doner, L., Kelsey, H., Nelson, A., and Cisternas, M., 2006, Paleotsunami Research: Eos, Transactions American Geophysical Union, v. 87, p. 205-209.

Roeber, V., Yamazaki, Y., and Cheung, K.F., 2010, Resonance and impact of the 2009 Samoa tsunami around Tutuila, American Samoa: Geophysical Research Letters, v. 37, p. L21604, doi: 10.1029/2010GL044419.

Ruiz, A., 2016, Investigating taphonomic changes of deposits and modeling of the 2010 earthquake and tsunami in south-central Chile, [Master's thesis]: Central Washington University, 124 p.

Satake, K., 2005, Tsunamis: case studies and recent developments: Springer Science & Business Media, v. 23, 343 pp.

Satake, K., Nanayama, F., and Yamaki, S., 2008, Fault models of unusual tsunami in the 17th century along the Kuril trench: Earth, Planets, and Space, v. 60, p. 925-935.

Scheffers, A., Kelletat, D., Voett, A., May, S.M., Scheffers, S., 2008, Late Holocene tsunami traces on the western and southern coastlines of the Peloponnesus (Greece): Earth and Planetary Science Letters, v. 269, p. 271-279.

Scholz, C. H., 1982, Scaling laws for large earthquakes: consequences for physical models: Bulletin of the Seismological Society of America, v. 72, p. 1–14.

Siever, S., Villegas, H., and Barros, G., 1963, The seismic sea wave of 22 May 1960 along the Chilean coast: Bulletin of the Seismological Society of America, v. 53, p. 1125–1190.

Smith, D.E., Foster, I.D., Long, D., and Shi S., 2007, Reconstructing the pattern and depth of flow onshore in a palaeotsunami from associated deposits: Sedimentary Geology, v. 200, p. 362-371.

Synolakis, C.E., Bernard, E.N., Titov, V.V., Kanoglu, U., and Gonzalez, F.I., 2008, Validation and verification of tsunami numerical models: Pure and Applied Geophysics, v. 165, p. 2197-2228.

Szczuciński, W., 2012, The post-depositional changes of the onshore 2004 tsunami deposits on the Andaman Sea coast of Thailand: Natural Hazards v. 60 p. 115, https://doi.org/10.1007/s11069-011-9956-8.

Tang, L., Titov, V.V., and Chamberlin, C.D., 2009, Development, testing, and applications of site-specific tsunami inundation models for real-time forecasting: Journal of Geophysical Research, v. 114, p. 1-22, doi: 10.1029/2009JC005476.

Tichelaar, B.W., and Ruff, L.J., 1991, Seismic coupling along the Chilean subduction zone: Journal of Geophysical Research, v. 96, p. 11,997-12,022.

Titov, V.V, and Gonzalez, F.I., 1997, Implementation and testing of the method of splitting tsunami (MOST) model: n.p. n.v., p. 1-11.

Udias, A., Madariaga, R., Buforn, E., Munoz, D., and Ros, D., 2012, The Large Chilean Earthquakes of 1647, 1657, 1730, and 1751 from Contemporary Documents: Bulletin of the Seismological Society of America, v. 102, p. 1639-1656, doi: 10.1785/0120110289.

Veblen, T.T., Claudio Donoso, Z., Schlegel, F.M., and Bernardo Escobar, R., 1981, Forest dynamics in south-central Chile: Journal of Biogeography, v. 8, p. 211-247, doi:10.2307/2844678.

Vigny, C., Socquet, A., Peyrat, S., Ruegg, J.C., Metois, M., Madariaga, R., Morvan, S., Lancieri, M., Lacassin, R., Campos, J., Carrizo, D., Bejar-Pizarro, M., Barrientos, S., Armijo, R., Aranda, C., Valderas-Bermejo, M.C., Ortega, I., Bondoux, F., Baize, S., Lyon-Caen, H., Pavez, A., Vilotte, J.P., Bevis, M., Brooks, B., Smalley, R., Parra, H., Baez, J.C., Blanco, M., Cimbaro, S., and Kendrick, E., 2011, The 2010 *M*w 8.8 Maule Megathrust Earthquake of Central Chile, Monitored by GPS: Science, v. 332, p. 1417-1421.

Volker, D., Geerson, J., Contreras-Reyes, E., Sellanes, J., Pantoja, S., Rabbel, W., Thorwart, M., Reichert, C., Block, M., and Weinrebe, W.R., 2012, Morphology and geology of the continental shelf and upper slope of southern Central Chile (33°S–43°S): International Journal of Earth Sciences (Geologische Rundschau), n.v. p. 1-23, doi: 10.1007/s00531-012-0795-y.

Wang, K., Wells, R., Mazzotti, S., Hyndman, R.D., Sagiya, T., 2003, A revised dislocation model of interseismic deformation of the Cascadia subduction zone: Journal of Geophysical Research, v. 108, n.p., doi: 10.1029/2001JB001227.

Wang, K., 2007, Elastic and viscoelastic models for subduction zone earthquake cycles, in Dixon T.H. Moore S.C., eds., The Seismogenic Zone of Subduction Thrust Faults: New York, Columbia University Press, p. 540-575.

Wang, K., Hu, Y., Bevis, M., Kendrick, E., Smalley Jr., R., Barriga Vargas, R., and Lauria, E., 2007, Crustal motion in the zone of the 1960 Chile earthquake: detangling earthquake-cycle deformation and forearc-sliver translation: Geochemistry, Geophysics, Geosystems, v. 8, p. 1-14, doi:10.1029/2007GC001721.

Watanabe, H., 1998, Comprehensive List of Destructive Tsunamis to Hit the Japanese Islands [In Japanese]: University of Tokyo Press, Tokyo.

Weatherall P., Marks, K. M., Jakobsson, M., Schmitt, T., Tani, S., Arndt, J. E., Rovere, M., Chayes, D., Ferrini, V., and Wigley, R., 2015, A new digital bathymetric model of the world's oceans: Earth and Space Science, v. 2, p. 331–345, doi:10.1002/2015EA000107.

Wesson, R.L., Melnick, D., Cisternas, M., Moreno, M., and Ely, L.L., 2015, Vertical deformation through a complete seismic cycle at Isla Santa Maria, Chile: Nature Geoscience, v. 8, p. 547-553, doi: 10.1038/NGEO2468.

Wright, C., and Mella, A., 1963, Modifications to the soil pattern of south-central Chile resulting from seismic and associated phenomena during the period May to August 1960: Bulletin of the Seismological Society of America, v. 53, p. 1367–1402.

Yamazaki, Y., and Cheung, K.F., 2011, Shelf resonance and impact of near-field tsunami generated by the 2010 Chile earthquake: Geophysical Research Letters, v. 38, p. L12605, doi: 10.1029/2011GL047508.

Yasuda, S., Verdugo, R., Konagai, K., Sugano, T., Villalobos, F., Okamura, M., Tobita, T., Torres, A., Towhata, I., 2010, Geotechnical damage caused by the 2010 Maule, Chile earthquake: ISSMGE Bulletin, v. 4, p. 16-27.

Zakharova, O., Hainzl, S., and Bach, C., 2013, Seismic moment ratio of aftershocks with respect to main shocks: Journal of Geophysical Research: Solid Earth, v. 118, p. 5856-5864, doi: 10.1002/2013JB010191.

# APPENDICES

## APPENDIX A

### Inundation at Promising Sites

Table A1: Maximum wave heights from my nine simulations compared to the minimum elevation needed for the tsunami to inundate shows that all 22 final promising sites could have tsunami inundation and possible tsunami deposits.

| | | | **Maximum Wave Heights (m)** | | | | | | | | |
|---|---|---|---|---|---|---|---|---|---|---|---|
| **Tide Gauge** | site name | minimum elevation needed for inundation (m) | $M_w$ 8.6N | $M_w$ 8.6C | $M_w$ 8.6 S | $M_w$ 8.8N | $M_w$ 8.8C | $M_w$ 8.8 S | $M_w$ 9.0N | $M_w$ 9.0C | $M_w$ 9.0 S |
| **55** | Los Rabanos | 2.0 | 6.2 | 0.8 | 0.3 | 8.8 | 1.8 | 0.5 | 11.9 | 3.3 | 0.9 |
| **6** | Constituc-ion | 4.0 | 4.3 | 0.6 | 0.4 | 5.8 | 1.9 | 0.6 | 8.3 | 2.8 | 1.2 |
| **68** | Tubul | 8.0 | 4.2 | 1.9 | 0.3 | 8.5 | 8.5 | 0.6 | 9.2 | 8.5 | 1.3 |
| **27** | Playa Llancao | 2.5 | 1.1 | 3.4 | 0.3 | 1.9 | 4.7 | 0.6 | 4.2 | 6.8 | 1.6 |
| **28** | W of Guape | 3.0 | 2.3 | 3.3 | 0.3 | 1.7 | 4.8 | 0.6 | 3.1 | 7.0 | 1.9 |
| **76** | W of Lago Lleulleu | 4.0 | 1.3 | 3.4 | 0.3 | 2.5 | 4.6 | 0.6 | 4.6 | 6.6 | 1.6 |
| **29** | Quidico | 2.0 | 2.2 | 2.2 | 0.3 | 2.0 | 3.7 | 0.6 | 6.2 | 5.0 | 1.4 |
| **60** | Tirua | 2.0 | 0.8 | 2.2 | 0.6 | 1.4 | 3.5 | 1.1 | 4.5 | 4.4 | 2.6 |
| **81** | N Saavedra | 4.0 | 0.6 | 3.7 | 0.5 | 1.4 | 4.7 | 1.9 | 2.3 | 6.6 | 3.4 |
| **31** | Puerto Saavedra | 1.5 | 1.6 | 4.3 | 0.6 | 1.5 | 5.6 | 1.6 | 4.4 | 7.9 | 3.1 |
| **83** | Chelle | 5.5 | 0.9 | 3.7 | 0.5 | 1.6 | 5.2 | 1.7 | 2.6 | 7.3 | 3.3 |
| **84** | Reduccion Porma | 2.0 | 0.9 | 4.0 | 0.5 | 1.6 | 5.5 | 1.6 | 3.0 | 7.6 | 3.1 |
| **85** | Nueva Tolten | 3.0 | 1.0 | 4.0 | 0.9 | 1.5 | 5.7 | 1.8 | 2.5 | 7.8 | 3.1 |
| **61** | W of Puraloco | 2.5 | 1.2 | 4.4 | 1.4 | 2.0 | 6.0 | 2.5 | 2.5 | 8.0 | 4.4 |
| **64** | Queule | 3.0 | 1.3 | 4.1 | 0.6 | 2.2 | 5.8 | 1.9 | 2.2 | 7.9 | 2.8 |
| **65** | Missisipi | 4.0 | 1.1 | 4.4 | 0.6 | 1.1 | 6.2 | 1.8 | 2.5 | 8.8 | 4.4 |
| **34** | S of Maiquillahue | 2.5 | 1.6 | 3.9 | 0.6 | 1.2 | 5.4 | 2.0 | 3.2 | 7.6 | 4.1 |

Table A1 (Continued): Maximum wave heights from my nine simulations compared to the minimum elevation needed for the tsunami to inundate shows that all 22 final promising sites could have tsunami inundation and possible tsunami deposits.

| **Tide Gauge** | **site name** | **minimum elevation needed for inundation (m)** | **$M_w$ 8.6N** | **$M_w$ 8.6C** | **$M_w$ 8.6 S** | **$M_w$ 8.8N** | **$M_w$ 8.8C** | **$M_w$ 8.8 S** | **$M_w$ 9.0N** | **$M_w$ 9.0C** | **$M_w$ 9.0 S** |
|---|---|---|---|---|---|---|---|---|---|---|---|
| **71** | Chaihuin | 5.5 | 0.3 | 3.2 | 0.6 | 0.6 | 4.1 | 2.4 | 1.3 | 6.4 | 4.8 |
| **72** | Pucatrihue | 4.0 | 0.6 | 2.3 | 2.2 | 1.1 | 4.6 | 3.1 | 1.9 | 6.9 | 5.0 |
| **48** | Chepu | 3.0 | 0.3 | 2.1 | 2.5 | 0.6 | 3.5 | 4.5 | 1.3 | 5.2 | 6.2 |
| **66** | Lake Huelde/ Cucao | 2.0 | 0.3 | 0.9 | 2.7 | 0.3 | 1.9 | 4.4 | 0.6 | 3.1 | 7.0 |
| **54** | Paso Huencho | 3.0 | 0.4 | 1.6 | 2.8 | 0.5 | 1.9 | 3.9 | 0.9 | 4.5 | 5.8 |

APPENDIX B

Tide Gauge Waveforms

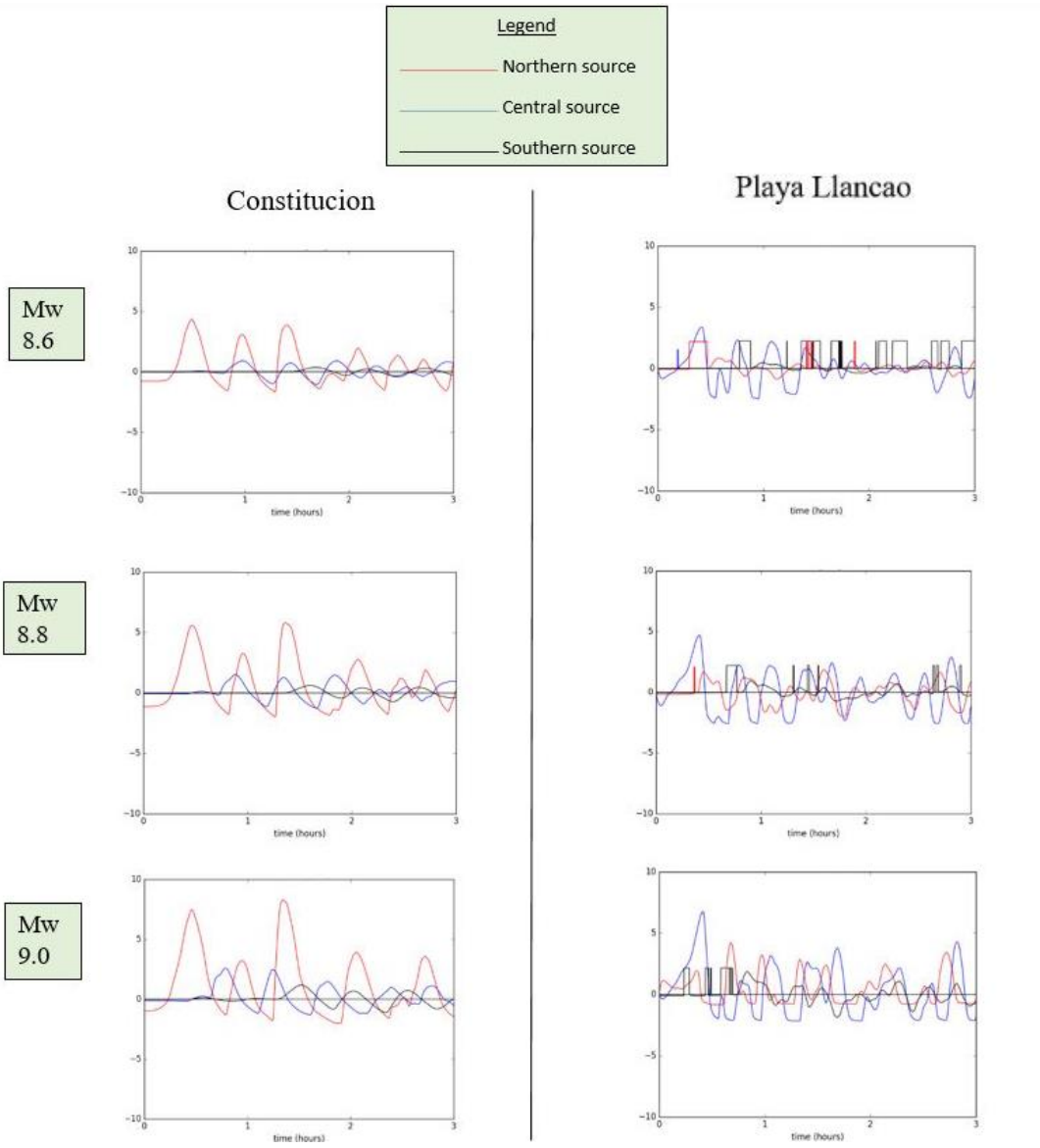


Figure B1: Tide gauge waveforms at Constitucion and Playa Llancao. The blue, black, and red squares in the Playa Llancao waveforms are the result of the tide gauge water depth oscillating above and below sea level due to changes in the resolution of the bathymetric grid during calculation in GeoClaw.

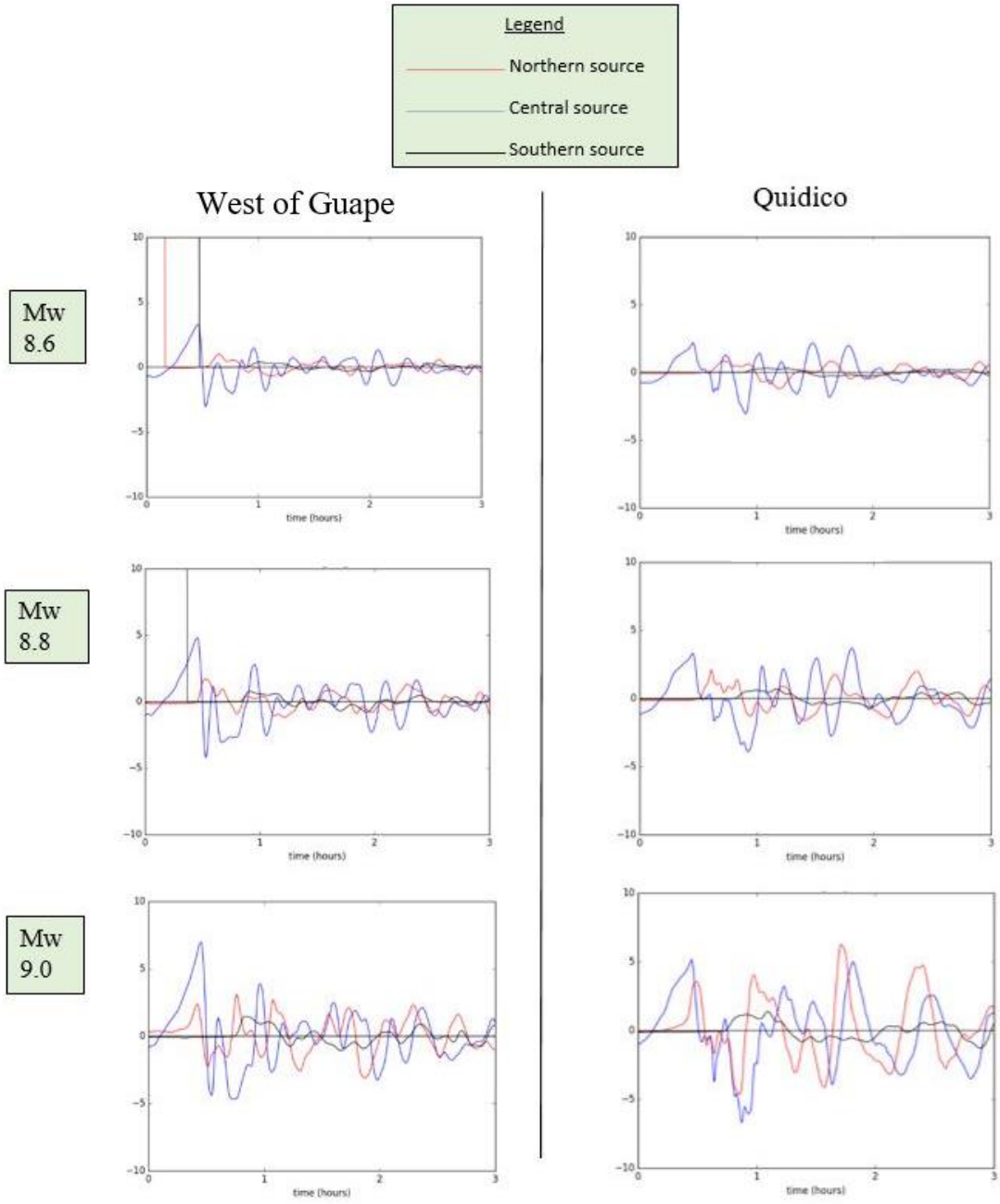


Figure B2: Tide gauge waveforms at West of Guape and Quidico.

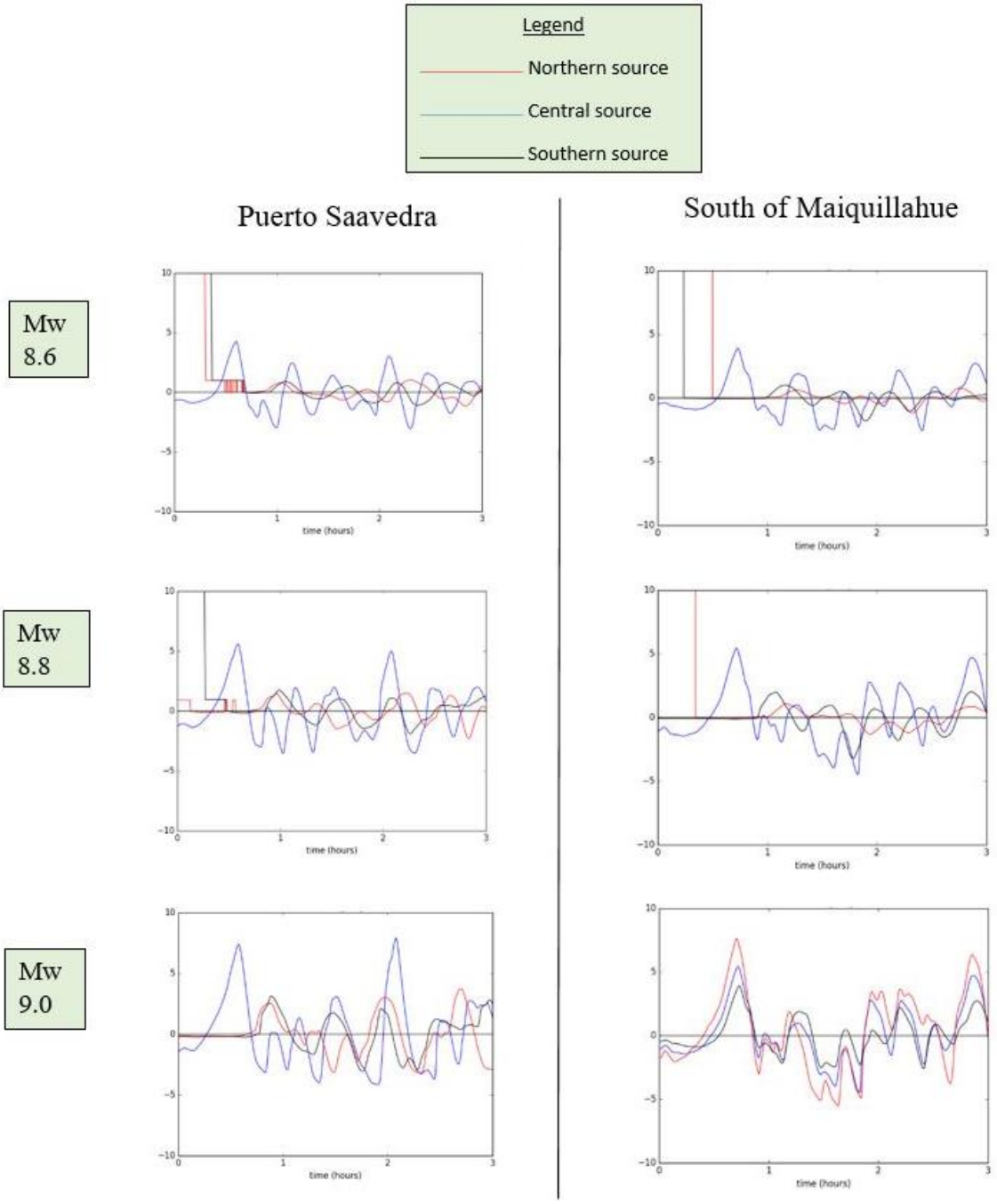


Figure B3: Tide gauge waveforms at Puerto Saavedra and South of Maiquillahue. The red squares in the Puerto Saavedra waveforms are the result of the tide gauge water depth oscillating above and below sea level due to changes in the resolution of the bathymetric grid during calculation in GeoClaw.

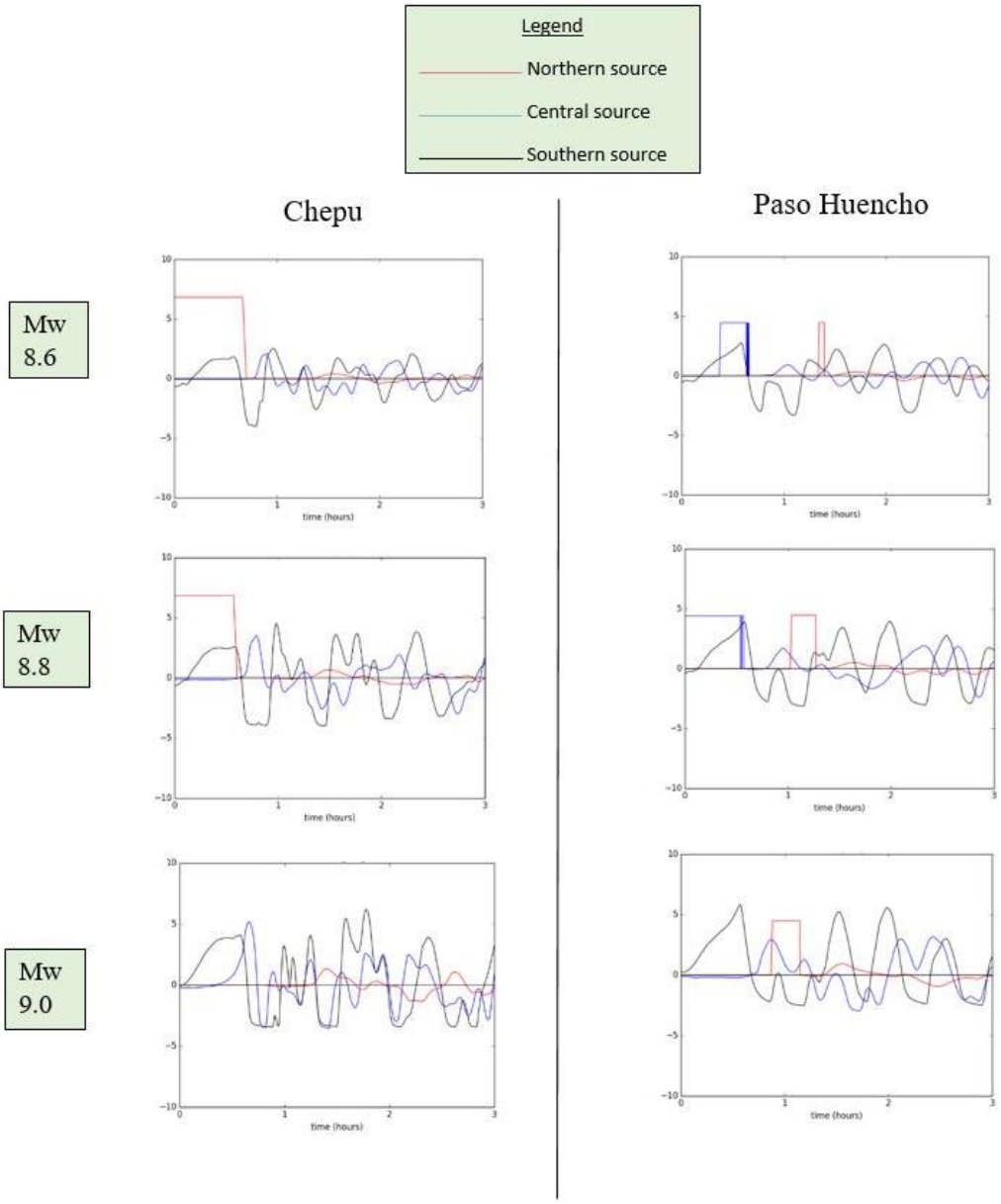


Figure B4: Tide gauge waveforms at Chepu and Paso Huencho. The red and blue squares in both waveforms are the result of the tide gauge water depth oscillating above and below sea level due to changes in the resolution of the bathymetric grid during calculation in GeoClaw.

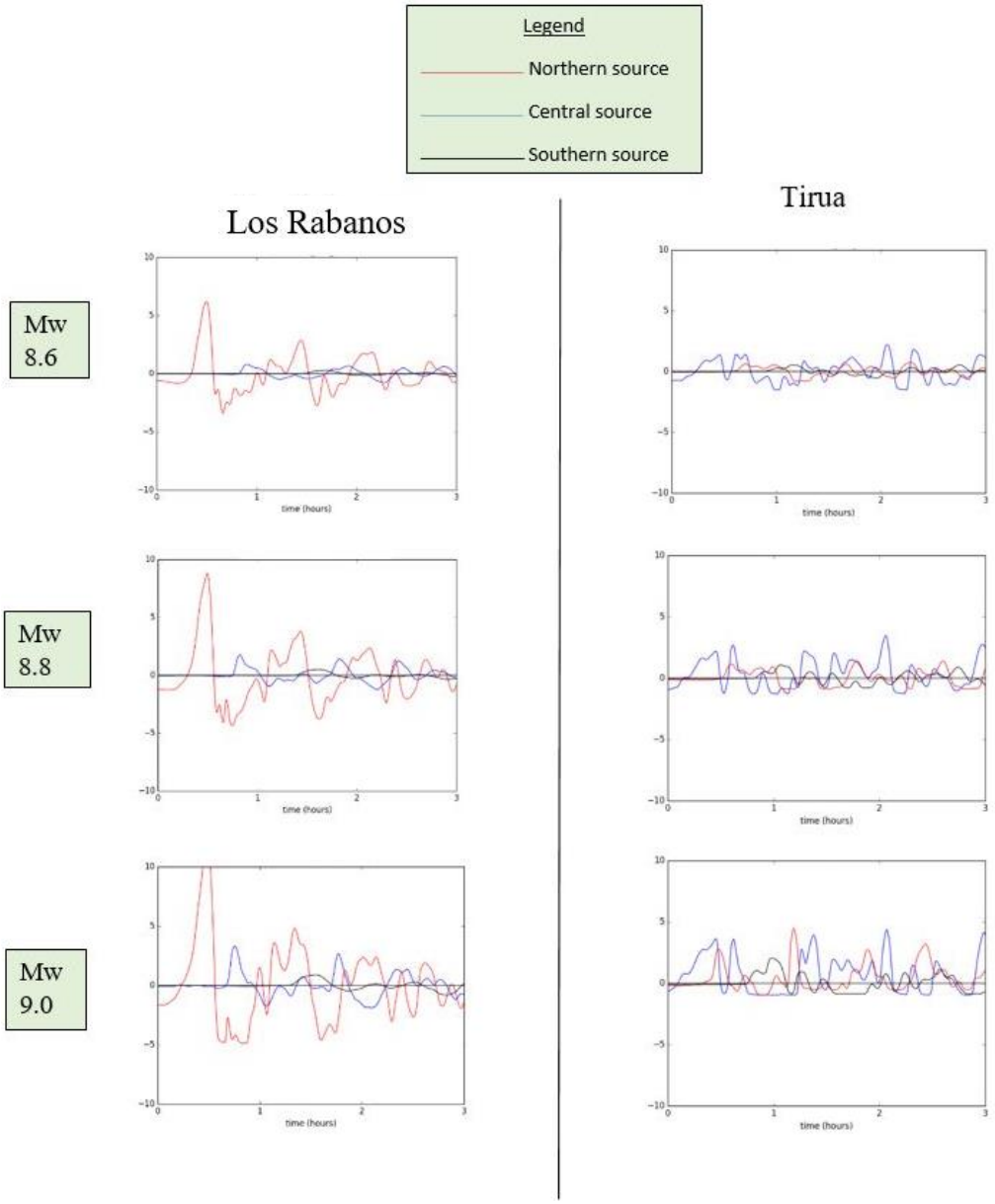


Figure B5: Tide gauge waveforms at Los Rabanos and Tirua.

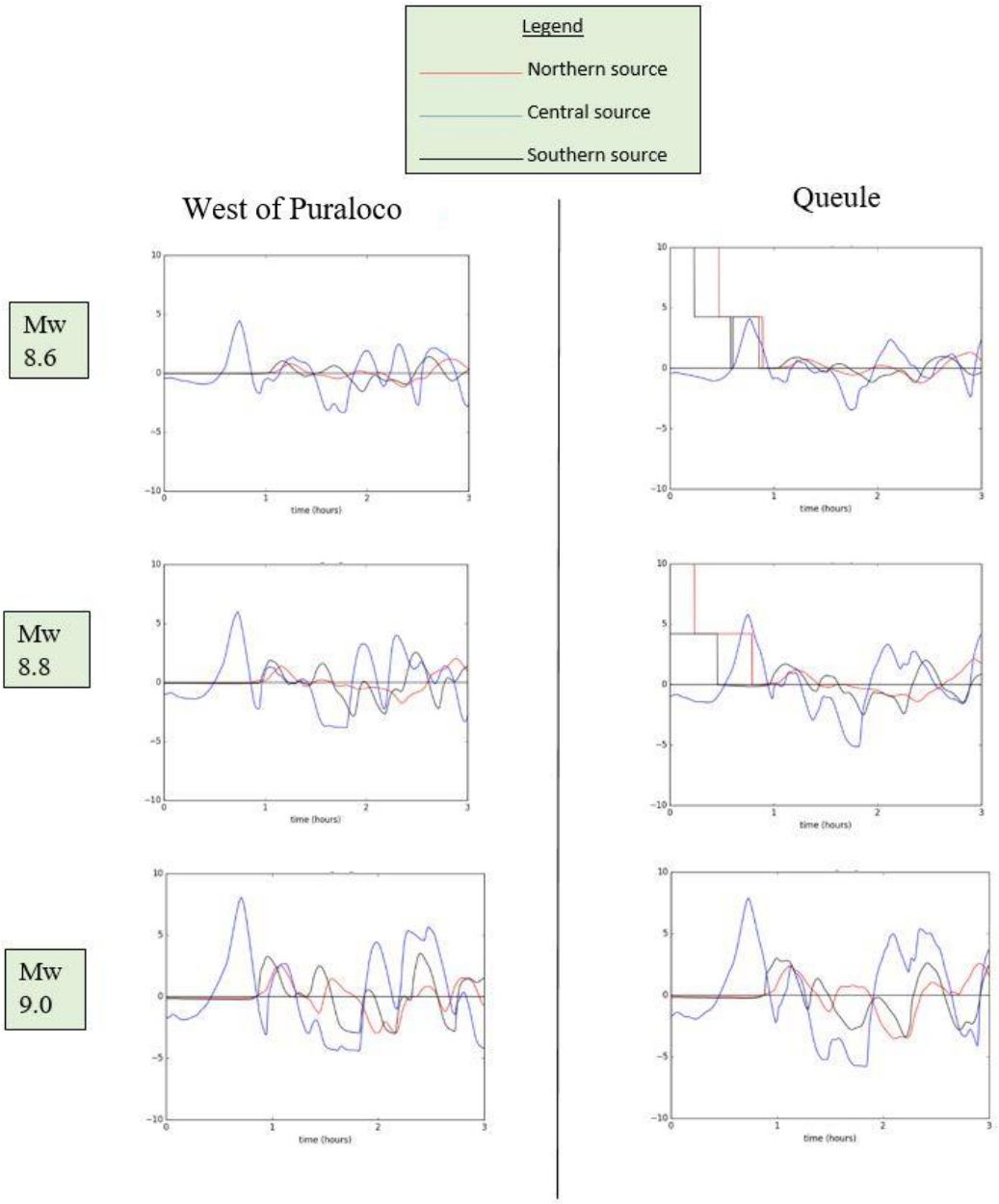


Figure B6: Tide gauge waveforms at Puraloco and Queule. The red and black squares in the Queule waveforms are the result of the tide gauge water depth oscillating above and below sea level due to changes in the resolution of the bathymetric grid during calculation in GeoClaw.

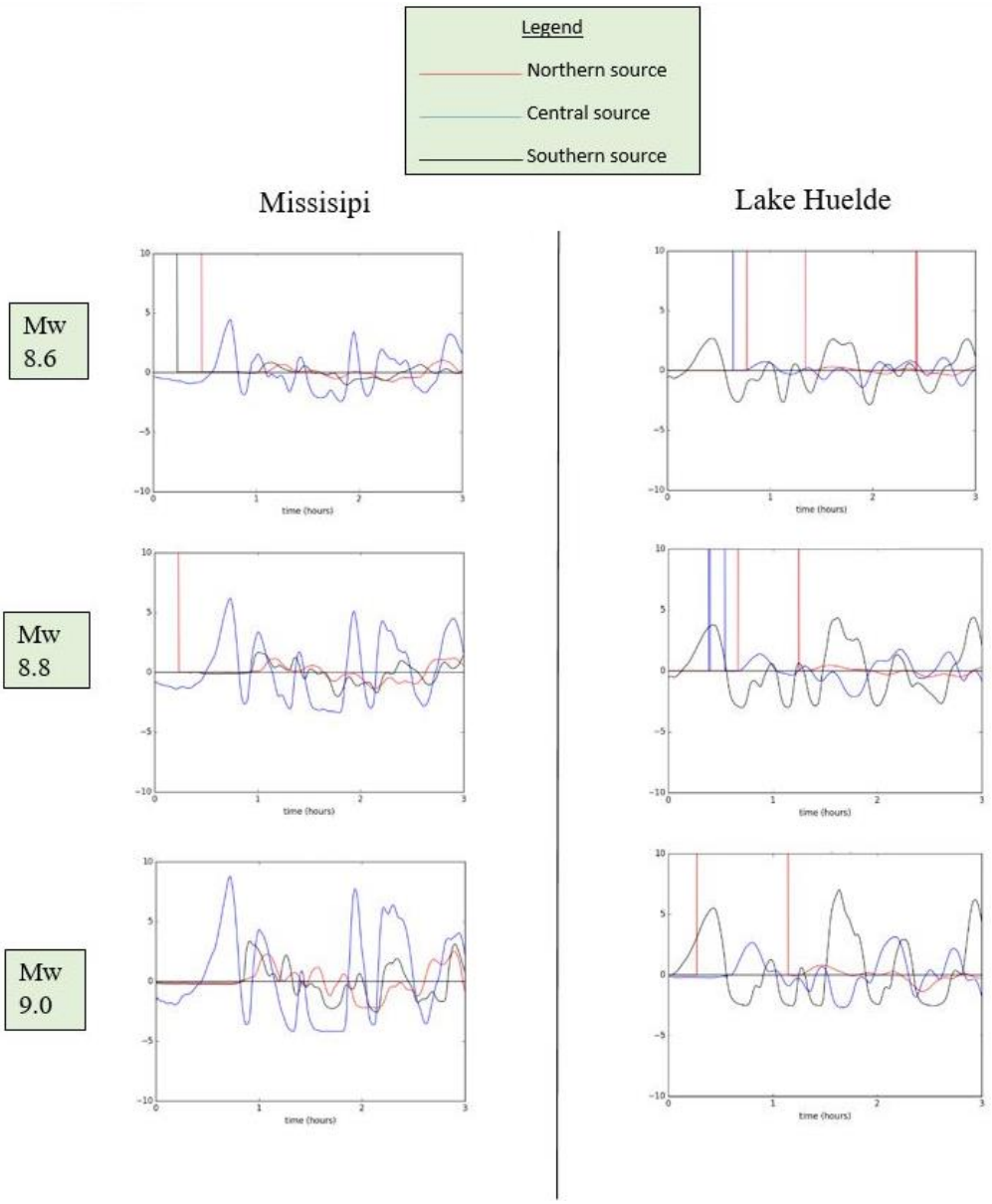


Figure B7: Tide gauge waveforms at Missisipi and Lake Huelde. The blue, red, and black lines in both waveforms are the result of the tide gauge water depth oscillating above and below sea level due to changes in the resolution of the bathymetric grid during calculation in GeoClaw.

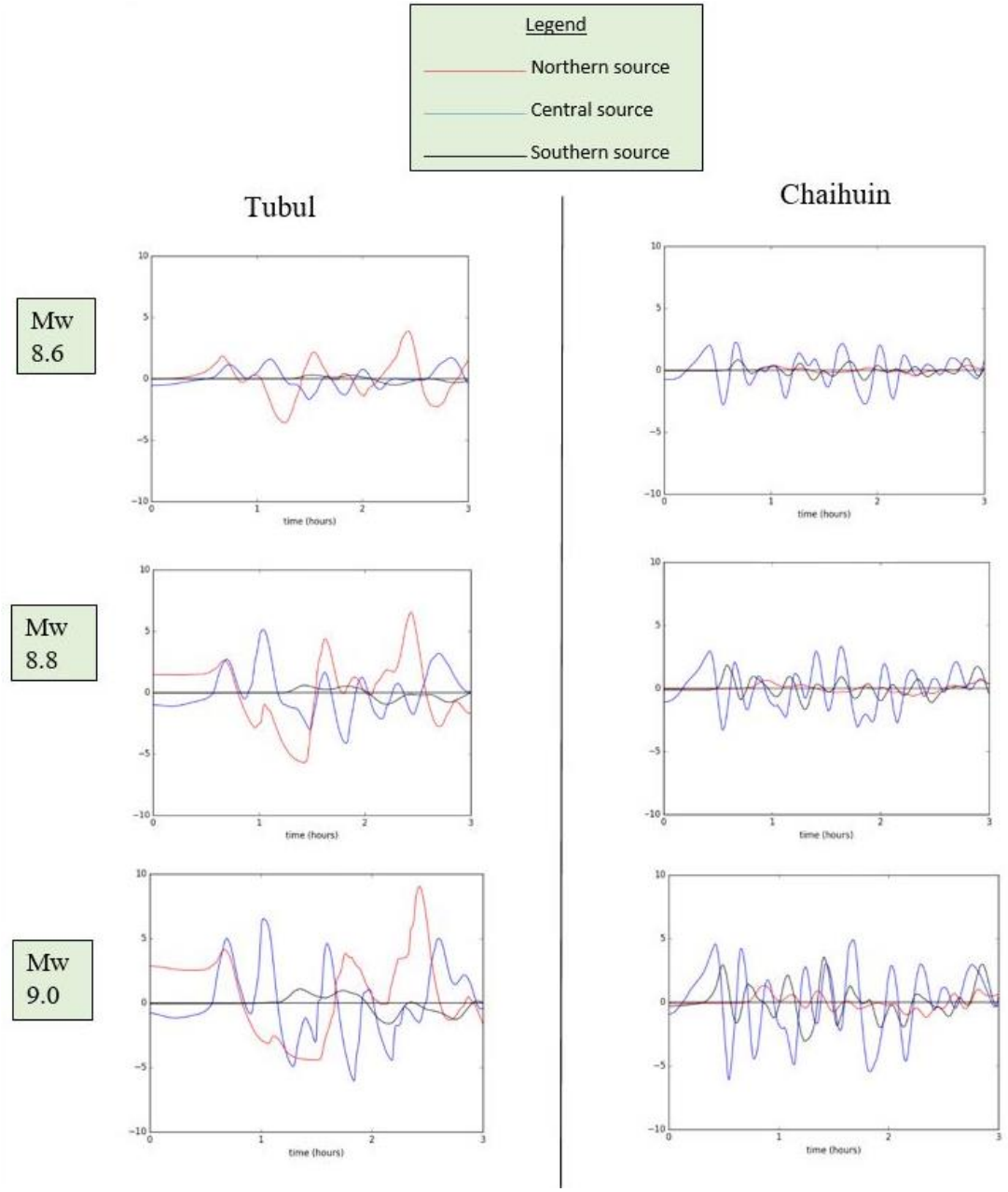


Figure B8: Tide gauge waveforms at Tubul and Chaihuin.

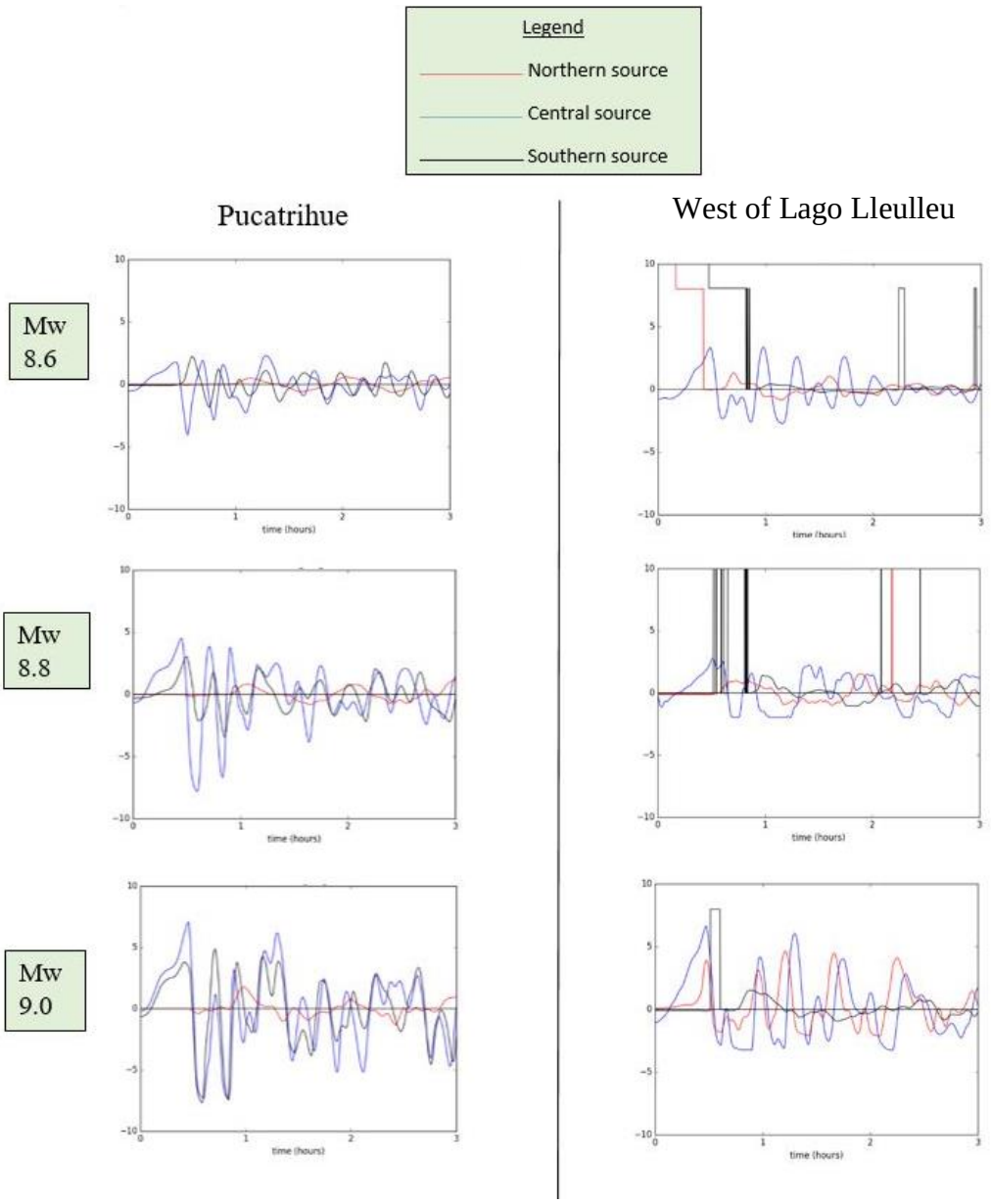


Figure B9: Tide gauge waveforms at Pucatrihue and West of Lago Lleulleu. The red and black lines and squares in the West of Lago Lleulleu waveforms are the result of the tide gauge water depth oscillating above and below sea level due to changes in the resolution of the bathymetric grid during calculation in GeoClaw.

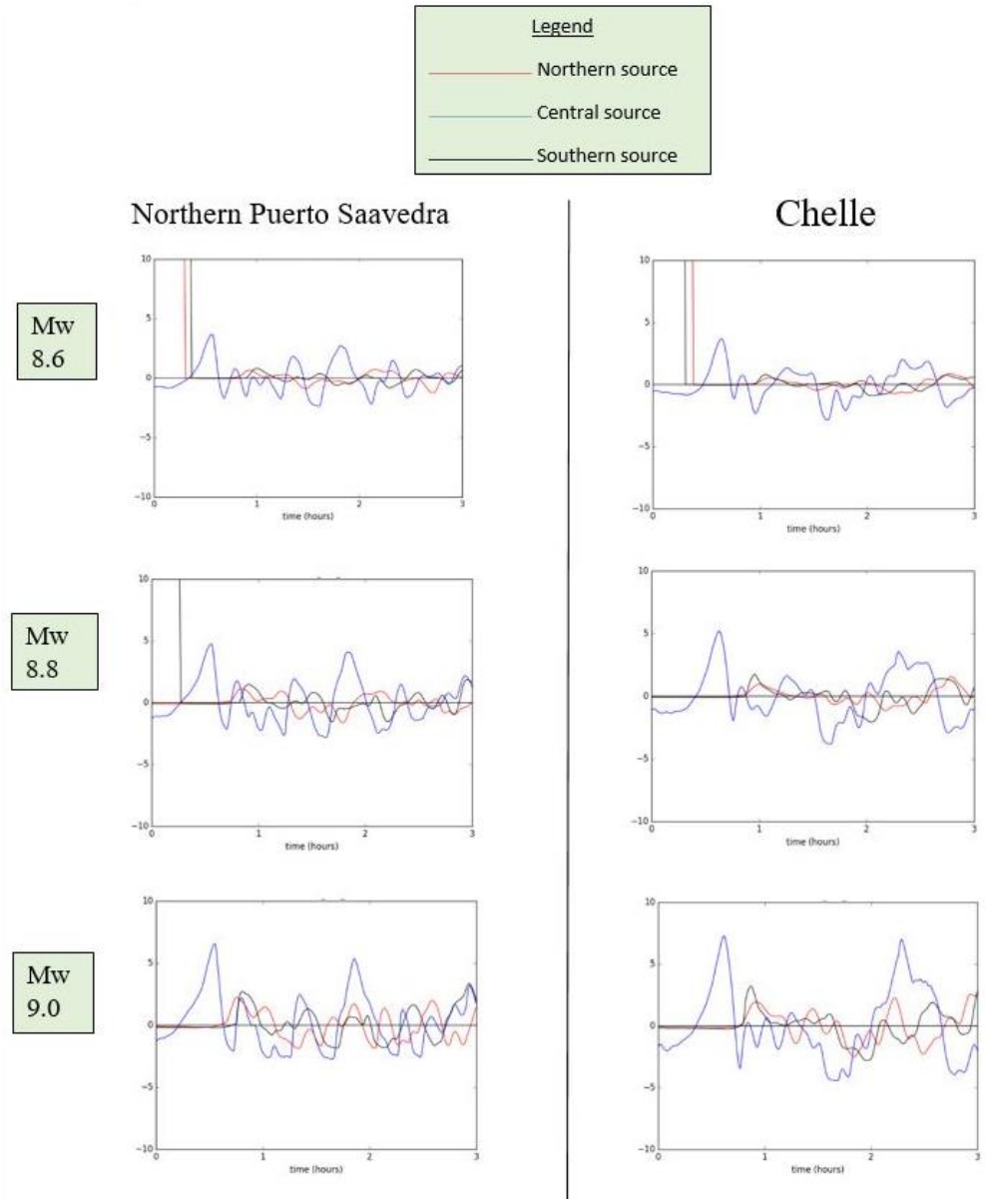


Figure B10: Tide gauge waveforms at Northern Puerto Saavedra and Chelle. The red and black lines in both waveforms are the result of the tide gauge water depth oscillating above and below sea level due to changes in the resolution of the bathymetric grid during calculation in GeoClaw.

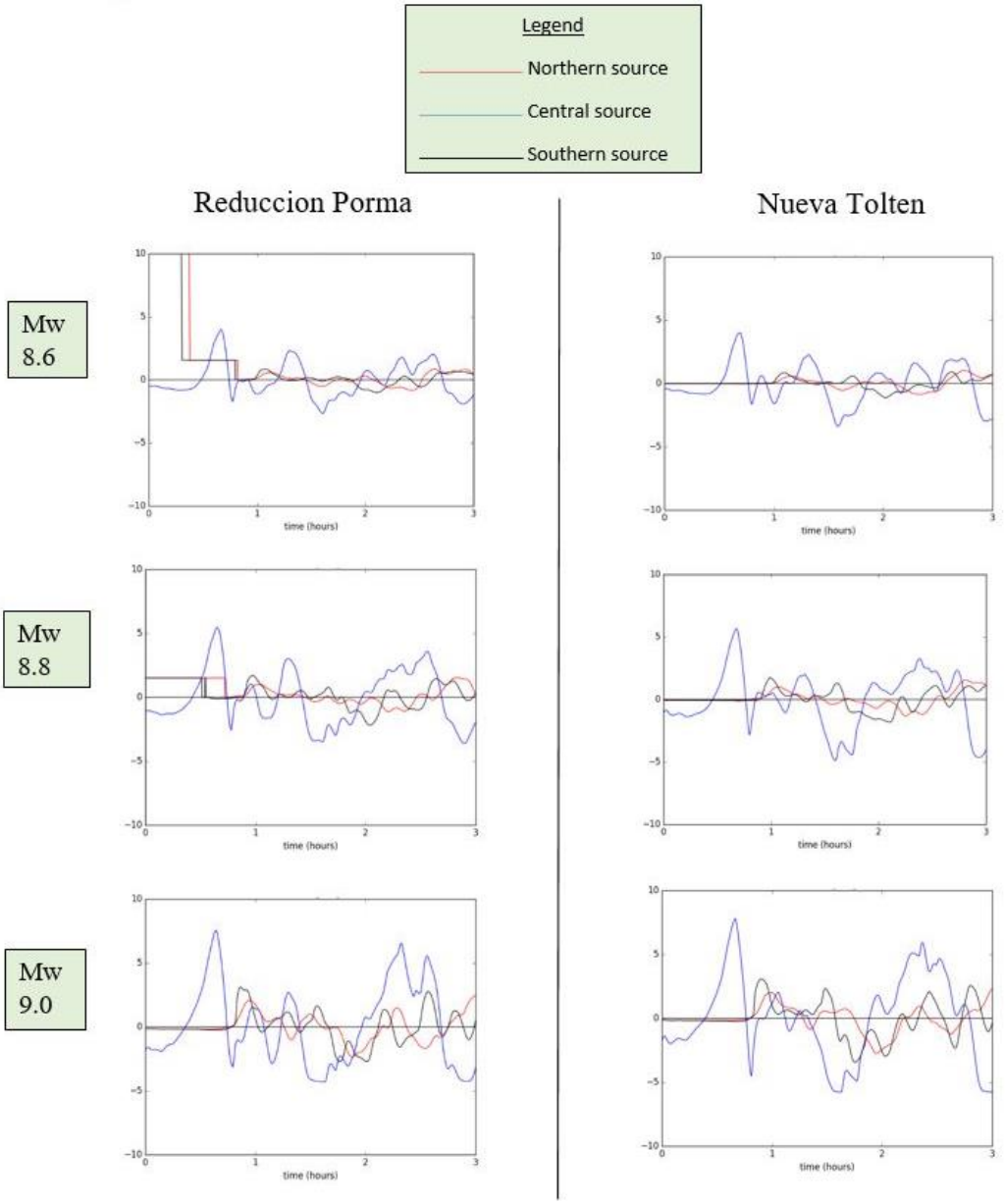


Figure B11: Tide gauge waveforms at Reduccion Porma and Nueva Tolten. The red and black lines and squares in the Reduccion Porma waveforms are the result of the tide gauge water depth oscillating above and below sea level due to changes in the resolution of the bathymetric grid during calculation in GeoClaw.